A Trigger for long-lived coloured or charged exotics for future luminosities in ATLAS

Master Thesis

by

Ursula Søndergaard

Supervisor: Rasmus Mackeprang

June 2010

Acknowledgements

Thank you Rasmus Mackeprang for showing me the wonderful worlds of BSM and SMPs and it's community, curiosities and fun people. If it were not for you I would not have written this thesis. Thank you (*and* Peter Hansen) also for giving me the opportunity to experience CERN on site and letting me come along to workshops, and for being a patient supervisor! I wish also to thank Sascha Mehlhase for excellent proof-reading, advice and sharing of experience, thanks to Morten for many good discussions and advice, thanks Esben for many cups of espresso brought to the table, special thanks to Stefania and Jørgen Beck for being very inspirational scientists, thanks to Lotte and Johan and Christian Ohm for great company at CERN, and thanks to the rest of the HEP group at NBI you have all been very nice, also the computing guys. Thanks to my other physics friends Majken, Terese, Karen, Catarina, Troels, Carsten, plus whoever I forget. Last and Biggest thanks to my dear Jacob.

Contents

List of Figures

Chapter 1

Introduction

1.1 Introduction

The search for hypothetic particles is motivated by different extended versions of the Standard Model of particle physics. These are turn motivated by the fact that the Standard Model, though impressively successful, is not quite sufficient in describing the material world and has features which suggest that it might be an *effective* theory rather than a fundamental one.

As has been noted in many a master thesis, text book etc. the Standard Model has had much succes in predicting observables of subatomic phenomena to a high precision and additionally it is very *extensive*. As it stands today it unifies three of the four known forces of nature in a consistent mathematical framework, capable of describing, at the *elementary level*, natural phenomena observed at high energy experiments. In high energy experiments particle beams are accelerated to relativistic speeds and steered to collide, and detector complexes enclosing the point of collision detect the outcome in ingenious ways.

The term 'elementary level' has at any point in the history of (particle) physics the level where observable entities appear point-like and indivisible. This level is bound *downwards* by the *upper* limit on energies attainable in collisions. As energies go higher and higher, structures beneath this level might appear; we cannot know beforehand what lies beneath this level, which must be set by *experiment*. On the other hand the idea that matter is made of small indivisible entities, atoms, was as is well known, conceived long before experimental observation of such an entity - by reasoning.

This picture is now known to be approximative, as atoms can be severed in electrons and nuclei and nuclei in nucleons. The picture does not stop here, as *firstly*, nucleons exhibit an internal structure; they are in the Standard Model built from elementary particles named *quarks*. Are electrons and quarks then the last indivisible entities? Approximatively, we might say yes. However this desciption also breaks down in the picture emerging from high energy experiments. Because, *secondly*, when you look close enough at a elementary particle it consists of virtual particles in addition to "itself", vacuum fluctuations appear.

'At earhtly energies' the picture of all matter being built from indivisible entities (then being the presently considered *fundamental* particles) is a good approximation and it is remarkable that the idea itself is so old.

Likewise it could happen that in the distant future ideas like string theory could be confirmed by experiment. String theories and M-theory are said to have the most succes in providing theoretical frameworks that can generate universes in congruence with the observed. There is however general agreement that the future, where the observation of strings is possible, might be as distant as never.

Therefore it is attempted to pose the question: are there hypothetical underlying principles leading to phenomenologies consistent with universes like the one we observe and that could be rendered more probable or be falsified at the current frontier particle physics experiment?

At the Large Hadron Collider (hereafter LHC) it is anticipated that new physics will appear, because the energies will go beyond the range of the Standard Model.

An important answer that it is hoped will be revealed, is the answer to the question: what is the mechanism for electroweak symmetry breaking? It is expected that the LHC (through the experiments ATLAS and CMS) can conclude whether the Standard Model Higgs mechanism can be counted as responsible or not. The Standard Model Higgs is a resonance and must be reconstructed from its decay products, the known Standard Model particles, and the whole experiment is tuned to these particles.

The Higgs is the last unobserved particle predicted by the Standard Model, but it is not the only phenomenon that may observed at LHC.

SMP = Stable Massive Particle is a jargon concept covering the class of hypothetic non-Standard Model particles with masses of 100-1000 GeV and sufficiently long-lived that they could be detected directly (i.e. not from their decay products) at modern collider experiments, in the sense that they might traverse a detector or at least the inner parts of a detector without decaying.

Several scenarios within for example *supersymmetry* and *universal extra dimensional* frameworks lead to states of the stable or meta-stable kind, which are in principle *detectable* in a modern *general purpose* detector context, i.e they are states that would interact electromagnetically or strongly with matter; states that interact only weakly are also implied by these scenarios, but would be detected through signatures using missing transverse energy.

We have at hand a modern general purpose experiment, the ATLAS experiment. In September 2008 the ATLAS detector saw its first events from proton beams of the Large Hadron Collider, the largest particle physics experiment ever.

SMP searches are made whenever a new collision energy is reached and in the absence of a signal, exclusion limits are then set on the mass of such objects. Before the LHC exotic hadrons with masses less than the order of a hundred GeV were excluded [13] by previous accelerator searches.

In march 2011 the most restrictive limits to date were set on the mass of hadrons containing SMPs in a *supersymmetry* scenario. These limits were set by the ATLAS Collaboration, using data from the latest proton-proton runs, reading for gluino, stop and sbottom respectively: 586, 309 and 294 GeV [31].

With these limits, supersymmetry scenarios predicting these states, can be rejected.

Therefore on one hand: the experimental discovery of a stable massive particle state would be significant - a clear evidence of new physics and insufficiency of the Standard Model; but on the other hand: as exclusion limits on the mass of such particles crawl upwards the rejection of specific scenarios that contain these kinds of states, eventually will leave little space for possible manifestations of the generating principle behind, and hence new ideas will be sought.

At modern collider experiments the main objective is the search for rare types of events, hypothetical as well as previously seen ones, and for this reason the larger part of data produced by the detectors will be superfluos/uninteresting.
Since data storage is not unlimited, rejecting uninteresting events is mandatory. An efficient trigger system is therefore part of any experiment searching for rare events.
The ATLAS experiment is one of the four big experiments at the Large Hadron ollider (LHC). It is a general purpose detector, built to discover new physics, yet it is tuned to the known particles of the Standard Model, since most searches assume rapid decay of the unseen state into known states, i.e a new particle would be discovered from its decay products.

The SMP search is orthogonal to this approach, so that particles which in principle would be detectable might be lost even at the trigger level.

The ATLAS trigger system exists at three levels. Level 1 is hardware/electronics based, consisting of simple thresholds on energy variations in the detector material. Standard Model particles will interact with the detector material leaving energy deposits behind when traversing, thus enabling detection with ATLAS, except for neutrinos which leave behind a signature of missing transverse energy. The L1 trigger system is based on objects which candidate for high-energy fundamental SM particles in a simple and coarse way i.e by leaving behind energy variation patterns in certain detector parts that are consistent with SM particles propagating out.

The second and third level (combined the High Level Trigger, hereafter HLT) are software based, consisting of more refined pattern recognizing algorithms. The second level are fast algorithms which run on simple event data from detector regions of interest, found by the first level trigger. Thirdly the Event Filter, consisting of off-line style algorithms, access the full detector read-out to make the final trigger decision.

As LHC intensifies, thresholds on trigger objects will be raised, and some of the trigger objects will suffer a hard *prescaling*, which means that only a fraction of the number of objects seen will result in passing the event. This will be potentially dangerous for the SMP search.

Here a dedicated second level trigger is studied, in order to estimate whether the theoretical efficiency of detecting SMPs can be kept/improved as prescales are applied and threshold raised.
I will consider only objects carrying as a minimum either *colour* charge or *electric* charge.

Concerning the layout of this report: The Standard Model will be shortly introduced along with the concerns attached to it, then will follow short introductions to possible extensions to it along with the generating principles behind these new models. The experimental context for which this work has relevance follows and finally we get to the description of the main results with conclusions.

Blurry photo of street name sign taken at night at CERN.

Chapter 2

Theoretical motivation

2.1 The Standard Model

Dating back to the 1960s when the theoretical possibility of unifying the electromagnetic and weak interactions was discovered [1] the Standard Model (SM) has been developed and refined in an interplay between laboratory experiments and theoretical development.

The SM can brag about many successes: experimental discovery of the omega-baryon in 1964 at Brookhaven Lab [2], confirming the quark model, theoretized in the 1950s [2], prediction (1972) and discovery of the weak current at Gargamelle, Cern 1973 [3], prediction (around 1968) of the masses of the W and Z bosons verified in 1981 [4, 5, 6, 7].

Of all the fundamental particles predicted the only one not observed is the Higgs boson, to be described below.

2.1.1 Overview of the Standard Model

The SM describes matter and the forces of nature, with the exception of the gravitational force, as quantum excitations of fundamental fields. The mathematical framework is a quantum field theory which unifies special relativity with quantum mechanics. From special relativity the formula $E = mc^2$ is inherited which describes the equivalence between mass and energy allowing for production (or destruction/annihilation) of matter if the energy is high enough (or the available phase space allows for it); in quantum field theory *quantum dynamics* is then described, which was not possible before when only quantum *mechanics* was formulated.

Particle content

In Figure 2.1 the experimentally confirmed fundamental particles are shown with their mass, charge and spin quantum number listed. The particles are grouped into *bosons* which are the force carriers and *fermions*, the matter particles.

The fermions appear in three generations only differing in mass, as shown in Figure 2.1. There are six quark and six lepton *flavours*. The leptons interact weakly and for the charged leptons also electromagnetically and the quarks interact in addition strongly, because they

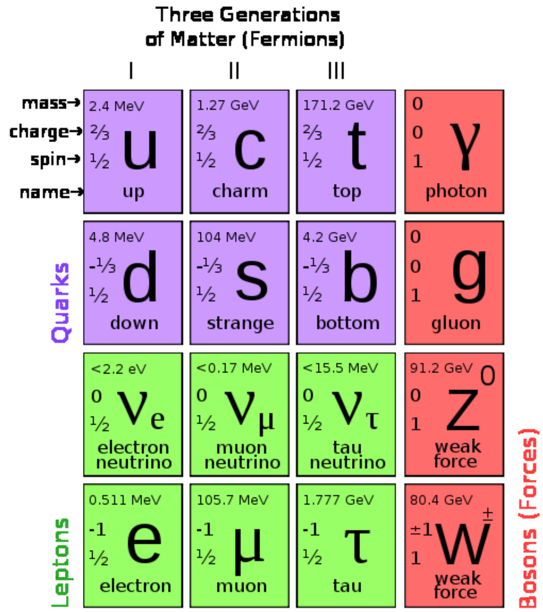

Figure 2.1: *The observed particles of the Standard Model, with mass, charge and spin indicated.*

carry colour charge.

The fermions interact via exchange of the bosonic field quanta of which the weak force carriers W+ and W- are flavour changing.

The mediator of the electromagnetic force, the photon has no charge and no mass.

The gluons are the strong force mediators and carry colour charge, but are like the photon massless.

Hadrons

Because of colour confinement quarks and gluons cannot exist freely in the energy regime of the SM. They appear only in colourless bound states. The bound states are named *hadrons* and are grouped in *baryons*, which are three quark states (qqq) and *mesons* which are quark-antiquark ($q\bar{q}$) states. The top quark however does not hadronise due to its lifetime being shorter than the hadronisation time.

At collider experiments a great number of free hadrons has been observed but only the proton (uud) is stable. The neutron (udd) is unstable but longlived when bound in a nucleus. All other hadrons have lifetimes of the order 10^{-9} or below.

The heaviest SM hadrons are the bottomium states ($b\bar{b}$) with masses of the order of 10 GeV.

Confinement can be described qualitatively as being due to the strong force being *very* strong at distances of the order of femtometer and larger [8], leading to permanent confinement inside colourless hadrons (with *colourless* being analogous to electrically *neutral*). The strong force is then *effectively* short ranged, eventhough at very short distances the force becomes zero, causing quarks to experience asymptotic freedom at distances tending to zero (less than

$\sim$ 1 fm).

2.1.2 Symmetries

Group theory is a discipline in mathematics dealing with structures at the abstract level. It turns out that three groups can be seen as underlying the behaviour of natural phenomena at the fundamental level:

$$U(1) \times SU(2) \times SU(3) \tag{2.1}$$

U stands for *unitary* meaning the group can be represented by unitary matrices and S stands for *special* meaning the determinant is equal to unity. The numbers 1, 2 and 3 are in the representations the dimensions of the matrices.

When imposing invariance of the Lagrangian of a field theory under *global* transformations conservation theorems arise in accordance with *Noether's theorem* [9]. The term *global* means that the transformation is applied uniformly to all points in space.

For instance conservation of momentum arises from invariance under translation [9].

$$q \to q + \Delta q \tag{2.2}$$

where q represents a set of generalised coordinates.

When imposing *local*, i.e position dependent invariance, *gauge bosons* arise. Local transformations are e.g. rotations in Minkowski space or complex mixings between the fermions of the theory.

The possible interactions of a theory are determined uniquely by the symmetries contained in the relevant group which are in the SM one of (2.1); for electromagnetic and weak interactions, which are unified at the order of 100 GeV, it is $U(1) \times SU(2)$ and for strong interactions it is $SU(3)$.

Once the formulation of the interacting fields is done, a theory still must be given specifications of free parameters by measurement, and the process of renormalisation must be performed. Calculations in quantum field theory are done using perturbation theory, valid within ranges where the interactions in question are weak. In these calculation many of the integrals turn out to be divergent giving infinite answers. In the process of renormalisation one gets rid of these divergencies by choosing a energy cut-off.

Divergent contributions are well illustrated by their representations in Feynman diagrams. Feynman diagrams are graphical representations of the perturbative contributions to the transition amplitudes of a field theory.

The divergences appear in calculations of loops with *virtual* particles.

It turns out that in SM processes radiative corrections applies, for example in quantum electrodynamics (QED), in the form of brehmsstrahlung and loop corrections. In Figure 2.2 a loop diagram is shown depicting a photon creating a virtual electron-positron pair, which then annihilates into a photon, the process of vacuum polarization. The creation and annihilation of such virtual particles are allowed by Heisenbergs uncertainty relation [2]:

$$\Delta E \Delta t \geq \hbar \tag{2.3}$$

Virtual particles can then have arbitarary energies as long as (2.3) is satisfied.

SM observables like mass contain contributions from loop corrections; for instance the electron mass receives contributions from emitting and reabsorbing virtual photons.

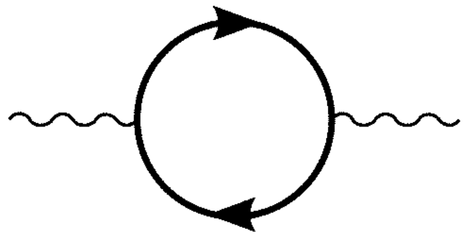

Figure 2.2: *A feynman diagram of vacuum polarization; a photon creates a electron-positron pair which annihilate.*

Electroweak symmetrybreaking

As mentioned in the above section the weak force and the electromagnetic force are unified at the weak scale. Below this scale, the symmetry between the photon and the weak bosons is broken by the acquisition of mass of the weak bosons, an effect for which, in the SM, the Higgs mechanism is responsible. Without this mechanism all particles are massless. Specifying a gauge invariant quantum field theory for a given symmetry group gives the structure of the theory in terms of matter content and force mediators, but without masses.

In the Higgs mechanism masses arise from interactions with the *Higgs field*, a complex scalar field, which couples to itself, and should be manifested as a massive boson, the *Higgs boson*. Apart from explaining how masses arise the mechanism also explains electroweak symmetry breaking.

The Higgs mechanism is not the only theoretized mechanism that can explain electroweak symmetry breaking and fermion masses; other examples are *technicolour* models [10] and other gauge mediated symmetry breaking models as well as *preon* models assuming compositeness of the massive particles, explaining mass by confinement of these new fundamental particles [11].

The non-observation of the Higgs motivates searching for alternative underlying theoretical frameworks for explaining electroweak symmetrybreaking and the observed massiveness of matter particles.

There are other concerns attached to the SM, the graveness of some of which are up to discussion. For some of these concerns though it can be argued, that they are decidedly evidence of insufficiency. Below a quick overview of these concerns will be given; a more thorough overview can be found e.g in [8].

2.1.3 Beyond the Standard Model

Motivations for the theoretical searches for new physics going beyond the SM can be grouped into motivations rooted in

- theoretical concerns
- non-observation of predicted phenomena
- observation of phenomena not predicted

The second group is quickly exhausted as only the Higgs has not been observed.

2.1.4 Theoretical concerns of the Standard Model

In the SM coupling constants determine the strength of interactions, i.e how probable a transition appear. These constants are *not* exactly constant but depend on the energy/mass scale, they *run* with the energy scale.

The electromagnetic coupling *increases* with increasing energy while the strong coupling *decreases*.

Hence the predictions/descriptions ranging from perturbative calculations are expected to break down at scales where perturbation theory is no longer valid. Above this cut-off, normally set to the order of TeV, coupling constants can be expected to diverge.

The cut-off scale has to be chosen “manually” which suggests that the SM might be an effective theory rather than a fundamental one.

These considerations are related to the so-called *hierarchy problem*. As noted in the previous section masses contain contributions from loops of virtual particles, and in the case of the Higgs mass, top loops dominate; the uppermost diagram in Figure 2.4 depicts a top loop contribution to the Higgs mass. The Planck scale Λ_p is defined as the scale where the gravitational energy of two masses placed at a distance of one Compton wavelength from each other equals their rest energy. Hence it is the scale where quantum gravitational effects should become important and therefore it would be reasonable that the SM is not valid in this regime since the SM does not include a description of gravity. If the SM should be valid to very high energies such as the Planck scale ($\Lambda = \Lambda_p$), the corrections needed to fine tune the Higgs mass are many orders of magnitude larger han the Higgs mass itself if the Higgs is a light Higgs with a mass at the order of 100 GeV. In this picture there is a gap from the energy scale of electroweak symmetry breaking up to the Planck scale where no new physics appears and this ’energy desert’ along with the corrections needed to fine tune the Higgs mass can be considered hierarchically problematic. (maybe put below paragraph in the introduction?) However the arguments used against the above picture claim such a model to be “unnatural” - but natural phenomena can never be unnatural no matter how counter-intuitive they might appear. Theories can of course be wrong and what complicates things is that they can be very good approximations in some ranges but fall short in other.

2.1.5 Observation of unexplained phenomena

Quantum field theory unifies quantum mechanics and the theory of special relativity. It does not incorporate the general theory of relativity. General relativity is non-renormalisable when viewed as a quantum field theory. Hence the SM does not describe gravity. Yet gravity has been observed at the macroscopic level since the dawn of science.

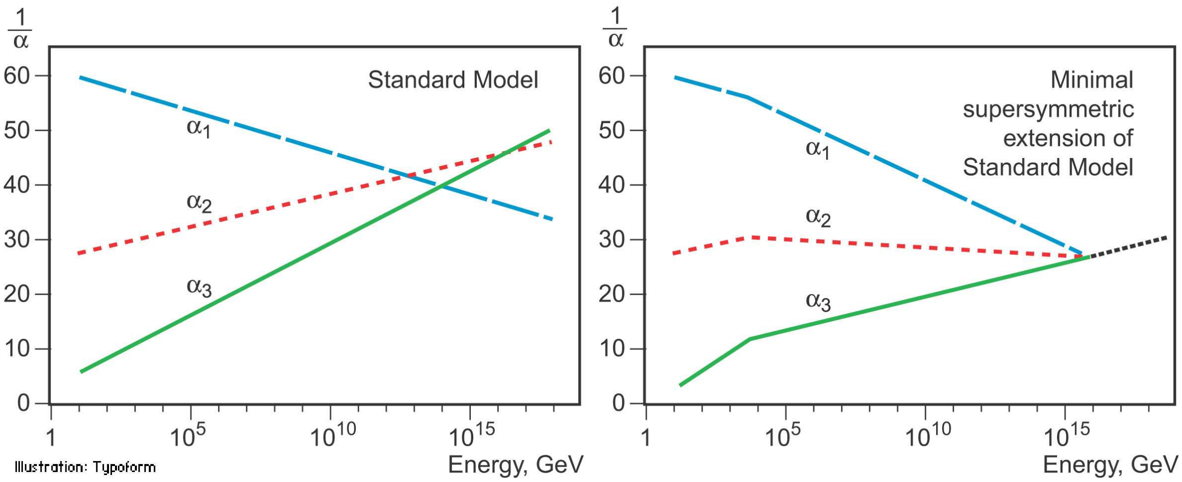

Figure 2.3: *Running of coupling constant with α_1, α_2 and α_3 being the electromagnetic, weak and strong couplings. They converge in the SM, in SUSY they unify, when assuming the SUSY paticles are not heavier than the order of TeV. From http://nobelprize.org.*

Also at the macroscopic level observation reveals that only 4% of the gravitating matter in the universe can be acconted for by SM particles. Of the missing 96 % around 24 % could be weakly interacting matter (dark matter) and the rest should be a constant vacuum energy density, *dark energy*. So-called weakly interacting massive particles (WIMP) are a hypothesis that explains the observed cosmic matter density, when the WIMP has a mass at the GeV scale [12]. The SM has no WIMP candiate since the neutrinos are the only particles interacting only weakly and they are relativistic and too light to candidate (ref to be inserted).

In the SM neutrinos are described as massless, but they are observed to be able to oscillate between the different flavours. This phenomena can be explained by ascribing masses (yet very small) to the neutrinos.

Yet another fundamentally important observation not accounted for in the SM is the asymmetry between matter and antimatter which is apparent according to astronomical observations. If this asymmetry did not exist, there would be no matter; however in particle physics experiments only weak interactions violate CP-symmetry, i.e. prefer matter over antimatter and the rate cannot explain the imbalance observed in the universe, in fact this asymmetry can only account for a single galaxy (ref to be inserted).

2.2 Beyond the Standard Model models

As described in section 2.1.4 the coupling constants of the SM are observed to *run*. When the energy scales go higher and higher the strong, weak and electromagnetic constants are observed to converge, as shown to the left in Figure 2.3.

This phenomenon has inspired the idea of Grand Unified Theories (GUT) where the three gauge symmetries are unified at a GUT scale (around 10^{19}) into one group and with just one coupling constant. However these theories predict instability of the proton which is non-observed.

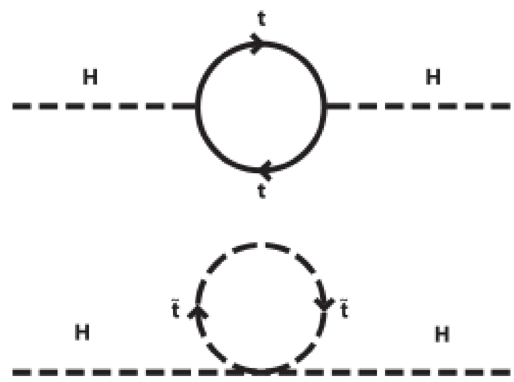

Figure 2.4: *Top and stop loop contributions to the Higgs Mass, from [37].*

Supersymmetry (SUSY) is a symmetry between fermions and bosons. In unbroken SUSY there is a bosonic partner for every fermion (and vice versa) equal in all properties except spin (and derived properties thereof). The new SUSY particles are commonly combined named *sparticles* and the new bosonic partners names are generated by prepending "s" to the SM fermion name, the new fernionic partners get an "ino" appended to the SM boson name (stop, gluino); common notation is to add a $\tilde{}$to the particle symbol for sparticles ($\tilde{t}, \tilde{g}$). This notation and nomenclature will be used throuhg-out this report.

Clearly any theory to be considered as an extension of/replacement to the current model must, besides being more inclusive in describing natural phenomena, be in accordance with experimental data as well as self-consistent. It is then clear that in any acceptable SUSY scenario SUSY is broken, otherwise we would have seen, even without collider experiments, evidence of the particles that would be the bosonic equivalents of the known fermions and vice versa. There exist different suggested mechanisms for SUSY-breaking but it is not relevant here to review these. We are here only interested in noting the attraction of one of the most popular principles to generate extensions to the SM.

In some SUSY models the coupling constants unify (see right side of Figure 2.3) which is one of the reasons why SUSY models have been explored quite extensively.

SUSY also can provide for a dark matter candidate which will be described below.

Some SUSY models solve the hierarchy problem in a elegant way. The main contribution to the SM Higgs mass is the top loop which is illustrated in the uppermost diagram in Figure 2.4. The divergent integrals stemming from the loop are exactly balanced by the new stop field (the stop loop shown in the bottom-most diagram). The correction from stop loops gives precise term-wise cancellation of the quadratic divergences, because there is a minus in front of the fermionic contributions and not of the bosonic contribution.

SUSY has generated numerous different phenomenologies, some focuses on the solving of the hierarchy problem, others the dark matter problem and yet others have gravity-mediated SUSY-breaking. SUSY is not the only priciple that generates exiting phenomenologies, but it is among the most extensively studied frameworks.

Another popular principle is addition of new dimensions to the four known; these kinds of models can also account for unsolved problems. For example in models with Extra Dimensions (ED) that are compactified, the hierarchy problem is solved through the adding the extra dimensions, because the Planck scale moves down as a result. (bit more detail to be added!)

2.2.1 Stable massive particles in beyond Standard Model scenarios

New SMPs are predicted in a variety of SM extending scenarios. In the SM stability of massive states are generated by symmetries, i.e quantities that are either strictly conserved or almost. Conservation of charge and baryon/lepton number can be said to cause the stability of electrons and protons. Muons, charged pions (ud-states which are the lightest mesons) and kaons (mesons containg strange quarks and ud quarks) are meta-stable due to their decays being mediated by the weak interaction and because the strong force conserves flavour. Stablity or meta-stability can also be due to a limited decay phase space, for example as in the case of the neutron. The free neutron is meta-stable but can have very long lifetimes when bound in nuclei, due to a small decay phase space [13]. In models extending the SM the same kind of mechanisms can apply. Unconstrained SUSY results in nonphysical vertices violating lepton and baryon number conservation and this would lead to rapid proton decay. One solution is to introduce a new global symmetry defined by conservation of the multiplicative quantum number R, defined as:

$$R = (-1)^{3B+L+2s} \tag{2.4}$$

where B is baryon number, L lepton number and s spin. This symmetry, called R-parity, leads to stability or meta-stability of new heavy states in certain scenarios. Examples are *Split* SUSY scenarios which are characterized by the new scalar bosons having very much higher masses (order of TeV) than the fermions. The $\tilde{g}$ is allowed to form an R-hadron due to being sufficiently long-lived (t>femtoseconds) to not decay before hadronisation. This is due to the gluino being colored, hence it can only decay to other colored particles/sparticles, but R-parity conservation forbids direct decay to quarks and/or gluons. In models with very high squark masses the decay though these are highly surpressed, as illustrated in Figure 2.5.

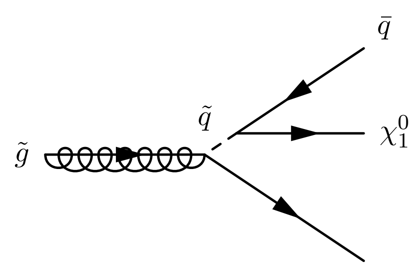

Figure 2.5: *An illustration of a gluino decaying to a χ_1^0 through a virtual squark. In models where the squark is extremely heavy and this is the only decay channel open for the gluino this decay is suppressed to the point where the gluino may acquire even very long lifetimes.*

2.3 Cosmological searches & limits

Absolutely stable SMPs is constrained by cosmology and from non-observation in terrestrial matter and meteorites which is reviewed in ref. [13]. These searches set very high lower mass limits on charged stable particles ranging from 10^3 TeV from γ-ray detectors to 10^5 TeV from observation of infalling charged, massive particles from the galactic halo onto the disk [14]. Terrestrial searches also exist. For instance a SMP with positive electrical charge have been searched for in water, since it would form a hydrogen-like bound state, excluding such states with masses up to 10 TeV [14]. Previous collider searches are added, for instance the CDF experiment at Tevatron set an upper limit on the production cross section of between 120 pb and 5 pb on pair-produced fermionic SMP with masses in the range 50-500 GeV and with positive or negative charges of $e, 2/3e, 5/3e$; the search techniques are described in [13].

Chapter 3

Experiment

3.1 The Large Hadron Collider

Figure 3.1: *The Large Hadron Collider (large ring) with the SPS injector (smaller ring). From* `http://www.scifun.ed.ac.uk/main.html`

In 1996 it was decided to build a 14 TeV proton-proton collider at CERN using the existing 26.7 km underground tunnel previously used for the LEP machine [15], the Large Electron-Positron collider running from 1989 til 2000. The LEP was (and still is) the most powerful lepton collider ever built with speeds of the colliding electrons/positrons exceeding 99.99975 per cent of light speed. The LEP was a *precision machine*, providing extremely accurate mass measurements of the gauge bosons Z and W+/-. In turn the Z and W+/- were experimentally discovered with the Super Proton Synchroton which is now used as an injector for LHC, as shown in figure 3.1.

CERN is the european center for subatomic physics research (originally nuclear physics, hence the acronym for Conseil Europeene de la Recherche Nucleaire) located in the vicinity of Geneva, Switzerland. The research center was founded officially in 1954, as a collaboration between 12 member states, pioneered by a handful of phycisists among which was our own Niels Bohr. Now there are 20 member states but more than 40 countries take part in the experiments through the participation of some 608 institutes from around the world.

In September 2008 the Large Hadron Collider (LHC) was fully constructed and the first beams were injected and circulated succesfully. But after less than 2 weeks a faulty electrical connection causing a large helium leak [16] forced shutdown for more than a year. In november 2009 the machine was started again [17] and there has been reported no more serious incidents to this date. The aim of the LHC is to reveal new physics, it is a *discovery machine*. It mainly accelerates *proton bunches* to speeds up to 99.9999991 per cent of lightspeed. The beams travel in opposite directions in two separate beam pipes deep underground and are steered to collide at four designated points where seven detectors are placed: ATLAS, CMS, ALICE, LHCb, ALFA, Totem and MoEDAL.
Until the time of writing this thesis the maximum energy in the p-p collisions has been as much as 7 TeV, which is the highest energy seen in man-made collisions, but eventually the maximum will be raised to 14 TeV. Accelerating subatomic particles and keeping them circulating in focused beams is done via a system of electric and magnetic fields. Because protons carry charge they can be accelerated by electric fields. The magnetic fields also accelerate the protons, but only by constantly changing the direction so that they are kept on a circular path. At the energies in question the use of the superconducting dipole magnets is demanded creating fields of up to 8.33 Tesla. In order for the magnets to be superconducting their temperature must be around 2 K; this demands a cooling system with 96 tonnes of liquid helium, which means that the LHC has the largest cryogenic facility in the world.

Proton collisions

(to be added somewhere: valence og sea quarks etc).

When protons collide numerous different processes are possible. In fact it is wrong to say that the protons collide, since protons are composite objects consisting of elementary particles in the SM. Hence it is the *partons* (quarks and gluons) which collide and this fact makes the situation rather complex. There can be have gluon-gluon collisions as well as quark-quark and quark-gluon collisions and never will we have the completely 'clean' event of two fundamental particles colliding in a vacuum. When ever we have 'hard interaction' (inelastic scattering) we also have an 'underlying event' stemming from so-called soft interaction of the partons not taking part in the primary collision; additionally radiation associated with the primary interaction is present. Eventhough the beam energy is very precisely known, the energy of the specific parton is not. This means that for a collision event we have no way of knowing the initial energy, except that to a high accurracy it can be assumed that the momentum-energy in the plane transverse to the beam directions is initially zero, and therefore must also add up to zero in the final states. This way a known source of unknown momentum like neutrinos can be constrained. From a detector point of view the only stable SM particles that are 'invisible' are in fact the neutrinos. Any other particle has either colour or electrical charge or will decay rapidly into particles with either of these charges so that the mother particle can be reconstructed from its visible daughters.

Even so it would still have been preferable to have a clean interaction between primary particles and this was exactly the case for the LEP experiment allowing for precision measurements of fundamental parameters. The problem with colliding electrons in a ring is that beam energy is lost due to synchrotron radiation. Any charged particle emits radiation, when accelerated as described by the Larmor formula. In the relativistic generalisation, relevant for high energy physics, the power radiated is proportional to the squared charge and inversely proportional to the squared mass of the accelerating particle, and therefore choosing a much heavier particle eliminates the loss of energy, to an extent sufficient for creating energies far exceeding the TeV limit, while still being able to use the existing circular tunnel.

For a given process the number of events is given by N = L * σ , where L is the luminosity measuring the number of protons crossing per area (square cm) per time (seconds) and σ the cross section in barns ($1barn = 100fm^2$) for the process in question.

Produced data is measured in time integrated luminosity conveniently expressed in 'inverse femtobarns' so that if a process has a cross section of a picobarn, then after an integrated luminosity of an inverse femtobarn, a thousand such events would be expected.

Lead Ion Collisions

It was mentioned that the colliding beams would be mainly of protons. The LHC will also for shorter time intervals be emptied of the proton beams and lead nucleus beams will be injected.
As with the protons, the lead nuclei will be steered to collide, here with the purpose of studying matter at densities/temperatures as they were after a millionth of a second after Big Bang. At that time quarks and gluons are believed to have been freely existing - in a state of plasma. The ALICE detector was built specifically to study this state. Indeed there have been signs of 'jet quenching' in the data from the first pb-pb collisions recorded in December 2010 at a per nucleon energy of 2.76 TeV [18].

ATLAS and CMS, complimentary experiments

The ATLAS and CMS experiments are *general purpose detectors* (see section about ATLAS) and they were built with the main objective of detecting new physics produced from the proton-proton collisions. The advantage of having two such detectors is that their measurements are independent and so results/discoveries made by one collaboration, can be confirmed by the other.

3.2 Hadronic interactions and calorimetry

Particles traversing a detector interact with the detector material by depositing energy via either electromagnetic interaction (for charged particles) or nuclear scattering. The energy deposited can then be converted to a signal to read out.

Electromagnetic interactions

The electromagnetic energy loss happens either through ionisation, excitation or additionally elastic Coulomb scattering from nuclei.

For a given medium the mean rate of ionisation loss of a charged particle depends only on the charge and the velocity of the particle. This dependency is given by the formula known as the Bethe-Bloch formula. In Figure 3.2 the ionisation loss is shown for muons, pions and protons in different materials.

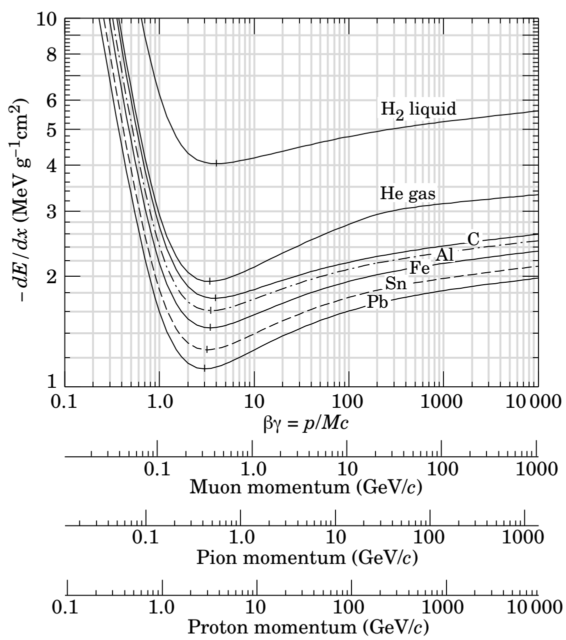

Figure 3.2: *Energy loss rate from ionisation as a function of $\beta\gamma$ for muons, pions and protons in different materials. [20]*

It is seen that at $\beta\gamma \sim 4$ the ionisation is at a minimum after which there is a slow rise, the so-called relativistic rise.

3.2.1 Nuclear scattering

For neutral particles in general, with the exception of photons, the energy loss mechanism is through scattering on nuclei. For each scattering the particle loses energy and hence the amount of energy lost when traversing a block of matter depends on the *interaction length* and the amount of energy deposited *per interaction*.

The nuclear interaction length λ_I of a particle travelling through matter is also called the *mean free path*, i.e the mean distance travelled between two interactions. It is determined by the total nuclear scattering cross section σ_{total} [20]:

$$\lambda_I = \frac{A}{N_A \rho \sigma_{total}}, \tag{3.1}$$

where A, N_A and ρ are the atomic number of the material, Avogadros number and the density, respectively. The total cross section is the sum of the cross section of *elastic* processes, which denotes processes in which the initial and final particles are the same, and *inelastic* processes, in which the out-going particles are not the same as the ingoing particles.

The scattering of light SM particles like pions has been studied extensively; pions are in general copiously produced at collider experiments. It is from these studies found that the behaviour is very different for the low and high energy regime [20].

In the low energy regime the cross section for scattering processes is very irregular and dominated by *nuclear resonances* which are short lived intermediate states. The processes are mainly $2 \rightarrow 2$ processes. The processes can be mediated either by the exchange of a quark-antiquark pair, a *Reggeon* or by the formation of resonances. If the Reggeon is a pion the cross section goes as $\sigma \propto 1/\sqrt{s}$, where s is the collision energy. For resonances the cross section goes as the Breit-Wigner shape for energies near the resonance energy.

In the high energy regime the scattering behaviour is of a more regular character. The processes are $2 \rightarrow N$ processes with $N \gtrsim 2$ and the total cross section is slowly rising for higher momenta but otherwise rather stable.

3.2.2 Hadronic calorimetry

Hadronic calorimeters are based on the strong interaction, not as in the direct exchange of a gluon between two quarks (which is short range). Rather the interaction can be described as a residual force analogous to the short range Van der Waal force between atoms resulting in molecular binding between atoms [8]; likewise this residual strong force is responsible for binding protons and neutrons in nuclei.

If a high-energy ($\gtrsim 5$ GeV) hadron enters a dense block of matter ineleastic as well as elastic collisions will take place between the hadron and the nuclei in the material. For each collision secondary hadrons are produced which are mainly pions, the lowest-lying quark-antiquark states of the up and down quarks and hence the lightest standard model hadrons. Part of the energy of the incoming hadron is transferred to the *secondaries* and they in turn can undergo inelastic collisions. If these secondaries have high enough energy *tertiary* hadrons will be produced. This process called a *hadronic shower* ends only when the hadron energies are so small that the hadrons are stopped by ionisation energy loss or absorbed in a nuclear process [21]. A calorimeter may either measure the energy of a particle in its entirety, requiring total containment of the particle shower, or it may be sampled. A hadronic calorimeter is always a sampling type which means its energy measurement is based on having an absorbing/passive material followed by a sampling/active one alternating in layers.

The produced secondaries (pions) can be neutral, negatively or positively charged. The neutral pion quickly decays to two photons. The energy detection is now done by the sampling of the ionisation energy deposit of charged particles plus photons in the active material. The active material is often a scintillator, a type of material which exhibits luminescence when excited by ionizing radiation. It can be a scintillating plastic, crystal, glass or gas.

3.3 ATLAS

The ATLAS detector is the largest particle detector ever built for a collider experiment. Figure 3.3 shows the components of the instrument to be described below.

The ATLAS experiment is put shortly a combined system of the collider providing the beam collisions, the detector and trigger/data-aquisition system along with computer farms providing data and the ATLAS software used when interpreting the detector output. You could add the several thousands physicist, engineers and technicians continuously working on the experiment.

The detector is designed to meet the following objectives [22]:

- the full tracking chain should be precise enough to efficiently reconstruct high transverse momentum leptons and to assist in the b-tagging and the τ reconstruction (NB omskrives).
- efficient identification of electrons and photons and reconstruction of their respective momenta and energies by electromagnetic calorimetry.
- a good resolution in missing transverse energy by the coverage and precision of the hadronic calorimeters, because many processes of interest have final state neutrinos
- high precision on the muon reconstruction should be obtainable using the muon spectrometer alone as high-luminosity running might infer occupancy-related problems in the ID tracking.

Requirements of the detector have been defined using a set of processes chosen to cover much of the phenomena one can hope to observe at the TeV scale [22]. These include: Higgs and top quark processes. The Higgs would be a very short-lived resonance and so to search for the Higgs is to search for its decay products or more precisely certain *patterns* matching a process with a Higgs. The Higgs has many decay channels depending on its mass, which leads to many different detector signatures but for all of these processes what will be searched for is ultra-relativistic particles with a high transverse momentum.

The standard coordinate system and some of the nomenclature used in the rest of this report are the following: the nominal interaction point is defined as the origin of the coordinate system, the beam direction defines the z-axis and the x-y plane is the plane transverse to the beam direction. The positive x-axis is defined as pointing from the interaction point to the centre of the LHC ring and the positive y-axis is defined as pointing upwards. In polar coordinates we have the azimuthal angle ϕ which is measured around the beam axis and the polar angle θ the angle from the beam axis; the pseudorapidity η is derived from the polar angle, defined as:

$$\eta = -\ln\tan(\theta/2) \tag{3.2}$$

Some values of η are shown in Figure 3.4. In the relativistic limit, $\eta \rightarrow y$, with y being the rapidity, a translational invariant in the z direction. The rapidity is defined as:

$$y = \frac{1}{2}\ln[(E + p_z)/(E - p_z)], \tag{3.3}$$

The initial momentum of the colliding partons is uknown, but the transverse component is well defined, hence values are often expressed in terms of their transverse components:

$$p_T = \sqrt{{p_x}^2 + {p_y}^2} = p\sin\theta, \tag{3.4}$$

$$E_T = \sqrt{m^2 + {p_T}^2}\cosh\eta, \tag{3.5}$$

$$\not{E}_T = -\sum_i p_T(i), \tag{3.6}$$

where the sum is over the momenta of all final state particles detected.

3.3.1 Detector parts

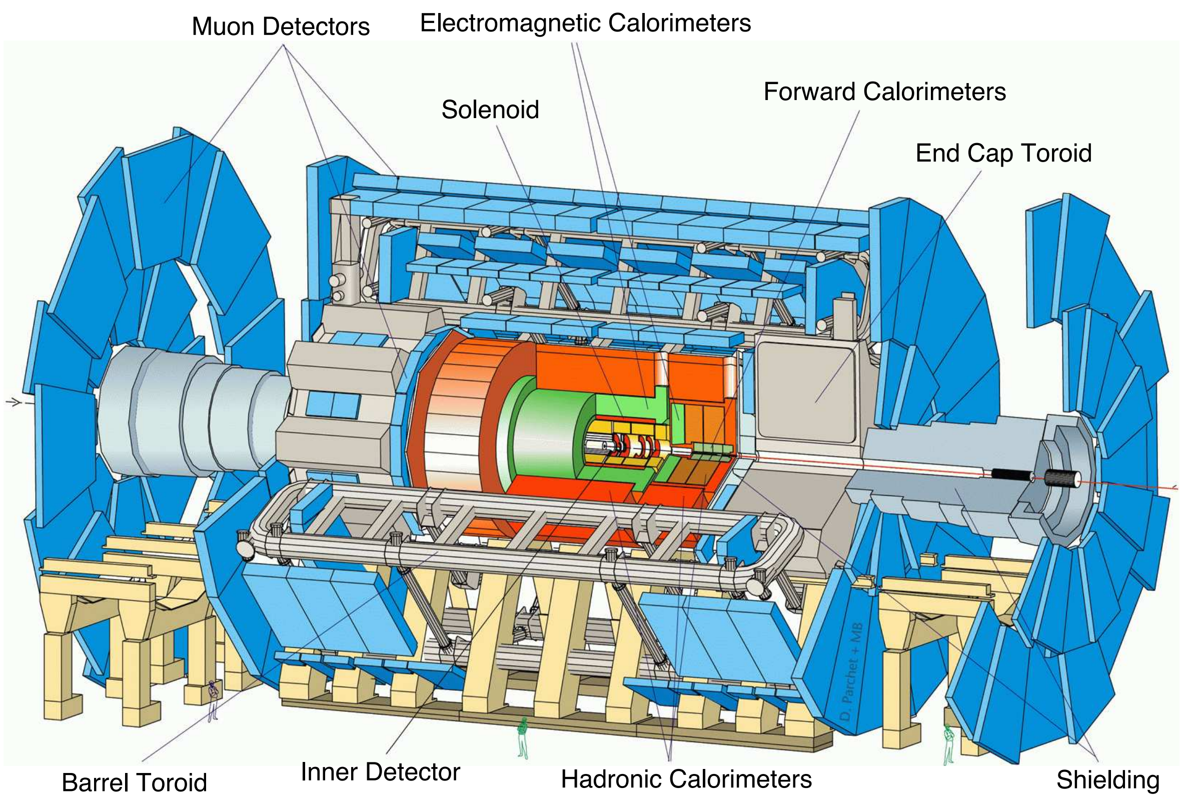

Figure 3.3: *The ATLAS detector. With its 46 m in length and 22 m in height it is the world's largest accelerator based particle physics detector. ATLAS Experiment © 2011 CERN.*

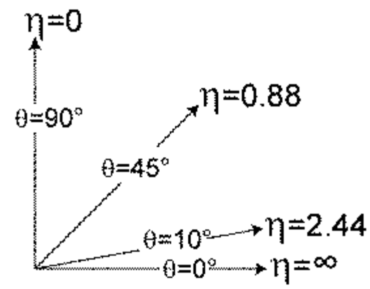

Figure 3.4: *Diagram of pseudorapidity with angular values. As angle increases from zero, η decreases from infinity. Wikimedia-Commons.*

3.3.2 The Inner Detector

Innermost of the ATLAS detector is the Inner Detector (ID) in a cylinder of length 7 m and radius 1.5 m. The ID consists of the Pixel Detector, the SemiConductor Tracker and the Transition Radiation Tracker, and measures with a high precision the tracks of charged paticles with an angular acceptance of $|\eta| < 2.5$ for the combination of all three ID parts. In order to be able to extract the momentum, the ID is enclosed in a superconducting solenoid magnet. The solenoid creates a uniform magnetic field parallel to the beam direction causing charged particle tracks to bend in the transverse plane, according to the Lorentz force law; the bending angle (or radius of the circular path) depends on the momentum (giving curvature) and charge (giving the direction of the bending). The momentum measurement is done by measuring the sagitta of tracks. The sagitta gives a measure of the degree of bending of a curve (see Figure 3.5. Since only charged particles leave a track all tracks will bend in the magentic field of the solenoid. In the near constant field the deflection depends solely on the magnitude of the momentum, P and the charge q of the particle, according to the equation [21]:

$$2\sin\frac{\theta}{2} = \frac{l}{r} = -\frac{qB_y l}{P}, \tag{3.7}$$

where B is the magnitude of a uniform magnetic field $(0, B_y, 0)$ of length l. The strength of the magnetic field (2 T) is so that a low transverse momentum particle ($\lesssim$ 400 MeV) of unity charge will be bent to circular motion (thus looping indefinately) whereas a high transverse momentum will effectively only be deflected by the bending.

The momentum extraction assumes unity charge of particles but doubly charged particles also appear like for instance α-particles; for such particles the bending will be stronger thus underestimating the momentum by a factor 2.

3.3.3 The electromagnetic calorimeter

The ATLAS electromagnetic calorimeter is a liquid argon calorimeter (LAr) consisting of two half-barrels. The structure of the calorimeter is like an accordion as shown in Figure **??**, the material alternating between a shower material (lead or iron) and liquid argon in a strong electric field generated by electrodes. Charged particles cause ionisation in the argon which is then picked-up by the electrodes. The calorimeter covers $|\eta| \lesssim 1.5$.

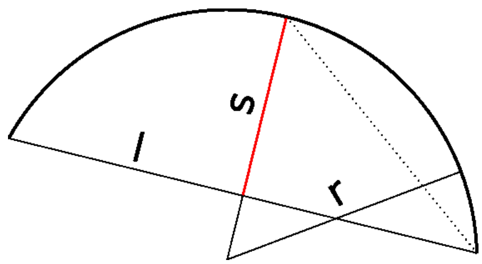

Figure 3.5: *Sagitta is the depth of an arc,* s, r *is the radius of the circle in which the arc is in, and* l *is one half the distance across the base of the arc. Wikimedia-Commons.*

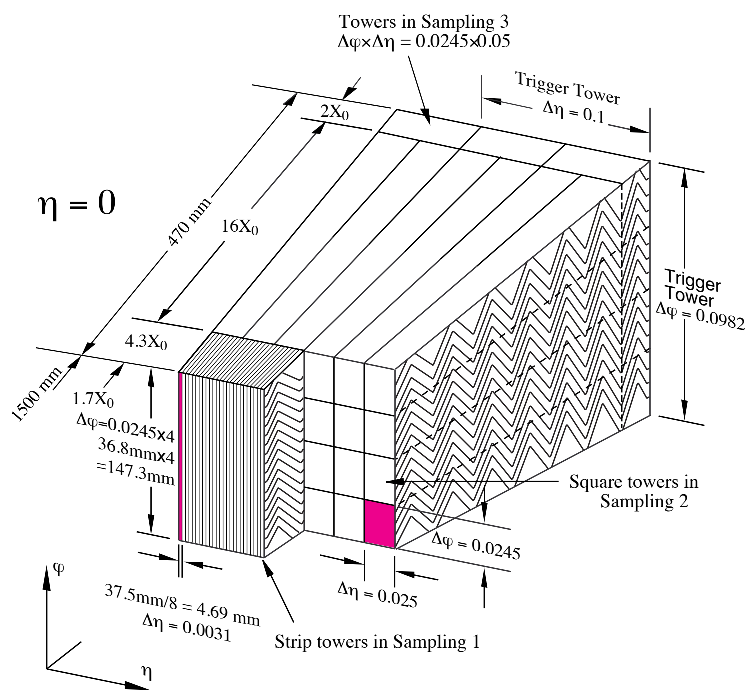

Figure 3.6: *The accordion structure of the ATLAS LAr calorimeter ensuring a good azimuthal coverage of the calorimeter. Trigger towers, described in 3.3.6, are also indicated in the figure. From [25].*

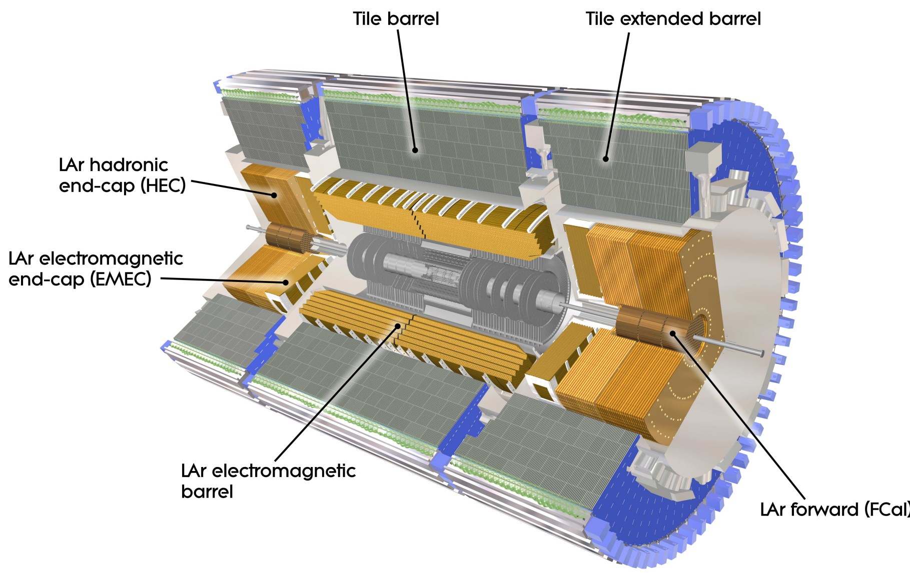

Figure 3.7: *View of the electromagnetic and the tile calorimeter with extended barrels and end-caps. ATLAS Experiment © 2011 CERN.*

3.3.4 The Tile Calorimeter

The ATLAS Tile Calorimeter is the barrel part of the hadronic calorimetry in the ATLAS detector located behind the liquid argon electromagnetic calorimeter, as seen from the primary interaction point (see Figure 3.7).

It is subdivided into an central barrel and two extended barrels each consisting of 64 modules or wedges of size $\Delta\phi \sim 0.1$.

The radial depth of the calorimeter is approximately 7.4 λ; where λ is the mean free path of a pion to suffer a strong interaction, i.e it is the mean distance a pion travels without ungergoing interaction with nuclei in the absorber; this characteristic length is also called interaction length and depends on the material. In iron $\lambda = 16.8$ cm.

The distance from the primary interaction point (IP) ranges from 2.3 m to 4.3 m. and the η coverage is $|\eta| < 1.7$

(which translates into an angular coverage of ~ 20 in degrees).

In the ATLAS tile calorimeter the tiles are composed of steel and scintillating plastic as depicted schematically in Figure 3.8; a photo of a single scintillator element is shown in Figure 3.9. Each of the 64 modules has between 1529 (extended barrel) and 3355 (central barrel) tiles giving a total of $\sim$ 463.000 tiles.

The scintillating light produced is blue or ultraviolet and in order to detect it, it is collected at the edges of each tile by wavelength shifting fibres, shifting the wavelength to the visible domain and guiding it to photomultipliers which are then read out. There are two fibres at each tile and they are grouped together and coupled to the photomultipliers in way such that a three-dimensional read-out cell structure is formed. The cell structure forms three

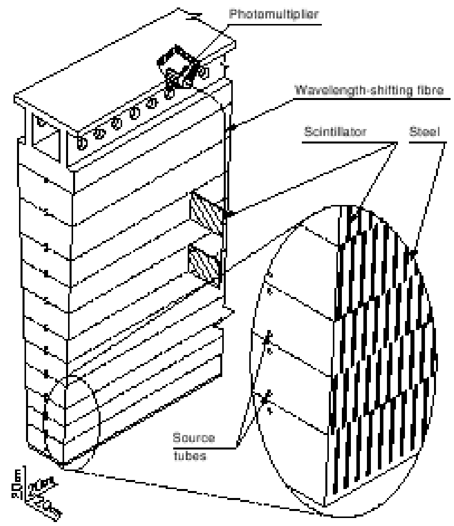

Figure 3.8: *Schematic view of a single tile calorimeter module showing the components: tiles, fibres and photomultipliers. From [26].*

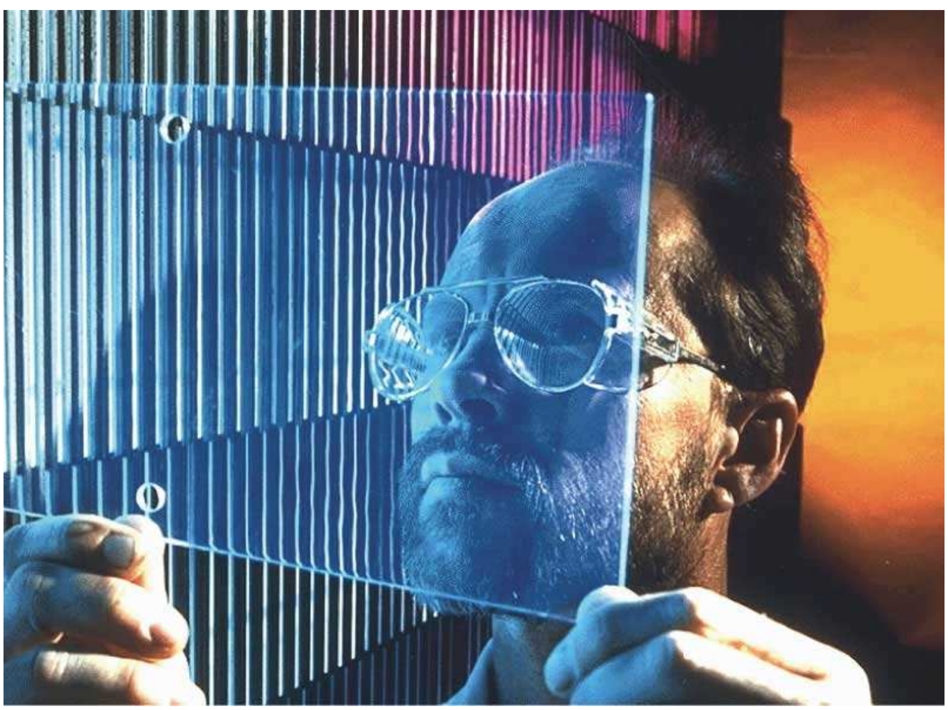

Figure 3.9: *A single scintillator element being inspected before assembly. ATLAS Experiment © 2011 CERN.*

radial sampling depths of approximately 1.5, 4.1 and 1.8 λ thickness at $\eta = 0$. The cells have dimensions $\Delta\eta \times \Delta\phi = 0.1 \times 0.1$ in the first (innermost) layers and 0.2 x 0.1 in the last layer; the structure is depicted in Figure 3.10.

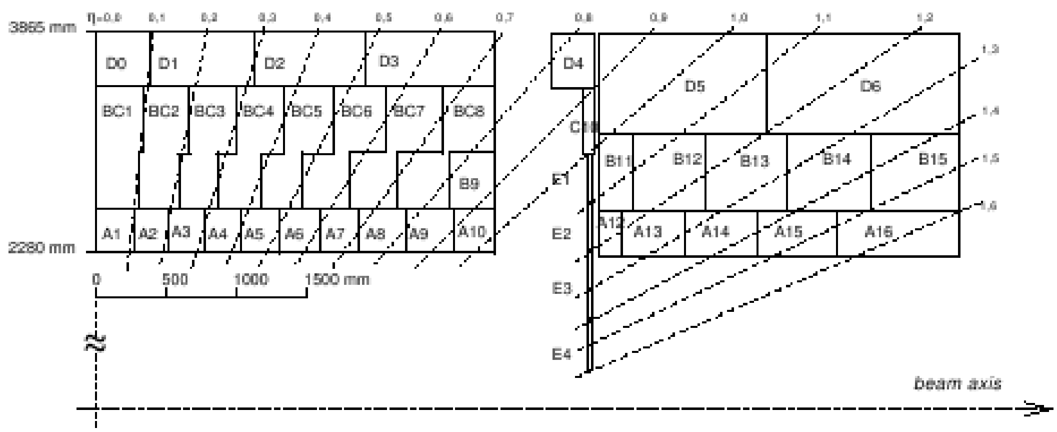

Figure 3.10: *Segmentation in depth and η of the tile modules in ATLAS tile calorimeter in the central (left) and extended (right) barrels. The bottom of the picture corresponds to the inner radius of the barrels and the top to the outer radius. From [22].*

A hadron can either punch through the detector or be stopped by the dense material depending on the interaction cross section and energy lost per interaction.

3.3.5 The Muon Spectrometer

The Muon Spectrometer forms the outer part of the ATLAS detector extending from approximately 5 m out to 10 m away from the beam axis.

The overall layout is shown in Figure 3.11 with indicators for the different regions in which four detector technologies are employed: thin-gap chambers, cathode strip chambers, resistive plate chambers and drift tubes; also shown with indicators are the toroid magnets.

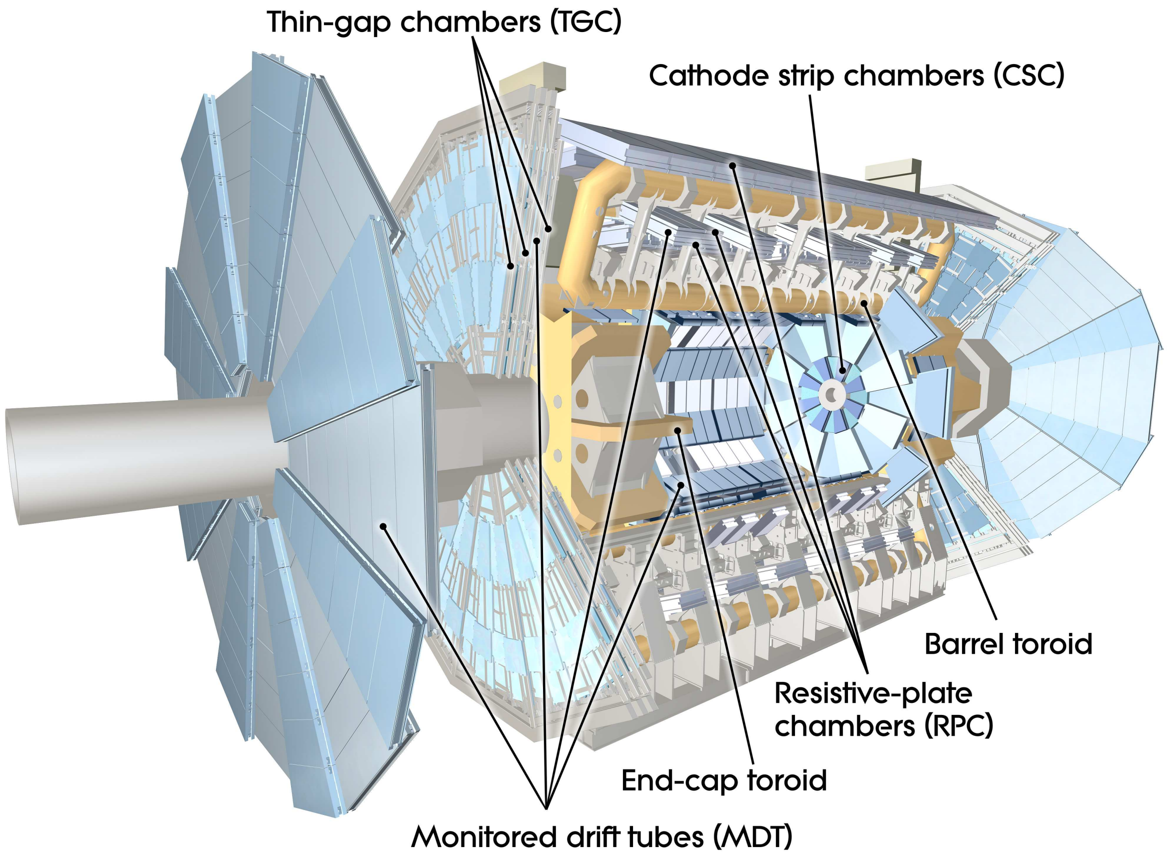

Figure 3.11: *The ATLAS muon spectrometer layout with detector parts and toroid magnets. ATLAS Experiment © 2011 CERN.*

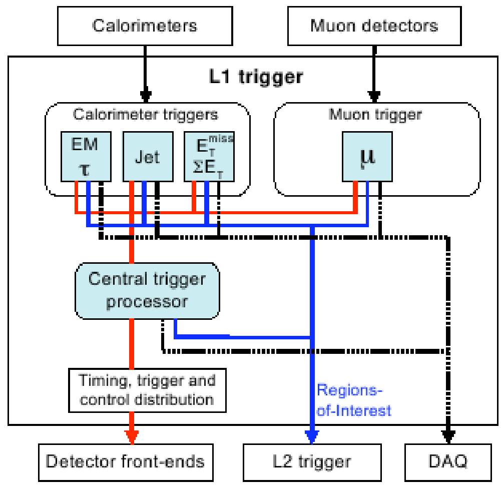

Figure 3.12: *Diagram of the L1 trigger showing the paths to the detector front-ends, the L2 trigger and the data acquisition system in red, blue and black respectively. ATLAS Experiment © 2011 CERN.*

3.3.6 The Atlas trigger system

Since the number of interesting events is orders of magnitude less than the total number of events and since there is not unlimited data storeage, a system to select the interesting events, and just as important, reject the overwhelming amount of uninteresting data is of vital importance.

The Atlas trigger system consists of three levels: Level 1, Level 2 and Event Filter. At each level the decisions made at the previous level are refined and additional selection criteria applied.

The trigger system operates simultaneously and in parallel with the data acquisition system, which receives and buffers, via electronics, event data from the read-out system at the L1 accept rate, see 3.12.

3.3.7 Level-1 trigger

Receiving data at each bunch crossing, when at the LHC design luminosity, the L1 must reduce the rate of ∼40 MHz down to ∼75 kHz. The High Level Trigger (HLT) further reduces the event rate to ∼200 Hz where the events to be stored are of size ∼1.3 MByte.

L1 uses a minimal amount of the total detector information in order to make a decision within 2.5 μs. The main objective of the L1 trigger is to search for high p_T muons, electrons, photons, jets, tauons decaying into hadrons, as well as large missing transverse energy.

The overall L1 selection is carried out by the central trigger processor using information from either the trigger chambers of the *muon spectrometer* or the *calorimeters*.
The decision is based on combinations of objects required in coincidence or veto. Because the luminosity varies over the run periods the trigger has to be *flexible*; the implementation is so that it can be programmed for selecting different signatures.

While being as inclusive as possible the L1 trigger must also meet the bound that the maximum rate at which the ATLAS front-end system can accept L1 triggers is 75 kHz (though upgradable to 100 kHz).
When accepting an event, *regions of interest* are formed and L1 also uniquely identifies the bunch-crossing number. The regions of interest (RoIs) are geographical regions in the detector where significant patterns have been "seen".

Events selected by L1 are read out from the detectors into readout buffers, where first intermediate buffers called *derandomizers* average out the the high instantaneous data rate at the output of the *pipeline* memories in order to match the maximum input bandwidth of the *readout drivers*. The full event data is kept while L2 algorithms run on RoIs.

The next and final step in the selection is the *Event Filter*; here the full event is read out from the temporary memory buffers and the final decision is made of whether to save the event on tape or not.

Considerations have included the transverse momentum (p_T) range over which the trigger must be able to operate and the required acceptance and efficiency to find the objects while taking into account constraints on the acceptable trigger rate. Other issues are the ability to resolve nearby objects while not double-counting single objects important for multi-object triggers such as di-electron and di-muon triggers.

The number of thresholds that can be concurrently used is constrained and different thresholds are used for single and multi-object triggers.

Because the LHC produces overwhelming amounts of data with a large amount of uninteresting events, the trigger menus are specialised for specific searches [23]. Evenso events like *minimum bias events* are needed for calibration and monitoring as well as validation of the detectors and also control samples are used for background evaluation studies, but since the cross sections of these kinds of events are high and only limited statistics are required these additional menu items suffers a hard prescaling. A prescale is a factor that can be set at each trigger level. At L1 it is an integer, so that for a prescale of N, one event out of N events, fulfilling the chain/threshold, leads to acceptance of the event. At the HLT each chain can be given individual prescales of any number value.

The geometrical acceptance of the L1 trigger is driven by the design of the detector, where precision measurements in the calorimeters and the coverage of the inner detector are limited to pseudorapidity, $\eta < 2.5$. The muon, electron/photon and hadron/tau triggers are required to cover this range ($\eta < 2.4$ in the case of the muon trigger).

For the jet trigger, the calorimeter trigger towers that are used extend up to $\eta < 3.2$, the edge of the endcap calorimeters. The missing and total scalar transverse energy (E_T) triggers use all of the calorimeters, giving a coverage of $\eta < 4.9$. Also important for L2 is the accuracy with which the position of the object within the detector can be specified by L1.

The trigger conditions (e.g. thresholds and multiplicity requirements) must be programmable to be able to adapt to different luminosity conditions and changing physics requirements. There must be sufficient flexibility to cope with unforeseen background conditions or new physics.

Summing up on the physics performance considerations of the L1 trigger it is repeated that the objects upon which the L1 trigger is based are high-pT muons, electrons/photons,

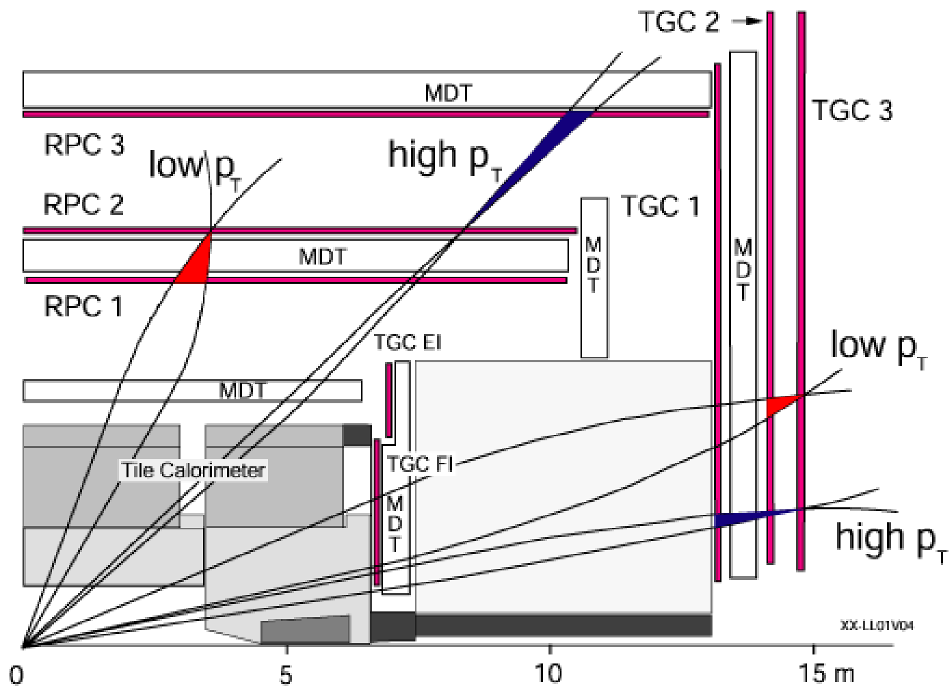

Figure 3.13: *ATLAS Muon Trigger, low p_T muons are in the barrel identified as coincidence between the middle resistive plate chamber (RPC) layer and one other layer and high p_T muons as coincidence between all three layers figure. ATLAS Experiment © 2011 CERN.*

hadrons/taus and jets, and large missing and total scalar ET.

Muon Trigger

For the L1 muon trigger, the muon spectrometer *thin gap chambers* and *resistive plate chambers* are used. Both high and low p_T muons are seached for in the barrel and end-caps of the muon system. There are three resistive plate layers. Low p_T muons are in the barrel identified as coincidence between the middle layer and one other layer and high p_T muons as coincidence between all three layers, as depicted in Figure 3.13. In the end-cap the strategy is similar, but using thin gap chamber layers instead of resistive plate chambers.

Calorimeter Trigger

The calorimeter trigger is more complicated, designed to identify high-E_T electrons, photons, jets and tauons decaying into hadrons and events with large missing E_T as well as large total E_T.

In order to be fast the L1 calorimeter selection is based on reduced-granularity information, whereas the HLT uses the full granularity and precision available within the RoI which is at the order of 2 % of the total event data.

The L1 calorimeter trigger algorithms get *trigger towers* as input, of granularity 0.1×0.1 in $\eta \times \phi$, which are formed by analogue summation of calorimeter cells, as shown in Figure 3.14.

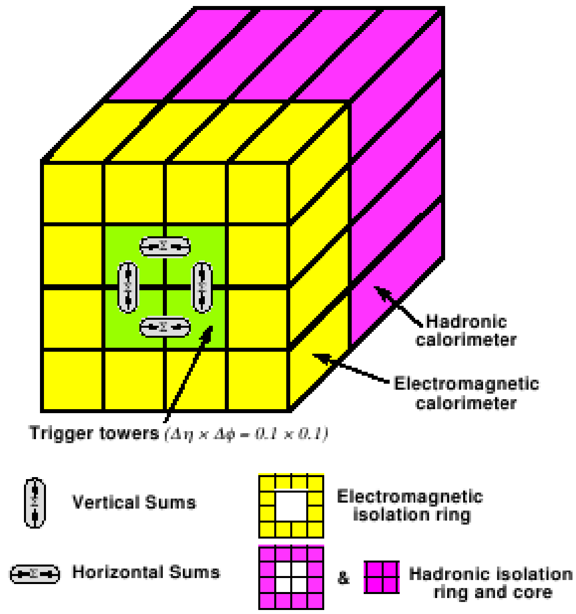

Figure 3.14: *Trigger towers used in the calorimeter triggers. From ref. [24].*

Three main subsystems process the calorimeter output: the *preprocessor* digitizes the analogue input signals and tags the signals with the bunch crossing number. The data is then sent in parallel to the *cluster processor* and the *jet/energy-sum processor*. The cluster processor identifies electron/photon and τ-lepton candidates with E_T above (a programmable) threshold and satisfying (if required) isolation criteria. The *jet/energy-sum processor* receives jet trigger elements, which are sums in $\Delta\eta \times \Delta\phi$ of 0.2×0.2 and from these identifies jets and forms sums of scalar energy and missing E_T.

Both subprocessors count the multiplicities of the different types of trigger objects and sends this information as well as the E_T information to the *central trigger processor*, which then accepts or rejects the event. In case of acceptance information is passed to the *RoI builder* for use by L2.

In the cluster processor e/γ algorithms search for narrow, high-E_T showers in the EM calorimeter demanding isolation and that the showers do not penetrate to the hadronic calorimeter. The $\tau/hadron$ algorithm looks for τ decays into collimated clusters of hadrons, with a looser isolation requirement and allowing the showers to penetrate into the hadronic calorimeters.

The jet energy sum processor carry out the jet algorithms and count the multiplicity while also serving as the first stage of the missing E_T and total E_T triggers, by summing the E_T components E_x and E_y, and the total E_T, over the region covered. Here the granularity is more coarse than for the e/γ and $\tau/hadron$ algorithms, and there is no need to keep electromagnetic and hadronic calorimeters separate. The jet energy sum processor then work with "jet elements" which are the sum of 2×2 trigger towers in the electromagnetic calorimeter added to 2×2 trigger towers in the hadronic calorimeters, giving a basic granularity of 0.2 in $\Delta\eta$ and $\Delta\phi$ except for the jet elements in the outer regions of η which are 0.3×0.2. The total scalar E_T is calculated as the sum of all jet elements and for the missing E_T the E_x and

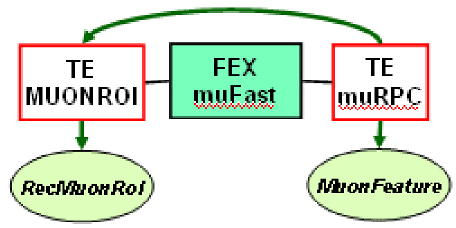

Figure 3.15: *Trigger sequence diagram illustrating how trigger elements, TEs, are inputs for trigger algorithms outputting new trigger elements. Here the FEX "mufast" receive a RoI TE and outputs a resistive plate chamber, RPC, feature TE. ATLAS Experiment © 2011 CERN.*

E_y components are calculated by multiplying each jet element by the appropriate geometrical constant.

Regions of Interest

The RoI objects are based on and optimized for high p_T fundamental SM particles and jets. For instance a muon RoI item corresponds to a signal above threshold in the muon systems which has been calibrated to muons. There are six programmable threshold settings optimized so that for instance a muon of p_T=20 GeV has a 95% chance of passing as a 'MU20' item. SM particles other than muons can feign a muon but are usually highly unlikely to penetrate through to muon system. R-hadrons have a high probablity of punching through as will be seen in section 4.3.1 and this can be exploited for triggering.

3.3.8 The High-Level Trigger

At L2 chains of algorithms run on RoIs passed by L1.

Each chain is *seeded* by a L1 item which corresponds to a passed threshold in either the muon system or the calorimeter or a combination thereof. After seeding the L2 algorithms can also run over data from the inner detector thus refining the selection.

The algorithms are classified into two groups: feature extracting (FEX) algorithms and hypothesis (Hypo) algorithms.

The first variety is dedicated to extracting event features to form and support a hypothesis of what was in the event. The advantage of this classification is that several Hypo algorithms can make use of the output TEs of one FEX, running only once.

The hypothesis algorithms then will check for passed criteria like energy or isolation and do a selection resulting in the output of a trigger element.

Several features can be combined and the algorithms run either parallelly or serially on the event.

The chains are built by adding sequences corresponding to signatures. A typical sequence consists of a FEX and a Hypo algorithm. The FEX algorithms receive trigger elements (TEs) from L1 and forms new TEs to pass on to the next algorithm in the chain as shown in figure 3.15 where a region of interest TE is processed by the algorithm "muFast" which then forms

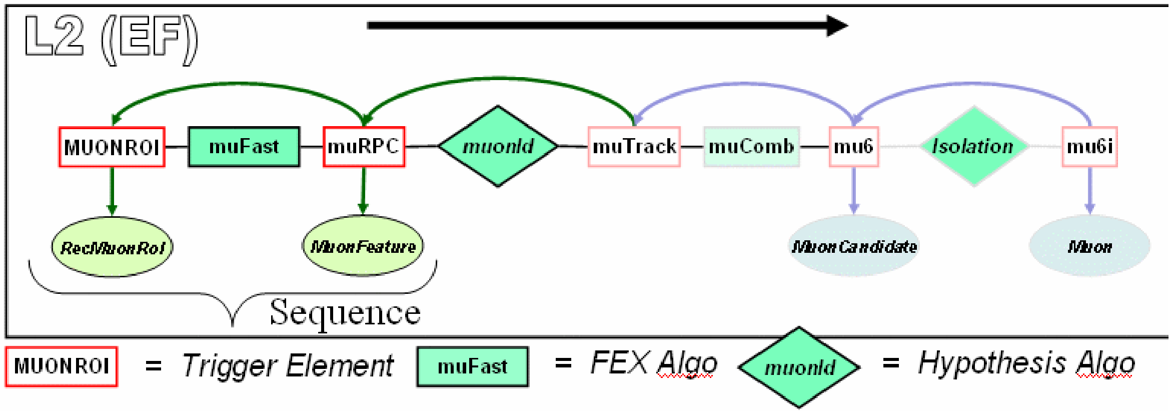

Figure 3.16: *Trigger Chain composed of four sequences. The chain consists of two FEX algorithms and two Hypo algorithms with trigger elements being passed from algorithm to algorithm and each step refining the selction. ATLAS Experiment © 2011 CERN.*

a feature TE from the output of the muon resistive plate chamber (RPC) to pass on.

In figure 3.16 a visualisation of a chain, beginning with the sequence desbribed above, is shown, with the passing of a TE to the algorithm “muon id” which then outputs track TEs and so on until the last step “isolation”, where candidates are accepted or rejcted as *muons*. At each step/sequence the chain is abandoned in case no signature is found. The chains terminate at the last Hypo algorithm where the decision of passing to the Event Filter or not is made.

After acceptance at L2 the full detector read-out is passed to the *Event Filter* comprising the hardware and sofware required for the final stage of the on-line selection using *off-line style* algorithms and full granularity detector read-out.

Chapter 4

Trigger for Stable Massive Particles

4.1 Simulation of experiments

A very important part of modern particle physics is data simulation using Monte Carlo methods.

The role of simulations is to attempt to predict the behaviour of phenomena at unprecedented energy regimes and to test the validity of models describing phenomena at known energies.

Comparing simulations with real data reveals the predictive power of theories.

Here it will be used to estimate the efficiency of triggers for SMPs. The reliability of the result depends on the quality of the simulation of the detector and on the GEANT 4 models for the interactions of SMPs in matter.

The simulation begins at the primary collision of fundamental particles where new particles are created. In processes resulting in the propagation of leptons and colourless bosons perturbative calculations are carried out and often the leading order or next-to-leading order approximation is satisfactory. These calculations include initial and final state radiation (ISR and FSR) of gluons and photons from the primary particles.

When the process result in outgoing quarks and gluons the perturbative picture falls short because these particles are colour-confined, resulting in the formation of jets of colourless hadrons.

In ATHENA, the official ATLAS software framework, the event generation and hadronisation if needed is often done using PYTHIA. In PYTHIA the calculation gets subdivided into steps: the hard process, calculated in perturbative QCD generates a number of elementary particles which are run through a so-called “parton shower”. A parton shower exploits the collinear limit of QCD to approximate a prediction of the final number of fundamental particles in the event. These are then passed on to hadronisation, where (using different models) partons are combined to form hadrons, thus giving a complete prediction of the final state particles in the event. This strategy reproduces to some accuracy the average behaviour of real data from accelerators [27]. In real data, fluctuations arise from quantum mechanics underlying the processes, which are based on amplitudes. In a Monte Carlo generator, probabilistic techniques are used to models this behaviour, and hereby interference phenomena are lacking in the modelling. However it is rare that this modelling is insufficient in approximating observed phenomena [27].

After hadronisation the simulation continues with the detector simulation. for official ATLAS samples it is GEANT 4 which computes how particles traverse the detector material, respond to the magnetic fields, shower in calorimeters etc.

The output of GEANT 4 corresponds to energy depositions produced by particles interacting with the detector material. The digitization step then converts this input to correpond to the raw electrical signals produced by the detector. From here the reconstruction into measurable quantities is carried out by Athena, the ATLAS software framework.

After the step of digitization simulated data and real data is ideally equal, when comparing sets of sufficient statistics, and of course provided that there is congruence between the model(s) in question and the true nature of phenomena.

Models for the interactions of R-hadrons has been developed and implemented in the detector simulation software GEANT4 which is incorporated in the official ATLAS simulation software; the models are described in more detail in refs. [28] and [29].

4.2 Stable massive particles at the LHC

As noted in the theory section there are many different theoretical scenarios that lead to the existence of SMPs. In this work attention is paid to the ones that are relevant in the context of the experimental facility at hand, the LHC.

4.2.1 Stable massive particle production

Firstly, the energy attainable in collisions sets the mass range of particles discoverable.

The collisions of fundamental partons allow for creation of new particles from the available energy.

The mandelstam variable s, a relativistic invariant, is defined as [9]

$$s = (p_1 + p_2)^2 = (p_3 + p_4)^2 \tag{4.1}$$

with p_1 and p_2 being the 4-momenta of the ingoing particles, and p_3 and p_4 that of the outgoing particles. The $\sqrt{s}$ is equal to the total energy in the center-of-momentum frame.

The design collision energy is 14 TeV at the LHC, but so far the maximum collision energy has been 7 TeV, still being the current world record as it superseedes the collider which previously claimed this title, the Tevatron, by a factor of $\sim$3.

It must be noted that the maximum $\sqrt{s}$ in collisions is not the typical *parton* collision energy. Where the $\sqrt{s}$ of the two colliding protons does not fluctuate much, that of the partons do. The fraction of the proton momentum carried by each parton follows a distribution which depends on the momentum transfer in the process. The *parton distribution functions* (PDFs) express the probability of given partons to carry the momentum fraction x of the total proton momentum [8]. PDFs are not calculable from first principles due to the non-perturbative properties of the binding of partons in hadrons; they are found from performing fits to *data*;

PDFs introduce a systematic error at LHC due to the energies at LHC being a new frontier opening up the low-x regime [30].

Assuming SMPs to be pair-produced, as is a reasonable assumption for any theory involving a conserved quantum number, the upper mass limit on particles that can be produced is at the order of at the very maximum 7 TeV when at the LHC design collision energy of 14 TeV; however it must also be noted that,

- in order for particles to be directly detectable (as opposed to being detected through decay products) excess energy must be available to give a non-zero velocity so that they would traverse the detector or parts thereof
- most production cross sections fall roughly exponentially with the mass for a given collision energy, and in order to be able to claim a discovery sufficient statistics must be available within the lifetime of the experiment.

Still this should leave several TeV for the upper limit on the mass of a LHC-detectable particle, even at the currently relevant collision energy of 7 TeV. This means that a discovery window is opened by the LHC for particles of masses up to the TeV scale.

In March 2011 new limits were set on the mass of R-hadrons based on SUSY gluinos, sbottoms and stops based on a data sample from ATLAS of integrated luminosity $34.4pb^{-1}$. These new limits, the most restricive to date, are as follows for gluino, stop and sbottom respectively: 586, 309 and 294 GeV [31].

The production cross section depends on which theoretical model is assumed, and can when all parameters are set be calculated for a given collision energy as in Figure 4.1 where the production cross section of $\tilde{g}\tilde{g}$ as a function of $\tilde{g}$ mass for proton-proton collisions with a center of mass energy of 7 TeV is shown. All other SUSY masses are assumed to be high enough to decouple completely from the process. There is approximately exponential fall-off with the the mass for a given collision energy.

4.2.2 Case Study Specifications

In order to carry out a simulation a specific scenario must be chosen. With all parameters set a model can be quantitatively explored; one can simulate samples of events and let them undergo detector simulation.

For the samples used in this work, it is in the case of $\tilde{g}$ R-hadrons aso-called split-SUSY scenario that would generate the phenomenological model. The specific split-SUSY model can then be said to be the scene for this case study; squarks will also be tested, but here the models are a kind of “toy” models, not generated in a consistent phenomenology as the masses of all other sparticles are set to be arbitrarily high. However squark SMPs are predicted in *gauge-mediated SUSY breaking* scenarios [12]. In the case of charged SMP is used a phenomenological model based on SUSY with gravitino Dark Matter.

While the above show that the models tested are theoretically justified it is asserted that the trigger results are relevant for any theoretical scenario leading to coloured or charged SMPs with the uncertainties regarding interaction with matter.

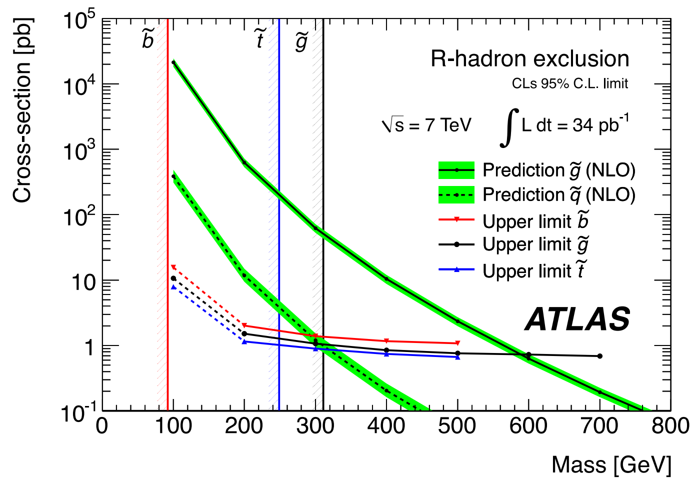

Figure 4.1: *Split-susy $\tilde{g}, \tilde{t}$ and $\tilde{b}$ pair production cross section at $\sqrt{s} = 7TeV$, with the lower limits on the mass of R-hadrons based on such SMPs at 95% confidence level, obtained from $34pb^{-1}$ of recorded ATLAS data. From ref. [31].*

Four kinds of particles will be used to test the trigger: $\tilde{g}$, $\tilde{t}$, $\tilde{b}$ and $\tilde{\tau}$.

Pair-production is assumed in all cases.

4.2.3 Kinematics

In order to get an overview of the character to be expected of R-hadron events three samples of 1000 events containing a gluino-based R-hadron pair have been generated privately with PYTHIA 6, with the mass of the gluino set to 300, 700 and 1000 GeV, respectively with a collision energy of $sqrts$=7 TeV.

This preliminary study is to give a feel for the kinematics and geometry to be expected for R-hadron events.

In Figure 4.2 is shown the distributions of β of the R-hadrons for the three mass points. Also shown, marked red, is the distribution for $|\eta|$ <1.7, i.e within the acceptance of the Tile Calorimeter.

The distributions are rather wide which means that at 7 TeV values in all of the range from 0 to 1 are to be expected.

The mean value is well below unity and for m=700 GeV and m=1TeV the distribution is completely separated from unity. The higher the mass the lower is the mean β because less energy is available to boost. Note also that the higher the mass the more particles survive the η-cut because the higher the mass, the more central is the event.

Figure 4.3 shows the transverse momentum distribution of the three mass points also with the distribution for $|\eta|$ <1.7 in red and here it can be seen that the distribution widens as mass increases which is expected since $\sqrt{s}$ are identical for the two distributions. Also it is seen that the $|\eta|$-cut only has effect on the low-end side of the spectrum.

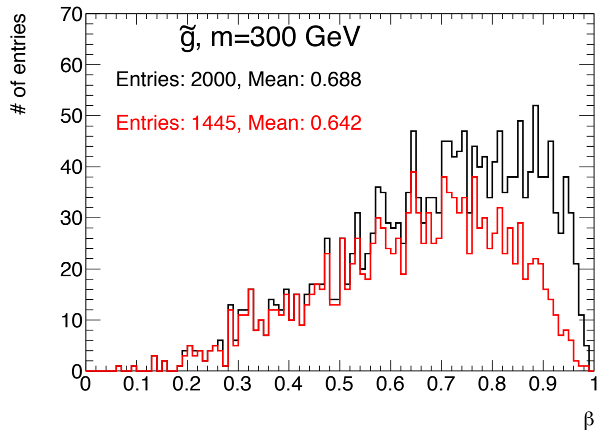

(a)

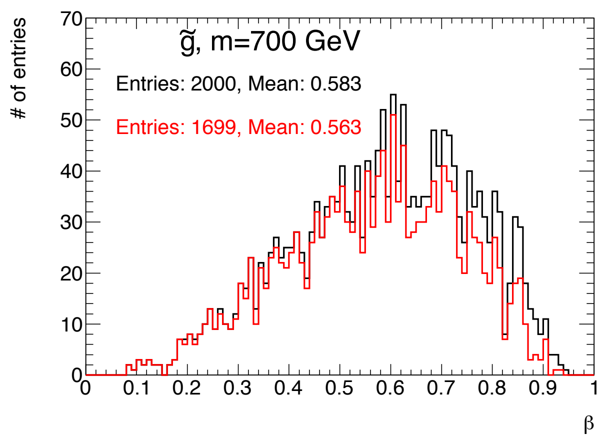

(b)

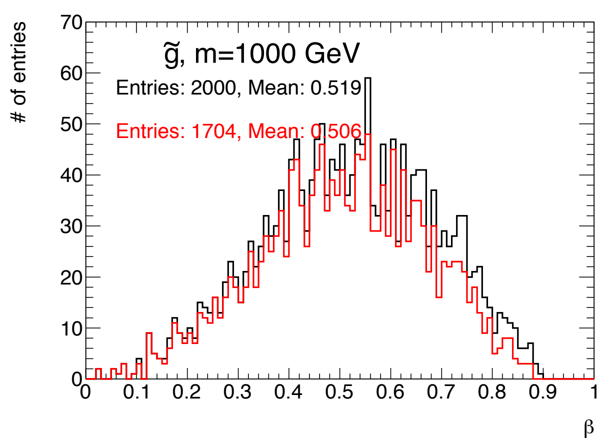

(c)

Figure 4.2: *β distribution of pair-produced $\tilde{g}$ R-hadrons, for 1000 events generated with Pythia 6 at the leading order at $\sqrt{s} = 7$ TeV, for the mass points (a) 300 GeV, (b) 700 GeV and (c) 1000 GeV. Also shown (red plot) is the distributions after demanding $|\eta| < 1.7$ corresponding to the coverage of the ATLAS Tile Calorimeter. The samples are not official, but are produced "privately".*

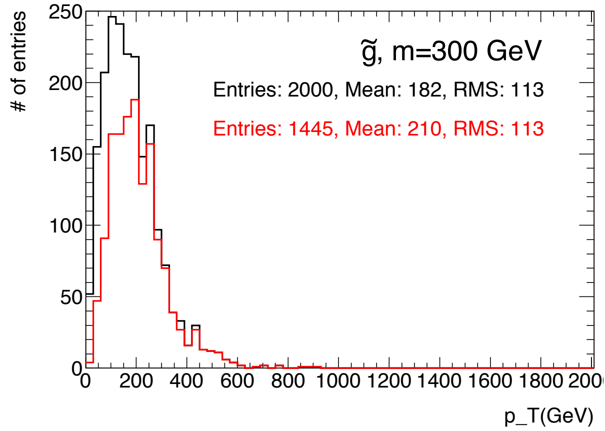

(a)

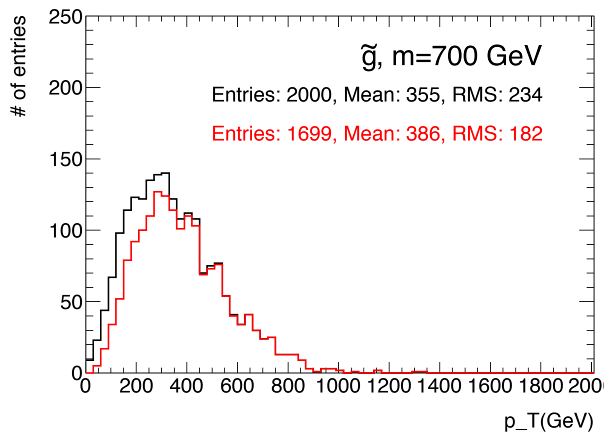

(b)

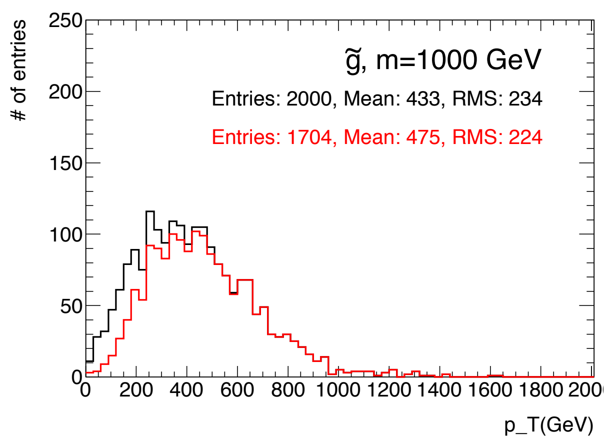

(c)

Figure 4.3: *p_T distribution of pair-produced $\tilde{g}$ R-hadrons, for 1000 events generated with Pythia 6 at the leading order at $\sqrt{s} = 7$ TeV, for the mass points (a) 300 GeV, (b) 700 GeV and (c) 1000 GeV. Also shown (red plot) is the distributions after demanding $|\eta| < 1.7$ corresponding to the coverage of the ATLAS Tile Calorimeter. The samples are not official, but are produced "privately".*

4.2.4 Interactions of heavy exotic hadrons

A particle carrying colour charge cannot exist as a free particle at the energy provided by the pp collisions at LHC. It would, because of colour confinement, hadronize, before entering the detector, into a bound state with either one or more quarks or a gluon, like for instance in the case of a $\tilde{g}$: $\tilde{g}$-$q\bar{q}$, $\tilde{g}$-qqq, $\tilde{q}$-$\bar{q}$, $\tilde{q}$-qq (R-hadron), $\tilde{g}$-g (gluino-ball).

Most likely it would form a bound state with some combination of the lightest quarks, the *uds* quarks.

Mass hierarchy

Given the mass of the SMP one may ask what would be the mass of the R-hadron it would form? For hadrons in general mass calculation models are semi-empirical and there are different ways of modelling the effects leading to observed masses.

The term *constituent mass* denotes the mass of the free parton plus a correction from the interaction with the remaining partons.

Bag models are models that assume non-interacting partons in a spherical cavity. Lattice QCD can also be used to calculate hadron masses and all these techniques have been used to predict features of R-hadron mass spectra making it possible to approximately determine the features relevant for modelling the interactions [29]. These predictions have been implemented in GEANT4, and are described below.

Because hadronic interactions can cause R-hadrons to convert from one state to another, i.e change light quark system (as will be described in next subsection) it is important to know what the energetically favourable states are. Conversions leading to lower masses are exothermic and thus preferred.

Calculating expected R-hadron masses is nontrivial and includes considerations on the allowed symmetry states of the relevant wave functions including possible spin states. A constituent model calculation for squark-based R-hadrons is treated thoroughly in [20] and I will here only refer the main points. It is used that interactions of heavy quarks with light quarks are observed to be spin and flavour independent and the lightest squark-based meson and baryon states are inferred from the mass spectra of charm and bottom hadrons.

The calculation gives with some approximation that neutral and charged squarm-mesons are mass degenerate and that the lightest baryon state is the state $\tilde{q}ud$. Also it is found that the decay of a baryon into a meson and proton is forbidden by kinematics.

The mass spectrum and scattering of gluino based R-hadrons is known with less confidence; squark R-hadrons have SM analogues with heavy quarks, but there are no massive gluons to extrapolate from.

Different techniques estimates that the masses of gluino mesons are the gluino mass plus 0.2-0.7 GeV with mass splitting of the lowest lying baryonic states less than the pion mass [29]. The lightest state is $\tilde{g}uds$ with $\tilde{g}udd$ and $\tilde{g}uud$ 0.2-0.3 GeV heavier leading to the prediction that $\tilde{g}udd$ and $\tilde{g}uud$ would decay weakly to $\tilde{g}uds$ within a timescale of $\sim 10^{-10}$s [29].

4.2.5 Interaction of R-hadrons

Electromagnetic interactions

The electromagnetic interactions of charged R-hadrons are well understood [32]. The continuous ionisation losses in the calorimeter are described by the Bethe-Bloch equation and are considerable when $\beta \ll 1$. Coulomb scatterings change the particle trajectory, but as the deflection angle is proportional to $(1/\beta \mathrm{p})$ it is small as p is large due to the large mass of the heavy parton [32]. A charged R-hadron produced with very low β are expected to be stopped, and detection methods in this case are being studied within the ATLAS collaboration, but are not within the scope of this work.

Hadronic interactions

The nuclear interactions have uncertainties, but it is predicted that the hadronic interaction of the heavy parton with the detector material is supressed relative to the light quark system [28], since the spatial extent of the wave function of a particle is inversely proportional to the mass according to the uncertainty principle. Thus the heavy parton can be seen as a reservoir of kinetic energy, and when the light quark system suffers energy losses it immediately regains kinetic energy through strong interaction with the heavy parton.

The effective interaction energy of the R-hadron is small, as can be seen by considering a $\tilde{g}$-$q\bar{q}$ state with constituent quark masses of 300 MeV as is often the value for qualitative considerations [32]. One can estimate the typical kinetic energy of the light quark system using the results from the pythia study ; in Figure 4.2 the β mean values are seen, they are approximately 0.5, 0.6, 0.7 for the masses of 300, 700 and 100 GeV respectively.

For $m_{\tilde{g}}$=700 the Lorentz factor becmoes $\gamma \approx$1.7. The kinetic energy of the interacting system is $T = m_{q\bar{q}}\gamma - m_{q\bar{q}}$=0.42 GeV, i.e less than 1 GeV. This means that the reactons to be seen are on average low energy.

Recall from section 3.2.1 that in the low energy scattering regime the behaviour is irregular due to resonances. Here uncertainty arise as possible resonances of R-hadrons are not known, however it is not expected to play and important role [32].

The solution in the implemented models concerning the above is to treat the R-hadron as a black disk [32] based on the line of arguments that: in the regime of high center-of-mass energies cross sections are for SM hadrons approximated by the geometrical cross section; the behaviour of SM hadrons in the low energy regime are effected by causes not present or not known to be present for R-hadrons.

The geometric cross section is then tuned to $\pi - p$ scattering; each light quark is assigned a total cross section of 12 mbarn leading e.g. to at value of 24 mbarns for a meson carrying a $\tilde{g}$ [32]. The contribution for an s quark is set to 6 mbarn [32].

For squark based R-hadrons processes in which R-mesons convert to R-baryons are exothermic and hence are expected to take place. The reverse processes would be kinematically disfavoured and be further supressed since the R-baryon would have to interact with a meson or antibaryon state in order for it to lose its baryon number [28] and mesons are not present in the detector-material in amounts comparable to baryons.

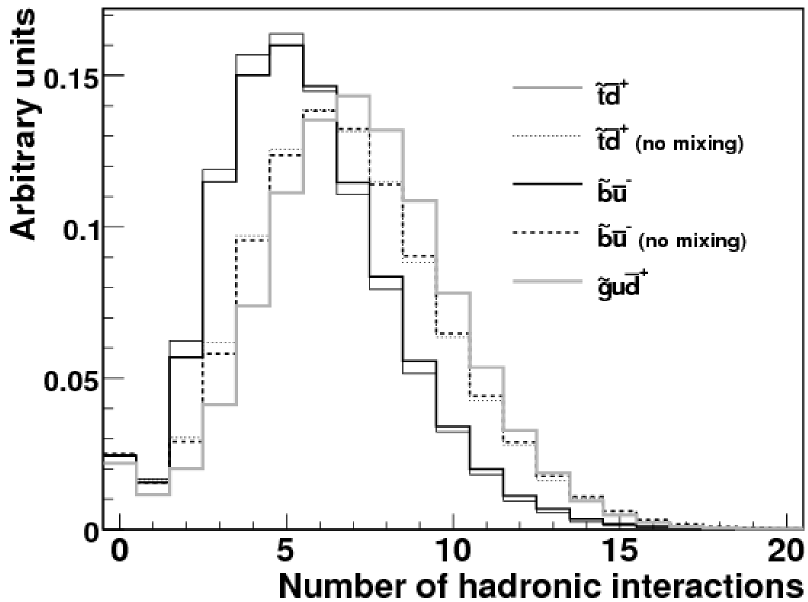

Figure 4.4: *Number of hadronic interactions of different types of R-hadrons when traversing 2m iron. From Ref. [29].*

It has also in Ref. [29] been calculated that the number of hadronic interactions when traversing 2 m of iron lies in the range 0-15 as seen in Figure 4.4

In GEANT 4 three different scattering models for R-hadrons are available. Each of them make use of the heavy parton being solely an energy reservoir.

The model that can be characterized as being the most inclusive is the *generic* model. It asumes a non energy dependent cross section and both 2-2 and 2-3 processes are included, with phase space factors weighting individual processes. It also assumes R-baryons to be degenerate and thus not decaying to a single low lying mass state.

The *intermediate* model use same scattering model as the generic model but differs in assuming a $\tilde{g}$ mass spectrum based on bag model calculations, this model only applies to $\tilde{g}$s [28], [33], [29].

The *regge* model assumes a cross section based on low energy hadron scattering and calculates energy losses using *triple regge* formalism [34] and is appropriate for treating squarks.

4.2.6 Samples

In Table 4.1 the MC samples used for testing the trigger efficiency are listed. The samples are official ATLAS samples, produced by the ATLAS central production, except for the $\tilde{\tau}$-sample which is generated privately, all are generated with Pythia 6.4 assuming $\sqrt{s} = 7TeV$. The prepended *mc09* stands for Athena MC-release and the difference between *mc09* and *mc10* is that *pile-up* is not simulated in mc09, but is so in release 10. The m=1000 GeV $\tilde{g}$ is the only sample used which is from MC-release 10.

The data format is the so-called RDO-format, *raw data object* which corresponds to the detector output before any reconstruction has taken place.

Mass(GeV)	Int. Model	sparticle	ID	No.events
700	generic	$\tilde{g}$	mc09_7TeV.114766	10.000
1000	generic	$\tilde{g}$	mc10_7TeV.114769	10.000
700	intermediate	$\tilde{g}$	mc09_7TeV.114826	10.000
500	regge	$\tilde{t}$	mc09_7TeV.114864	10.000
400	regge	$\tilde{b}$	mc09_7TeV.114873	10.000
152	electromagnetic	$\tilde{\tau}$	non-official, mc10	5.000

Table 4.1: *Signal samples, official.*

Table 4.2 lists the samples used for estimating the efficiency in rejecting events with no R-hadrons. Any SM process is a background to R-hadron events/signals, but only the ones with a large cross section need to be rejected at the trigger level. Ws, Zs and top-pairs are produced in large amounts at LHC and QCD jets even more copiously.

Background	Sample	No.events	σ(pb)
$t\bar{t}$ (semi-)leptonic	mc09_7TeV.105200.T1_McAtNlo_Jimmy	10.000	1.442×10^2
$W \to \tau\nu$	mc09_7TeV.107054.PythiaWtaunu_incl.digit.RDO	10.000	8.824×10^3
$Z \to \tau\tau$	mc09_7TeV.106052.PythiaZtautau.digit.RDO	10.000	8.486×10^2
$Z \to \mu\mu$	mc09_7TeV.105145.PythiaZmumu.digit.RDO	10.000	8.543×10^2
QCD di-jets	mc09_7TeV.105010.J1_pythia_jetjet.digit.RDO	10.000	6.781×10^8

Table 4.2: *Background samples, official.*

4.3 Trigger for long-lived heavy exotics

4.3.1 Event characteristics and R-hadron challenges

In this section common features of events, with either of the different types of SMPs and which could distinguish SMP events from SM events, will be considered. R-hadrons pose the most challenges as compared to sleptons.

Delay of signals

It is general to most searches and SM processes at the LHC, that the particles expected to be seen (reconstructed) in the detector have a β very close to unity, though with exceptions like heavy kaons and protons and neutrons produced in minimum bias events. The detector is built to fit this fact. Likewise the trigger system is tuned to the SM. This fact can prove to be a challenge for a search like the one in question. The low-β property (see Section 4.2.3) however appart from introducing a challenge, also proves to be useful, as it can distinguish SMPs from the light SM particles. The light SM particles are at the LHC *ultrarelativistic*, having the following definition: the energy of an ultrarelativistic particle is almost completely given by its momentum ($pc \gg mc^2$), and thus can be approximated by E = pc. Take as an example top quark events; the LHC is said to be a *top factory* [36]. The top quark being also very heavy ($172.0 \pm 0.9 \pm 1.3 GeV$ according to ref. [35]) will have low β as well, but the lifetime, τ, of the top is very short, given by its decay width $\Gamma = 13.1 GeV$ [35]: $\tau = h/\Gamma = 6.6 \times 10^{-21} GeVs/13.1 GeV \approx 5 \times 10^{-25}$. This means that what we see in the detector are the daughters (or in fact some pursuing generations of the daughters) of the decaying top. These will in turn be ultrarelativistic, since there is such a large gap between the mass of the top and the detected decay products.

Penetrating power

Another feature shared due to the high mass is the penetrating power. In Figure 4.5 is shown the expected combined energy loss from ionisation and hadronic scattering for a 300 GeV $\tilde{g}$ and $\tilde{t}$ R-hadrons when traversing trough 1 m of iron; the mean value of β, of m=300 GeV $\tilde{g}$-based R-hadrons was found in Section 4.2.5 to be: $< \beta >$=0.5, giving a mean value of the kinetic energy of the light quark system of: $T = (\gamma - 1)m = 1.333 \times 0.6\ GeV = 0.8\ GeV$. At ATLAS where particles reaching the muon systems have traversed 1.7-3.5 m of iron [30] this yields an energy loss at the order of 10 GeV. With an average initial kinetic energy of order of 100 GeV a loss of this order will not stop the R-hadron, which is then expected to punch through.

Otherwise the detector signatures of R-hadrons can be characterised as being very versatile.

Irrespective of the SMP charge a $\tilde{g}$ R-hadron can be produced as a *neutral*,*charged* or *doubly* charged object and indeed in the generic model all of these variants are stable, while the

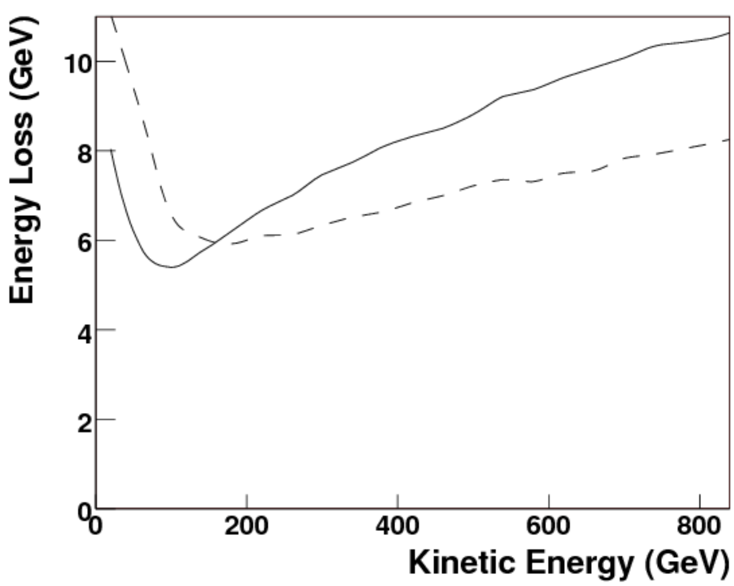

Figure 4.5: *Absolute energy loss in 1 m of iron for a m=300 GeV $\tilde{g}$ (fully drawn) and a m=300 GeV $\tilde{t}$ (dotted line). From Ref. [28].*

regge and intermediate models impose some restrictions. In the case of $\tilde{t}$ and $\tilde{b}$ the R-hadrons produced can be charged or neutral.

Charge flipping of R-hadrons

Since an R-hadron can change its light quark system due to hadronic interactions with the detector material, some rather peculiar/characteristic signatures are possible: charge flipping/fluctuation can cause single tracks to "appear from nothing" or be disrupted, or cause tracks to reverse the direction of bending. Also possible are back-to-back signals with the same charge or a a factor of two between the momentum measured in the Inner Detector and the Muon System due to the possiblity of an initially singly charged R-hadron changing to one of the doubly charged variants.

The most challenging scenarios are those where both the R-hadrons are neutral throughout the detector. Evenso, energy will always be deposited in the hadronic calorimeter if the trajectory is within the coverage.

Hence the Tile Calorimeter is a good starting point for searching for coloured SMPs.

Missing energy

In a SM context, only neutrinos can theoretically escape detection and therefore *missing energy* is seen as sign of either neutrinos escaping or new physics. The initial energy of the partons taking part in the primary collision cannot be determined. What can be measured is the momentum missing in the plane transverse to the beam axis, because one can, to a high accuracy, claim the beams to be travelling in one dimension. Hence the measurable missing energy is the *transverse momentum imbalance*, which is a good approximation in the relativistic limit with $E \approx p$. One distinguishes between *true* and *fake* missing transverse energy ($\not{E}_T$). A *true* $\not{E}_T$ should only arise in events with particles which solely interact weakly, propagating out, carrying momentum in the transverse directions. In practice what is measured is typically the transverse missing energy, calculated from calorimeter information only. Such a *measured* $\not{E}_T$ can arise in different ways: particles can out of the calorimeter coverage, there can be mismeasurement of energy, cracks or dead, distorted or noisy cells in the calorimeters. Sources of fake $\not{E}_T$ are continuously being "mapped" and are thus accounted for as thoroughly as possible. Here it is mostly the true $\not{E}_T$ which is of interest. For R-hadron events a large measured $\not{E}_T$ appears due to initial state radiation from one of the interacting partons from the proton-proton collision, causing transverse asymmetry in the event. It is expected that missing E_T appear in most R-hadron events, even with the SMP pair produced back-to-back.

4.4 Building the trigger

The basic idea of this study is to estimate the obtainable efficiency for selecting coloured SMP events by means of a dedicated L2 trigger. One must take into account that as LHC luminosity and energy increases harder prescaling will be necessary and thresholds will be raised.

The available ATLAS trigger system will here be used for building the trigger and keeping the experimental context in mind, there are constrains to be aware of. A trigger must meet the following demands simultaneously and with a high efficiency:

- select events of interest
- reject background

A momentum measurement along with β gives the mass according to the equation from special relativity:

$$p = m\beta\gamma \Leftrightarrow m = \frac{p\sqrt{1-\beta^2}}{\beta}, \tag{4.2}$$

where p is the 3-momentum and m is the invariant mass.

The background to SMP searches is in principle any SM process. The SM particles detected are *light*. Hence a mass variable can be used to discern between SM particles and SMPs.

Motivation for L2 strategy

As outlined in Section 3.3.6 the ATLAS trigger system is constructed in a way so that it is flexible; thresholds on Level 1 objects are programmable and the HLT algorithms can be combined in numerous different ways and be seeded by Level 1 objects of choice to optimize particular searches. Hence developers can with minimal changes to the actual code use the different pieces of code as building blocks for trigger chains optimized for different physics searches.

Recall the R-hadron detector event characteristic of being *slow* and *penetrating*; this suggests that an appropriate SMP trigger strategy, might be to make use of an algorithm searching for delayed signals in the muon chambers.

Already existing at ATLAS is a chain triggering on muon-tracks refitted with variable β; the cathode strip chambers of the Muon System have a very good timing resolution: 1.5 ns []. However one must expect signals to be lost due to event overlap with the next bunch crossing. This happens the following way: consider an event with a R-hadron. For the event to be assigned to the right bunch crossing a particle must deposit energy in either the calorimeters or the muon chambers before a particle of β=1 produced at the next bunch crossing can arrive at either detector system. For a bunch spacing of 25 ns this means that the difference in time-of-flight, ΔToF, must be less than 25 ns. To give a back-of-the-envelope estimate on the events lost due to this effect I calculate the minimum β a particle must have in order to not be assigned to the wrong event for bunch crossings of 25 ns, 50 ns and 75 ns respectively. In Table 4.3 the values are shown for both the muon chamber and Tile Calorimeter with the distance to muon system and Tile Calorimeter assumed to be 22 m and 6.5 m respectively; this corresponds to the farthest points in these detector systems. The table values represent worst case scenarios, where the pseudo-rapidity is maximal in order to be within coverage anyway.

In Figure 4.3 are shown the number of events that would be lost, due to having a β below the critical values, for three different $\tilde{g}$ masses. The numbers are estimated from the distributions

Bunch spacing	75 ns	50 ns	25 ns
TileCal	0.2	0.3	0.5
Muon chambers	0.5	0.6	0.7

Table 4.3: *The minimum β a particle must have, in order to not be assigned to the wrong bunch crossing in the tile calorimeter and muon chamber, at three different bunch spacings, the past (25 ns), present (50 ns) and future (75 ns) bunch spacing.*

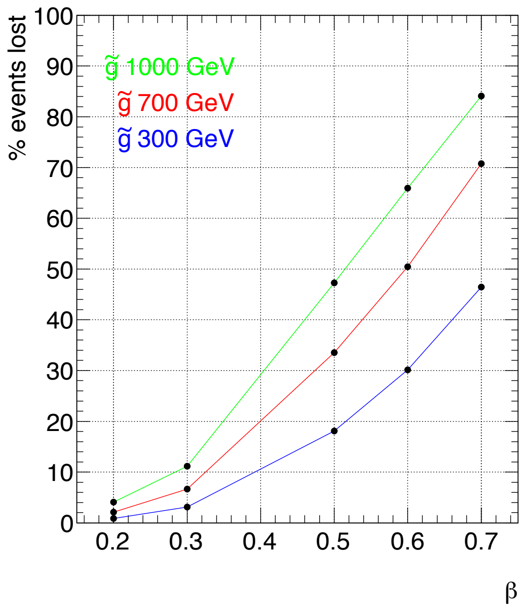

(a) no η-cut

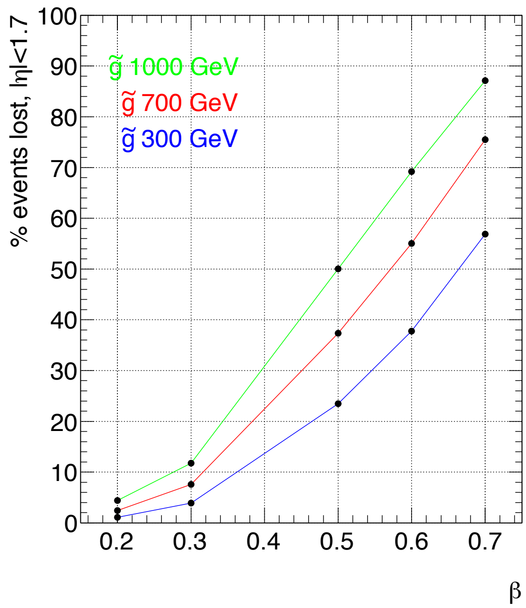

(b) with $|\eta| < 1.7$

Figure 4.6: *Average percentage of events that would be lost, due to having a below-critical β value, for three different $\tilde{g}$ mass points, with (a) no cut and (b) with $|\eta|$ less than 1.7. The numbers are based on "privately" produced simulations made with Pythia 6.*

in Figure 4.2 which were produced from simulations using Pythia 6 and without detector simulation, i.e representing how the events would look in vacuum. In Figure 4.6(b) cut on η has been applied: $|\eta| < 1.7$, as to be within the coverage of the Tile Calorimeter.

One sees from the figure that the loss may be severe for future bunch spacings, especially so for TeV masses: for $\tilde{g}$-based R-hadrons with m=1000 GeV 50% would have a β below 0.5, and would not reach the muon system before relativistic particles from the next bunch crossing, at a bunch spacing bs=50 ns. At bs=25 ns it would be almost 90 %. For the Tile Calorimeter it would be 12 % and 50 %; this shows that it would be practicable, if one could rely solely on this detector system.

The aforementioned lower mass limits set on R-hadrons, were based on a muon-system agnostic search, thus being sensitive to particles with a β down to as low as 0.3, as the bunch spacing was 50 ns during the recording of the data used in the search. Another advantage of this approach is, that in some models it is expected that R-hadrons will eventually convert to neutral variants when suffering hadronic interactions. Overall, meta-stable particles with lifetimes, $\tau \gg d/c$ with $d =$ the radius of the detector, will thus have a higher probabillity of being detected (directly) with the calorimeter system.

Here, results based on a muon-system agnostic approach will be presented in parallel with results where signals in the muon system are used in forming regions of interest.

Tile Calorimeter β-extraction

Like the Muon Spectrometer, the Tile Calorimeter also has excellent timing. Studies done with the internal laser calibration system, test beam data and cosmic rays, have shown that a timing resolution of less than 1.2 ns is achievable if the energy deposit in a tile cell is greater than 1.5 GeV [38]. It has also been shown that the timing resolution improves with the energy deposited, as seen in Figure 4.7. R-hadrons traversing the calorimeters are expected to deposit energy in all three calorimeter layers giving three independent measurements; in particle physics one is always dealing with statistical fluctuations, and independent measurements can help eliminate these.

In Figure 4.8 is shown the expected distribution of energy deposited by R-hadrons and $\tilde{\tau}$s in the Tile Calorimeter; the variable plotted is the average over the three cell layers, obtained from full simulation with Athena using the samples in Table 4.1. It is seen that the mean value in all cases lies above 1.5 GeV.

The timing resolution of the Tile Calorimeter enable the time-of-flight of a traversing particle to be measured. The time-of-flight, τ along with the distance, d, from the primary interaction point, gives an estimate of β: $\beta = d/\tau$.

High Level Trigger strategy

Considering the above, and recalling the need of a momentum measurement in order to get a mass estimate, it is concluded that an algorithm searching for late energy deposits in the Tile Calorimeter associated with ID tracks is an attractive starting point, for developing a Level 2 trigger for coloured SMPs.

In the HLT a package for searching for muons in the Tile Calorimeter is implemented; it

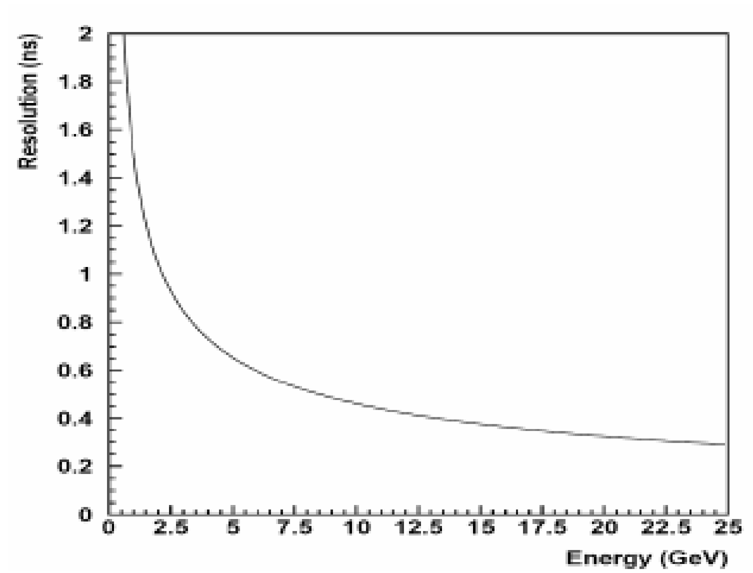

Figure 4.7: *The timing resolution as a function of energy deposit of Tile Calorimeter cell A-6 as extracted from test beam data from Ref.[38].*

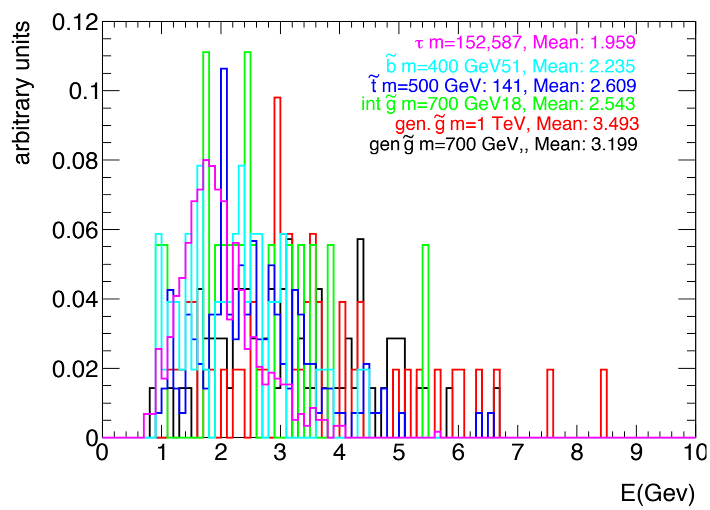

Figure 4.8: *Energy deposited in Tile calorimeter cells of R-hadrons and $\tilde{\tau}$ the variable plotted is the average over the three cell layers, obtained from full detector simulation with Athena.*

consists of Python scripts and C++ algorithms in a configuration optimized to search for low-p_T muons in the Tile Calorimeter. This package has here been modified for the purpose of developing a L2 SMP trigger. Below I describe how the algorithms select objects of interest.

At the HLT level of calorimeter read-out one can access, for each tile cell, the time a signal was recorded after a bunch crossing, i.e the time-of-flight of the particle giving rise to the signal, and the position of the cell. In a FEX, which I will refer to as the "tile FEX", a β estimator is constructed using the above and this information is attached to a TE (see Section 3.3.6) An Inner Detector tracking algorithm provides a momentum estimate of particles with charge. Combining the output TEs of these two FEXes a mass variable for candidates found is constructed in a third FEX.

In the section below I will go into more detail concerning the developed trigger chain, but here I want to point out that the tile FEX can be set to run over the L1 output of

- all cells, i.e over the full coverage, or
- only cells within L1 RoIs of a given type.

In both cases the tile FEX first performs a full scan of the Tile Calorimeter and saves the energy information for *all cells*. If running with no RoI ("full scan mode" hereafter), patterns are searched for in all cells; with RoI input, only the regions pointed to are scanned.

The full scan mode will in practice not be possible for running online; it would be too time consuming; however full scan mode running is highly valuable for testing the efficiency of different RoI seeds.

After selection the candidates are passed to the next algorithm and matched in (η, ϕ) to tracks found in the Inner Detector. The track-finding is done by an algorithm running in parallel with the tile FEX, doing a a scan of the ID and saving the momentum of tracks. Hence for R-hadrons that were charged in the ID the momentum can be obtained. As noted R-hadrons can be doubly charged which would cause an underestimation of the momentum by a factor 2, however it is only expected to be of danger for the muon system momentum measurement; following hadronisation it is predicted that only 0.05% of $\tilde{g}$ R-hadrons are doubly charged in models that allow it, hence in the ID there is low risk of this underestimate.

4.4.1 Level 2 trigger chain for SMPs

The main algorithms of interest are the tile FEX and a FEX combining an ID momentum measurement with the β from the tile FEX and a hypothesis algorithm.

In two algorithms new variables and routines have been added in order to use them in the purpose of developing dedicated R-hadron triggers.

Starting with the tile FEX, the algorithm is initiated with a numbering scheme for the read-out cells of the Tile Calorimeter being set up, in accordance with the structure shown in Figure 3.10, Section 3.3.4. Then a scan of the Tile Calorimeter read-out is processed in the following way. For each cell the energy deposition read-out, the position of the cell and the time of energy deposition is accessed, the β estimate is formed from the time t and the distance d from the IP, determined using $d = \sqrt{x^2 + y^2 + z^2}$. The β variable is saved along with *energy deposit* and *time of flight*, by filling a 3-D tensor structure $(64(\phi) \times 13(\eta) \times 3)$.

The algorithm then iterates over the energy deposit entries of the tensor selecting candidates defined as passing a lower threshold of 150 MeV in the outermost layer of the three layers. In full scan mode the iteration is over all $64 \times 13 = 845$ values and otherwise only over entries corresponding to the given L1 RoI η, ϕ pair.

Among the candidates fulfilling the above is searched for patterns consistent with a traversing muon or R-hadron, meaning that there should be energy deposits in all three layers (a "track") and that the deposit in at least two of these layers must pass an *upper* threshold, which ranges between $\sim$ 1 GeV and 2.5 GeV depending on the position of the cells. The deposits hence should be lying in a range between a *low* and a *high* threshold. These cuts are meant to reject electronic noise and minimum bias pile-up events (lower threshold) and eliminate hadronic showers and tails (upper threshold). Now the weighted average of β from the three independent measurements using the energy deposit as weighting factor is computed.

This information is then passed to the next algorithm where the matching to ID tracks is carried out. The ID algorithm runs in parallel with the tile FEX and searches for patterns of a traversing charged object: if a minimum of five space points are found, i.e five hits in either the Pixel Detector or semiconductor tracking detector, lying in a cone of ϕ, η with a halfwidth of 0.2 and 0.1 radians respectively, the information is passed on tagged as a track.

The geometrical matching of the ID tracks to the tile objects is as follows. The difference in η, ϕ must be less than 0.1 and 0.2 radians respectively. The variable ΔR is formed from $R = \sqrt{\eta^2 + \phi^2}$ and used to compare different tracks matching tile candidates. In case more than one matching track is found it is demanded that the ΔR be less than the ΔR of the previously found one.

At any step in the chain one can access the MC *truth* particle event record, i.e for an event that passed the last step we can access the η and ϕ of the two R-hadrons and hence signal candidates/RoIs can be matched geometrically to the MC particles. This geometrical matching is here called *truth matching* and is defined as requiring: $\Delta R < 0.1$ i.e the object is in the same η, ϕ cone as that of a MC truth-particle.

Now, for the matched tracks and Tile Calorimeter objects the mass variable is formed using equation (4.2), and attached to a TE to pass to a Hypo.

4.5 L1 trigger results

After running ATHENA on a sample of MC events the L1 items that were fired are accessible. This enables quantification of the L1 trigger response to R-hadron and slepton events. In Figures 4.9-4.14 are shown the efficiencies of different L1 items of selecting SMP events. For each model is shown the efficiency of the L1 items: "J", single jet; "JE", the transverse energy of all jets, "TAU" and "TAU(I)", leptons/hadrons from a decaying τ-lepton with or without isolation requirement; "XE", missing tranvserve energy; "TE" total transverse energy; "MU", single muon.

It can be seen that, at the lowest thresholds the L1 efficiency is (more than) $\sim$50 % for all types, with the exception of the "MU"-item, which is only around 30 % for the intermediate model $\tilde{g}$ and $\tilde{b}$ R-hadron events, but as much as 95 % for the $\tilde{\tau}$ events.

One however cannot see from these numbers what objects actually triggered the items; it

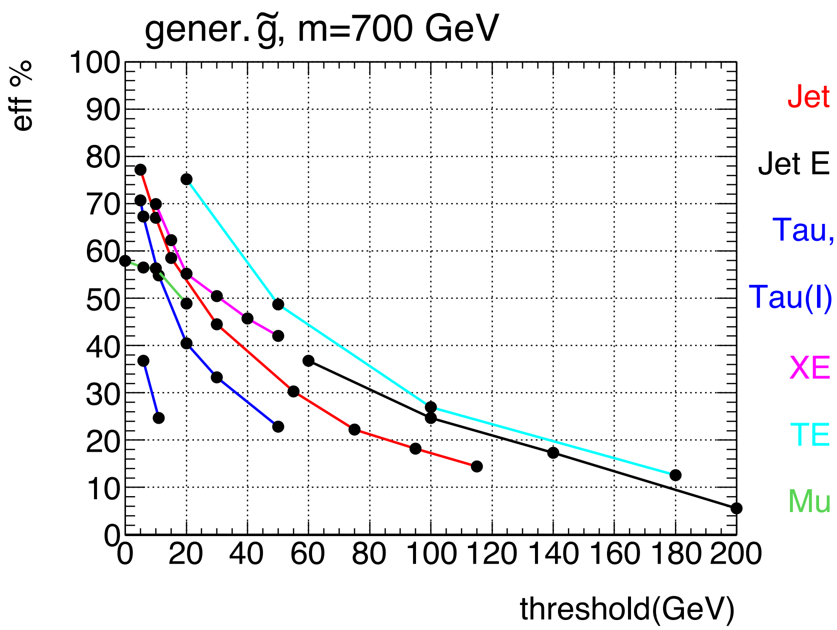

Figure 4.9: *L1 efficiency for generic interaction model, gluino 700 GeV*

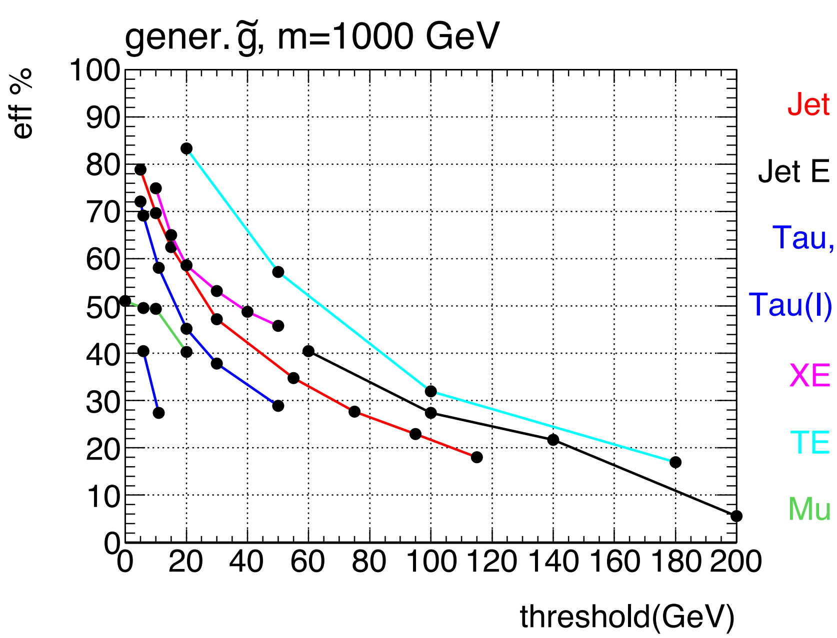

Figure 4.10: *L1 efficiency for generic interaction model, gluino 1000 GeV*

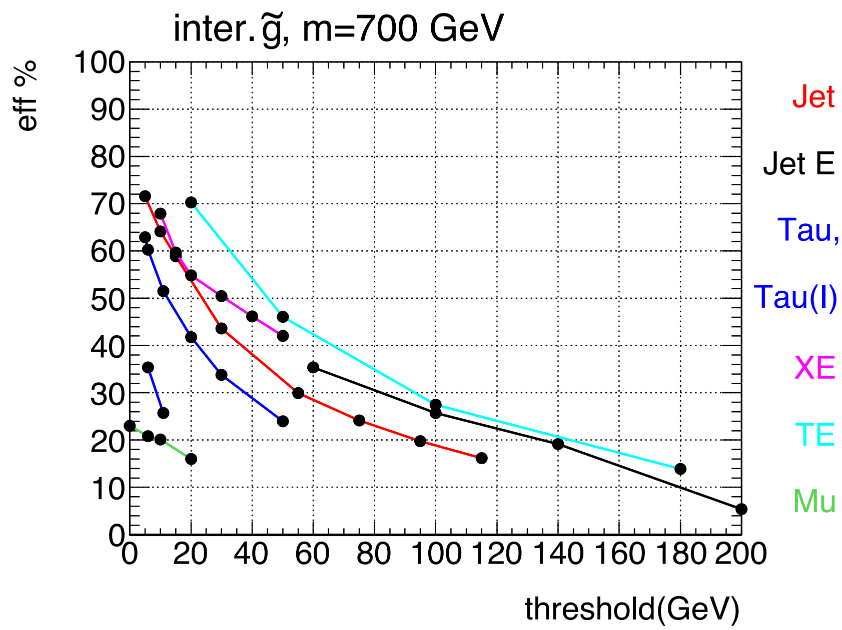

Figure 4.11: *L1 efficiency for intermdiate interaction model, gluino 700 GeV*

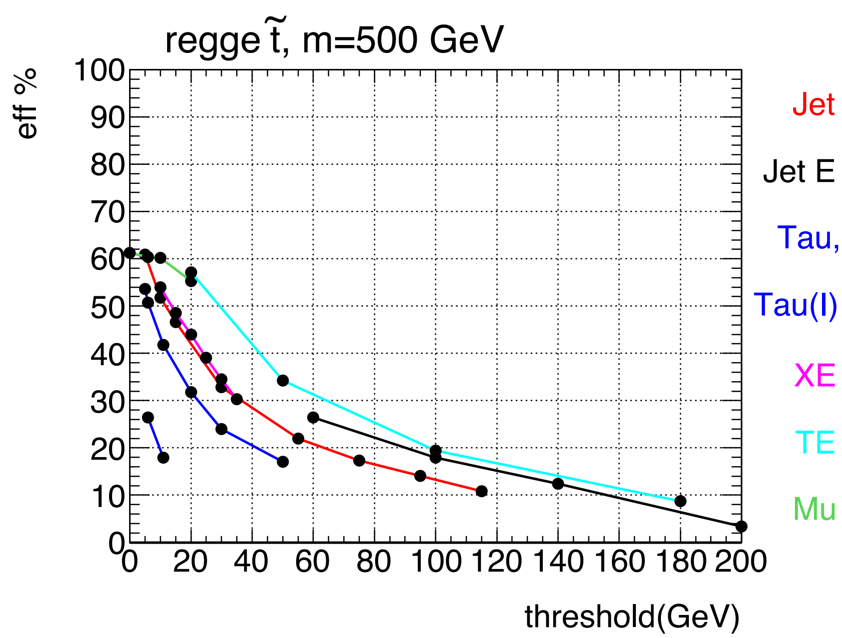

Figure 4.12: *L1 efficiency for regge interaction model, stop 500 GeV*

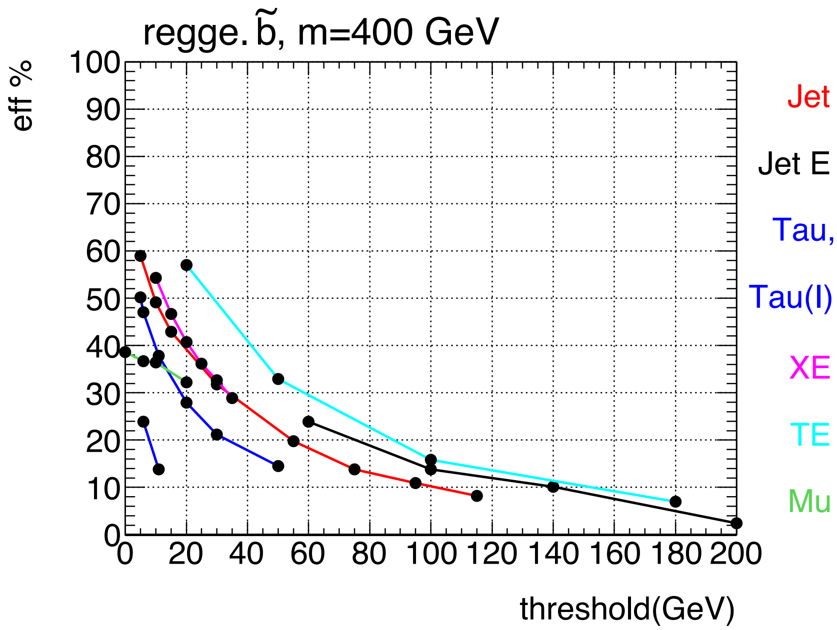

Figure 4.13: *L1 efficiency for regge interaction model, sbottom 400 GeV*

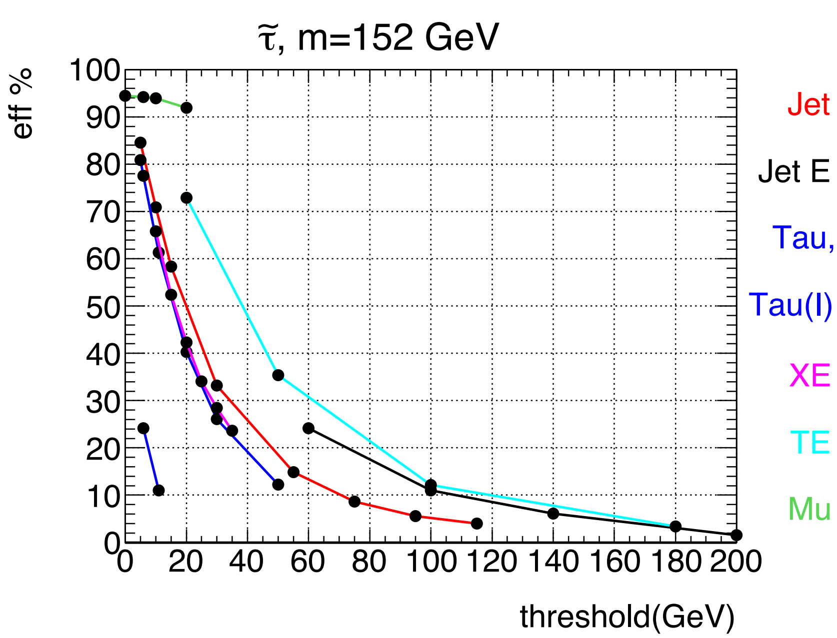

Figure 4.14: *L1 efficiency for $\tilde{\tau}$ m=152 GeV*

could be secondaries/the underlying event. This will only be resolved at the L2 where RoIs are matched to MC truth-particles to be seen in the next section.

One can conclude that the current L1 threshold configuration sets an upper bound on the overall efficiency obtainable of ∼50-60%.

Overall the L1 "XE", "TAU" and "MU" items are the most promising since they fall off the slowest with threshold.

4.6 High-level trigger results

In Figure 4.16 is shown the β distribution of candidates fulfilling Tile Calorimeter selection requirements in 4.16(a)-4.16(c) with given RoIs and for 4.16(d) with full a scan of the Tile Calorimeter, from running on events with $\tilde{g}$ R-hadrons of the generic interaction model type of mass 700 GeV and with no L1 trigger, that is L1 set to accept all events. Similar plots are in the Appendix for the remaining signal samples.
The distributions of truth-matched candidates are shown (marked red) on top of candidates. In 4.16(a)-4.16(c) the given RoIs are truth-matched. In 4.16(d), which was produced from running the tile FEX in full scan mode (thus given no RoIs) the truth-matching was made to candidates passing the selection of energy deposit threshold and having a track-like pattern, as described in Section 4.4.1. The truth-matched candidates are for all three RoI types distributed in a range from $\beta \approx 0.4$ to $\beta \approx 1$ (higher statistics would exhibit the shape shown in Figure 4.2(b)).
Referring to the true distribution shown in Figure 4.2(b) having a mean value of 0.583, it is seen that for truth-matched candidates passing this first selection, the mean value of Tile Calorimeter measured β has a bias towards higher β. Both for the different RoIs and full scan mode, $< \beta >$ ranges between 0.6 and 0.8. This bias is more pronounced for the calorimeter RoIs, for which the truth-matched mean value differs from the true mean by $\sim 30\%$ where in the case of muon RoI it is only $\sim 10\%$ and for the full scan there is hardly a bias as the difference in mean value is $\sim 3\%$.

The number of truth-matched entries compared to the number of unmatched candidates reveals that the muon-based RoI is significantly more efficient in selecting R-hadrons and sleptons than SM particles. Only in the case of the generic interaction model can jet RoIs be of reasonable use; for intermediate $\tilde{g}$ and the regge model squarks they are not feasible for selecting R-hadrons.

Referring to Figures 5.2-5.5 in the Appendix it can be seen that the remaining models exhibit similar patterns to the generic $\tilde{g}$, but with the difference that the overall efficiency is lower. For the generic $\tilde{g}$ of mass 1000 GeV the efficiency is also lower than for the 700 GeV mass point. This can be due to the lower average β resulting in some signals being too delayed to be processed by the CTP (irrespective of the bunch spacing).

In Figure 4.15 is shown the Tile Calorimeter-measured time-of-flight of R-hadrons and $\tilde{\tau}$ passing all selection requirements and it is seen that none of the surviving have a time-of-flight of more than 25 ns.

For the $t\bar{t}$ and Z-background plots shown in Figures 5.19-5.23 in the Appendix the β values are centered around unity as is expected, but also exhibit a tail pattern in low β. Selecting

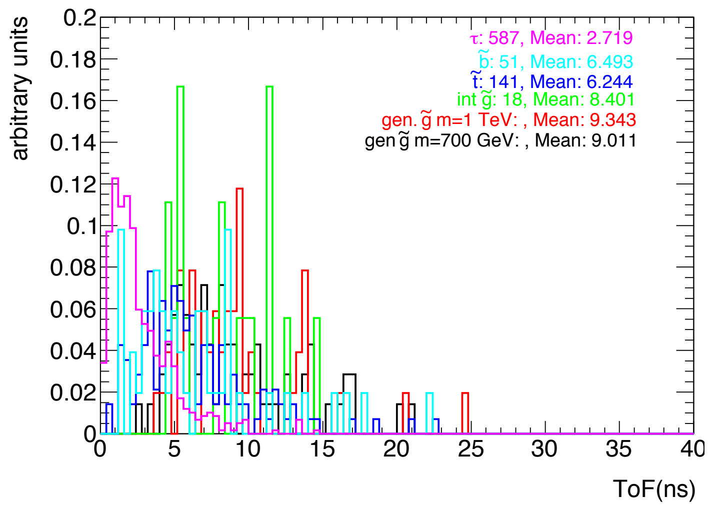

Figure 4.15: *Tile Calorimeter Time-of-flight of truth-matched candidates for the R-hadron models and $\tilde{\tau}$; the variable is a weighted average over the three tile cell layers. The plots are produced from running ATHENA full detector simulation.*

slow tile candidates would thus suppress most of this background but not get completely rid of it due to the tail.

From the plots in Figure 4.16 it can also be concluded that the calorimeter RoIs unpractically have higher efficiency for the SM particles in the remaining event and the background. In the case of non-decaying charged R-hadrons with moderate β the muon system based RoI are preferred. Referring to the appendix the same conclusions can be drawn for the other interaction models.

However the distribution resulting from running without RoI reveals that with an appropriate calorimeter RoI pattern the efficiency could be much improved.

Figure 4.17 shows the distribution of transverse momentum of candidates with a track matching the candidates passing the selection in the previous step (tile fex algo); as in the previous paragraph the sample shown is the generic $\tilde{g}$ of mass=700 GeV.
All truth-matched points lie above 100 GeV so setting a cut here will not reject signals. It is noted that again the muon-based RoI item gives the best efficiency, however the full scan mode (4.17(d)) is significantly more efficient, suggesting that a track-based RoI or a calorimeter RoI optimized for muons rather than jets might might be optimal for R-hadron triggering.

Referring again to the Appendix the same conclusions can again be drawn for the other interacton models. For the generic $\tilde{g}$ of mass=1000 GeV the p_T distribution is wider than in the low mass case, with a tail towards zero; this is expected since the pp collision energy is the same as was also noted in Section 4.2.3,

In Figure 4.19 is shown plots of the mass variable for RoIs with the generic interaction model.

Inspecting the plots in the figure, starting from the left, it is seen that the mass variable exhibits a pattern of a peak around zero and then another around the mass given to the Monte Carlo (MC) R-hadron.

Also plotted in the figure on top of the above described plot and marked red is the mass

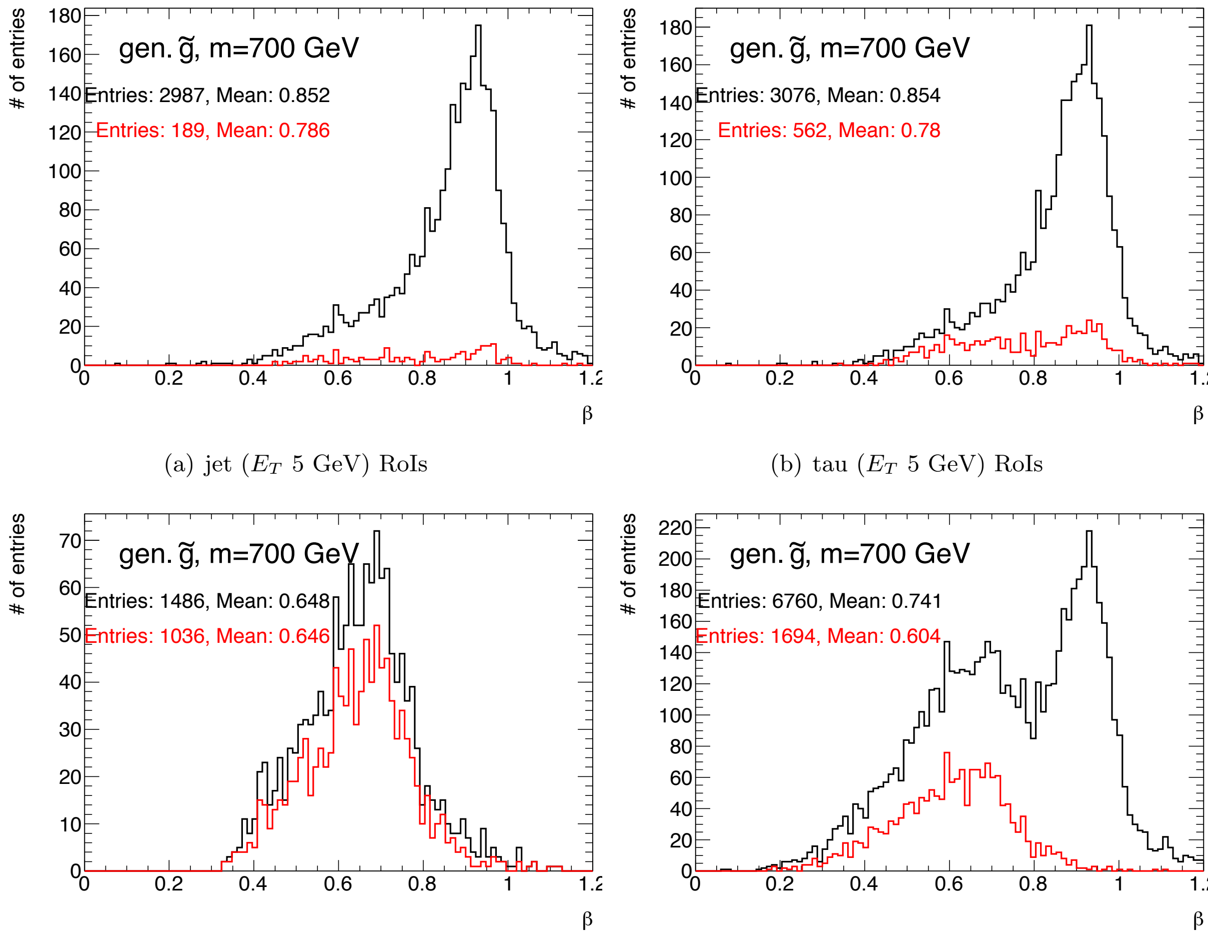

(a) jet (E_T 5 GeV) RoIs

(b) tau (E_T 5 GeV) RoIs

(c) muon (p_T 20 GeV) RoI

(d) No RoI

Figure 4.16: *β distribution of candidates found in the Tile Calorimeter scan of regions of interest based on 4.16(a) jet (E_T 5 GeV), 4.16(b) τ (E_T 5 GeV), 4.16(c) μ (p_T 20 GeV) and 4.16(d) with full scan of the Tile Calorimeter for $\tilde{g}$ of 700 GeV with the generic interaction model and with candidates from truth matched RoIs shown marked red.*

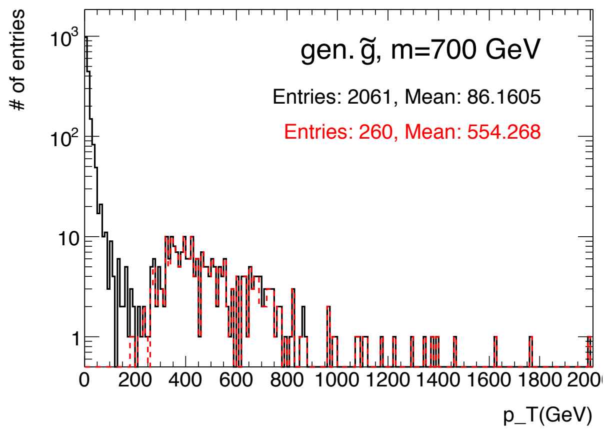

(a) jet (E_T 5 GeV) RoIs

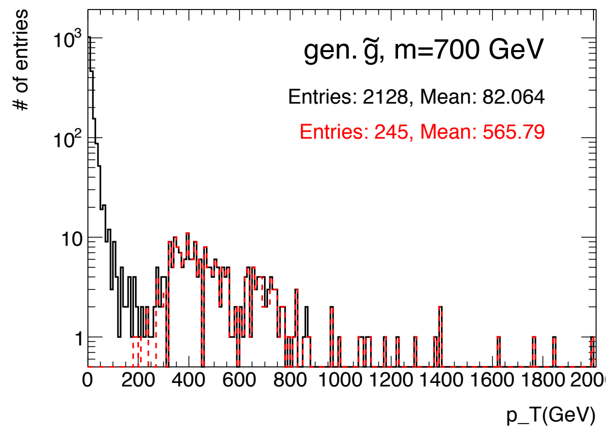

(b) tau (E_T 5 GeV) RoIs

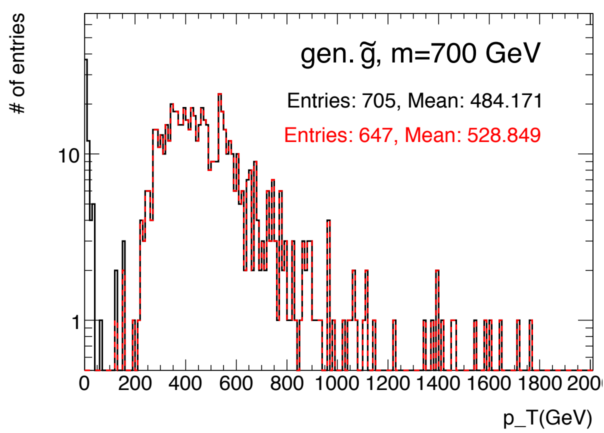

(c) muon (p_T 20 GeV) RoI

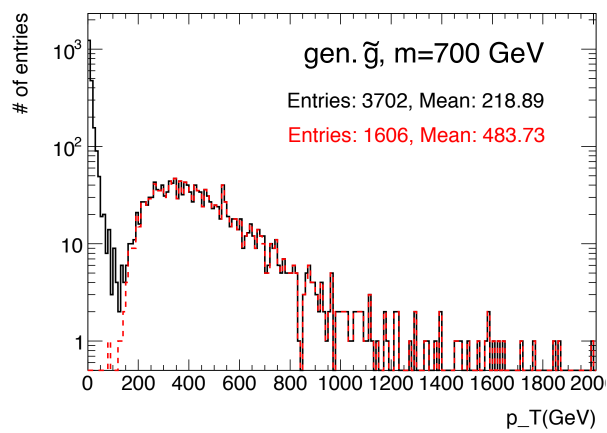

(d) unseeded

Figure 4.17: *p_T distribution of candidates found in the Tile Calorimeter scan of regions of interest based on 4.17(a) jet (E_T 5 GeV), 4.17(b) τ (E_T 5 GeV), 4.17(c) μ (p_T 20 GeV) and 4.17(d) unseeded for $\tilde{g}$ of 700 GeV with the generic interaction model and with candidates from truth matched RoIs shown marked red.*

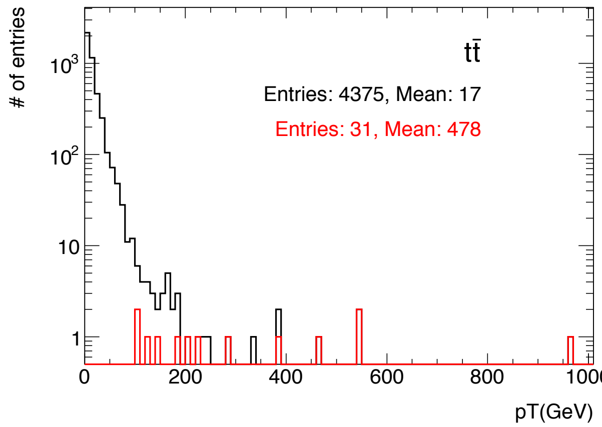

(a) jet (E_T 5 GeV) RoIs

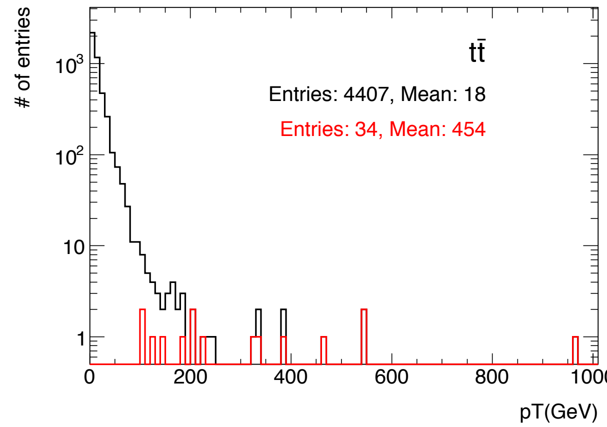

(b) tau (E_T 5 GeV) RoIs

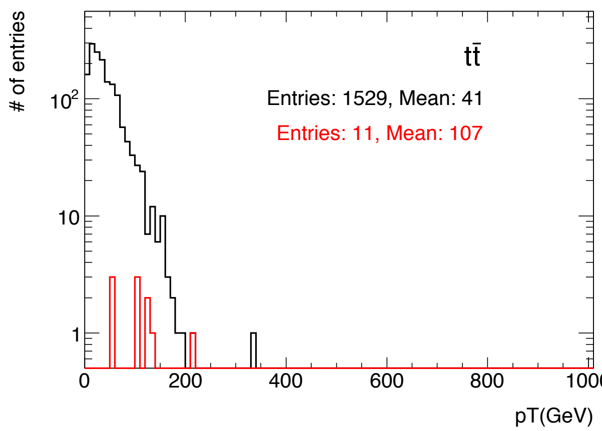

(c) muon (p_T 20 GeV) RoI

Figure 4.18: *Transverse momentum distribution of candidates passing selection in Tile Calorimeter and having a matching track in ID of $t\bar{t}$ events from Tile Calorimeter scans of RoIs based on (a) jet (E_T 5 GeV), (b) τ (E_T 5 GeV) and (c) μ (p_T 20 GeV).*

variable for truth matched objects and it is seen that the second peak is well matched to these.

The first peak is almost entirely due to SM particles from the event in all five cases and the truth-matched candidates all lie well above $\sim 100GeV$ with very few exceptions as is expected. Cutting on the mass is equivalent to cutting on p_T and β combined; one could also cut on β; but using this option might not reject slow muons/SM hadrons; likewise cutting on p_T would select high energy muons produced copiusly from for instance $t\bar{t}$ events, as seen from the p_T of $t\bar{t}$ shown below in Figure 4.18.

4.6.1 RoI results

In Table 4.4 is shown the L2 chain efficiency of selecting R-hadron events for three different RoIs and full scan for the different models and with no L1 demand (all events accepted at

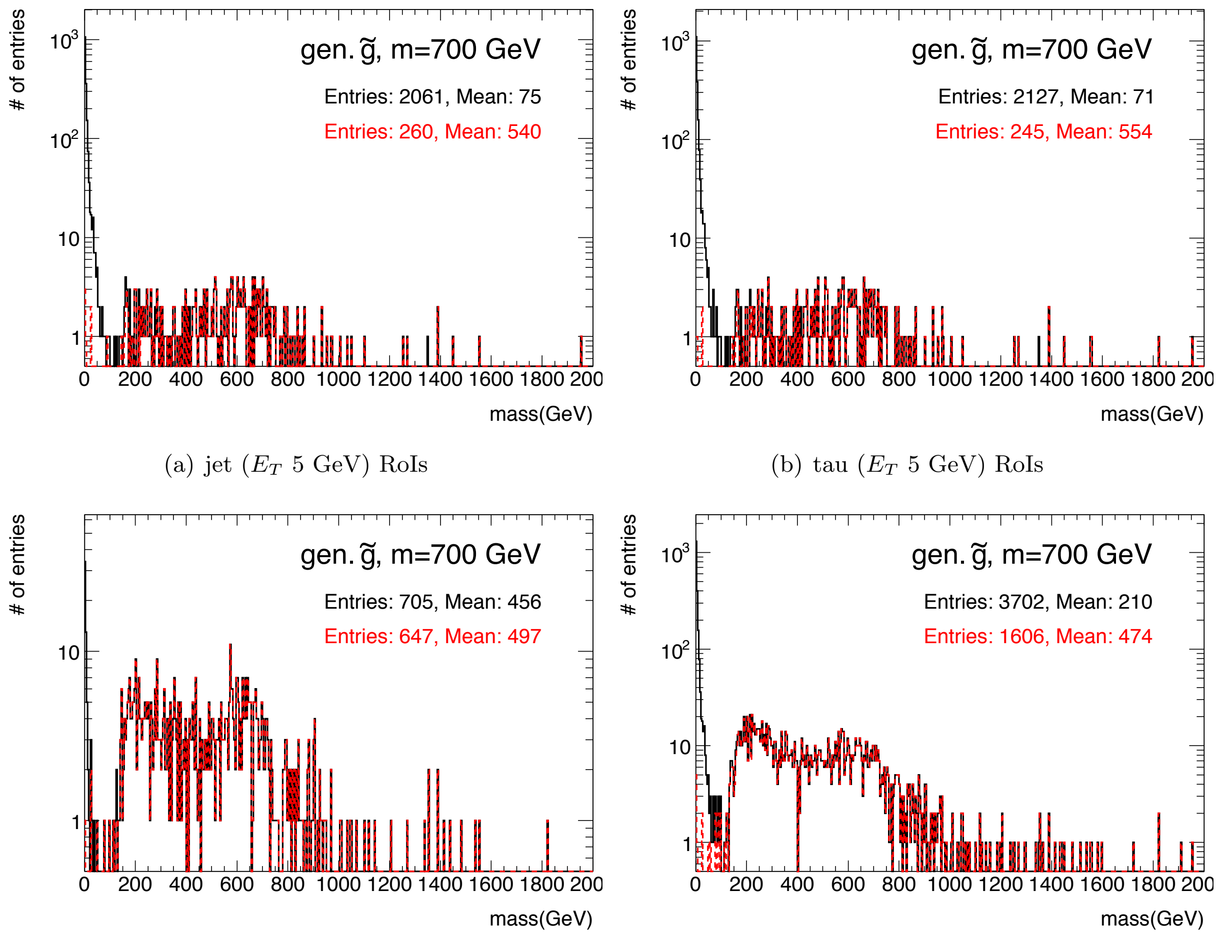

(a) jet (E_T 5 GeV) RoIs

(b) tau (E_T 5 GeV) RoIs

(c) muon (p_T 20 GeV) RoI

(d) No RoI

Figure 4.19: *Mass distribution of candidates found in the Tile Calorimeter scan of regions of interest based on 5.13(a) jet (E_T 5 GeV), 5.13(b) τ (E_T 5 GeV), 5.13(c) μ (p_T 20 GeV) and 5.13(d) 2 GeV deposit in the EM calorimeter for $\tilde{g}$ of 700 GeV with the generic interaction model and with candidates from truth matched RoIs shown marked red.*

RoI	g. $\tilde{g}_{m=700GeV}$	g. $\tilde{g}_{m=1000GeV}$	i. $\tilde{g}_{m=700GeV}$	$\tilde{t}_{m=500GeV}$	$\tilde{b}_{m=400GeV}$	$\tilde{\tau}_{m=152GeV}$
J5	2.60 %	1.88 %	0.68 %	0.97 %	0.44 %	16.0 %
TAU5	2.45 %	1.84 %	0.64 %	0.78 %	0.37 %	14.9 %
MU20	6.47 %	5.72 %	1.78 %	14.9 %	5.20 %	62.0 %
No RoI	16.1 %	14.3 %	8.80 %	26.9 %	11.9 %	78.0 %

Table 4.4: *Signal efficiency of L2 chain with no L1 trigger (all events accepted at L1). Obtained from running detector simulation over the signal samples listed in Table 4.1 .*

RoI	g. $\tilde{g}_{m=700GeV}$	g. $\tilde{g}_{m=1000GeV}$	i. $\tilde{g}_{m=700GeV}$	$\tilde{t}_{m=500GeV}$	$\tilde{b}_{m=400GeV}$	$\tilde{\tau}_{m=152GeV}$
J5	6.2	7.6	12.9	27.8	27.0	4.9
TAU5	6.6	7.8	13.6	34.4	32.2	5.2
MU20	2.5	2.5	4.9	1.8	2.3	1.2

Table 4.5: *Relative L2 chain signal event efficiency of full scan mode over RoI seeded mode.*

L1). The selection requirements are the passing of track-likeness the energy deposits being within range in the Tile Calorimeter and ID track matching of candidates and with a cut on the obtained mass variable of 100 GeV.

The RoIs tested shown are "J5", L1 *jet* item, and "HA5", L1 τ item, both with a E_T threshold of 5 GeV and "MU20", μ with p_T threshold of 20 GeV and with no L1 trigger.

The efficiency of the full scan mode gives the maximum efficiency obtainable with the specific strategy used, i.e when demanding simultaneously specific energy patterns in the Tile Calorimeter and ID tracks that matches the tile candidates.

Running in full scan mode is for all models more than twice as efficient as any of the RoIs and $\sim$ 5 times more efficient for the $\tilde{t}$.

Comparing for the two mass point of $\tilde{g}$ both with generic interaction model, it can be seen, that the efficiency for all RoI types as well as for the full scan mode, is lowered ~1-2 % at the higher mass compared to the lower. Since the hadronisation and interaction are identical the effect is due to kinematics. The p_T distribution is wider for m=1000 GeV than m=700 GeV as can be seen in Figure 4.3 in Section 4.2.3, and the mean value of β is lower, one of these effects cause the lowering of efficiency.

4.7 Ratebudget

As described in Section 3.3.8 L2 chain are, when running *online*, seeded by L1 items, only for *offline* testing on MC samples, is it possible to accept all events at L1. Based on the L1 results and HLT results combined, L2 chains have been built with the L1 triggers "L1 XE20", "L1 TAU5" and "L1 MU20"; performance plot for the three chains are shown in the Appendix in Figures 5.57-5.60. These are compared to selected reference triggers, for different thresholds passed by the L1 items. This is shown in Figures 4.20-4.21 plotting the fractions of different background efficiencies, ε_{BG} of the SMP trigger chain over the background efficiency

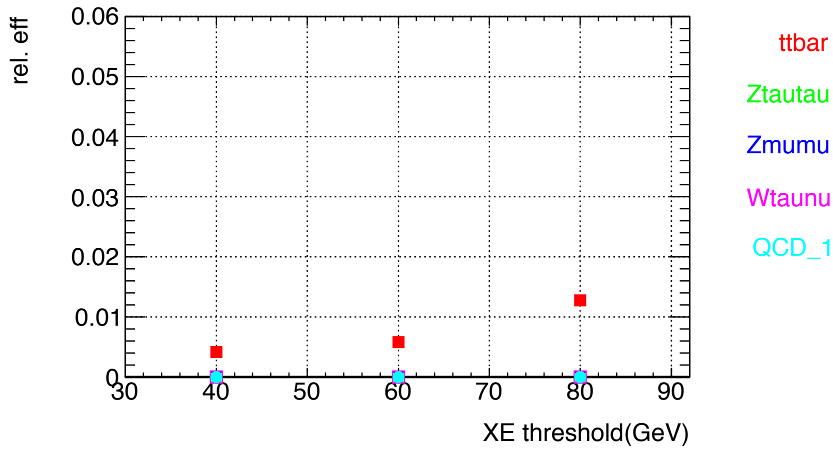

Figure 4.20: *Relative background efficiencies as a function of threshold, of XE EF ($\not\!\!E_T$ event filter) triggers to the developed L2 SMP trigger chain with L1 XE 20 GeV.*

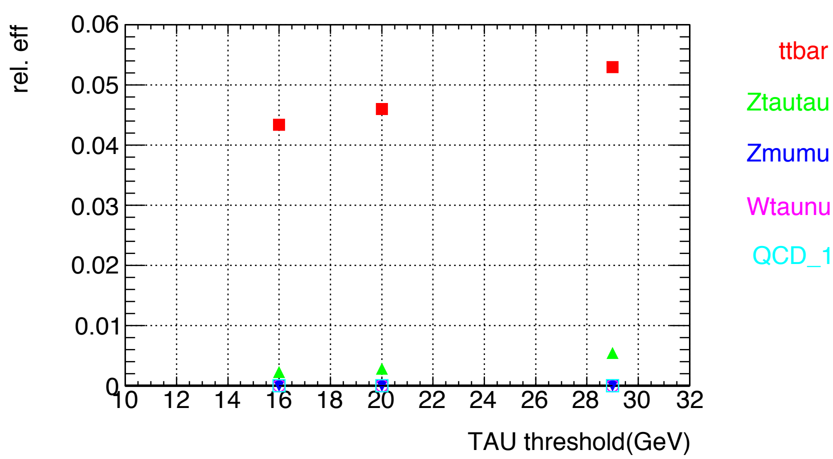

Figure 4.21: *Relative background efficiencies as a function of threshold, of TAU reference EF triggers to the developed L2 SMP trigger with L1 TAU 20 GeV.*

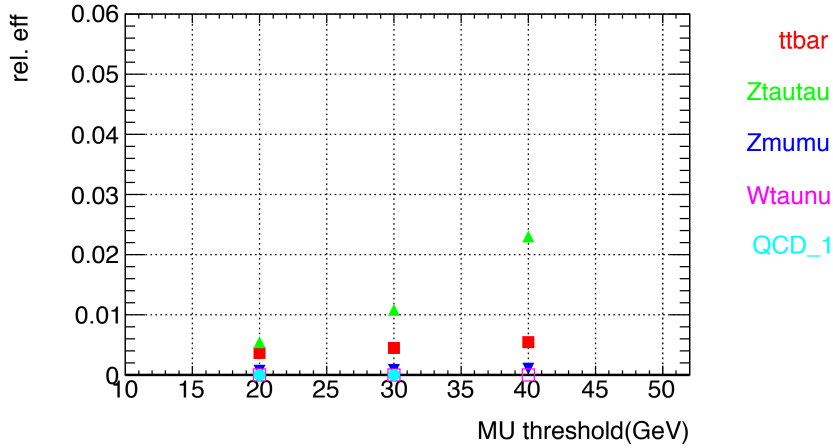

Figure 4.22: *Relative background efficiencies as a function of threshold, of MU reference EF triggers to the L2 SMP trigger with L1 MU 20 GeV.*

Run	Links	#LB	Start and endtime (CEST)	#Events
177540 Period: A,A1,AllYear	DS, RS, BS, AMI, DQ, ELOG, DCS:SoR/EoR, OKS	396 (58 s)	Mon Mar 14 2011 09:28:47 – 15:55:29	2,646,393 (114.1 Hz)

Figure 4.23: *Run 177540 specification summary.*

of reference trigger chains for different thresholds:

$$\varepsilon_{BG,relative} = \frac{\varepsilon_{BG}(SMP\ chain)}{\varepsilon_{BG}(ref.chain)}$$

The reference triggers are the chains: "EFMetHypo_xe40_noMu", "EFMetHypo_xe60_noMu" and "EFMetHypo_xe80_noMu" selecting events with a missing energy based on the calorimeters only (no muon system correction), "EF_tau12_loose", "EF_tau16_loose", "EF_tau20_loose" and "EF_tau29_loose", selecting events candidating for being τ events with loose requirements, i.e the less strict isolation option, "EF_mu20_MSonly", "EF_mu30_MSonly", "EF_mu40_MSonly", muon selecting event filters using solely the Muon System.

Figure 4.20 shows that only $t\bar{t}$ events are expected to add to the filling of disk space if using the "L1 XE20" trigger for seeding the SMP chain; Figure 4.21 show that seeding with a "TAU" L1 trigger is expected to be slightly more dangerous as both $t\bar{t}$ events and $Z \to \tau\tau$ have relative efficiencies to τ triggers being separated from zero and Figure 4.22 show a similar result when comparing "L1 MU20"-seeded SMP trigger to *muon* event filters.

In Figures 4.25-4.28 are shown the rate plots before prescale of selected L1 items, at run number 177540 which has the specifications shown in Figure 4.23.

In Figures 5.34-5.38 in the Appendix are shown rates and prescales of more L1 items for the same run.

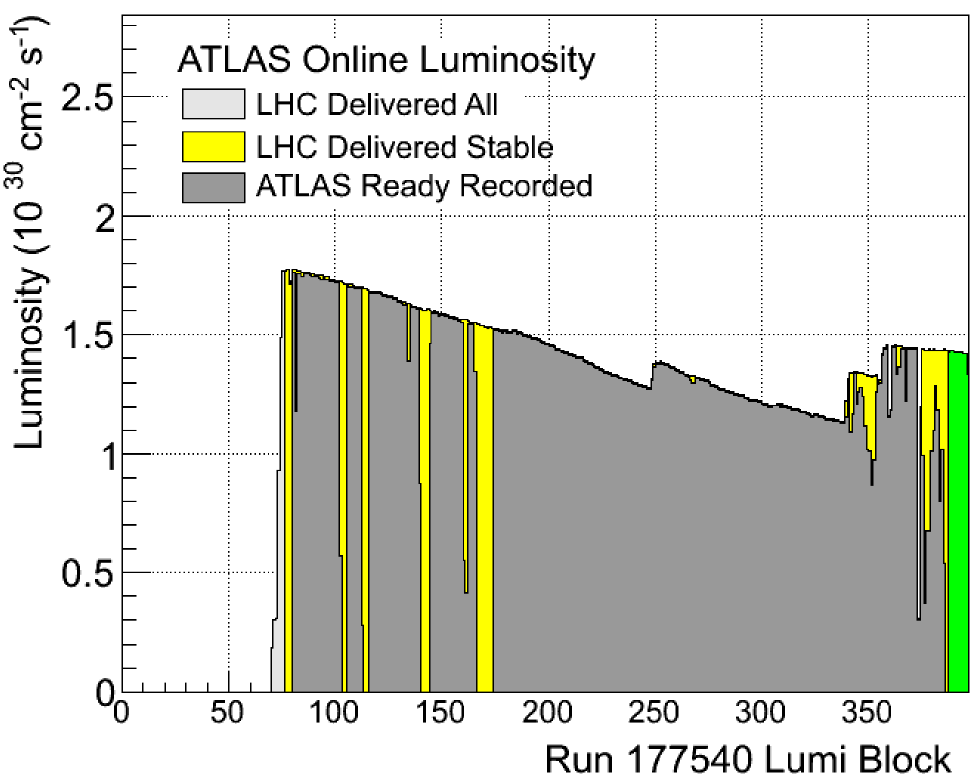

Figure 4.24: *Run 177540 luminosity, peaking at* 10^{30}.

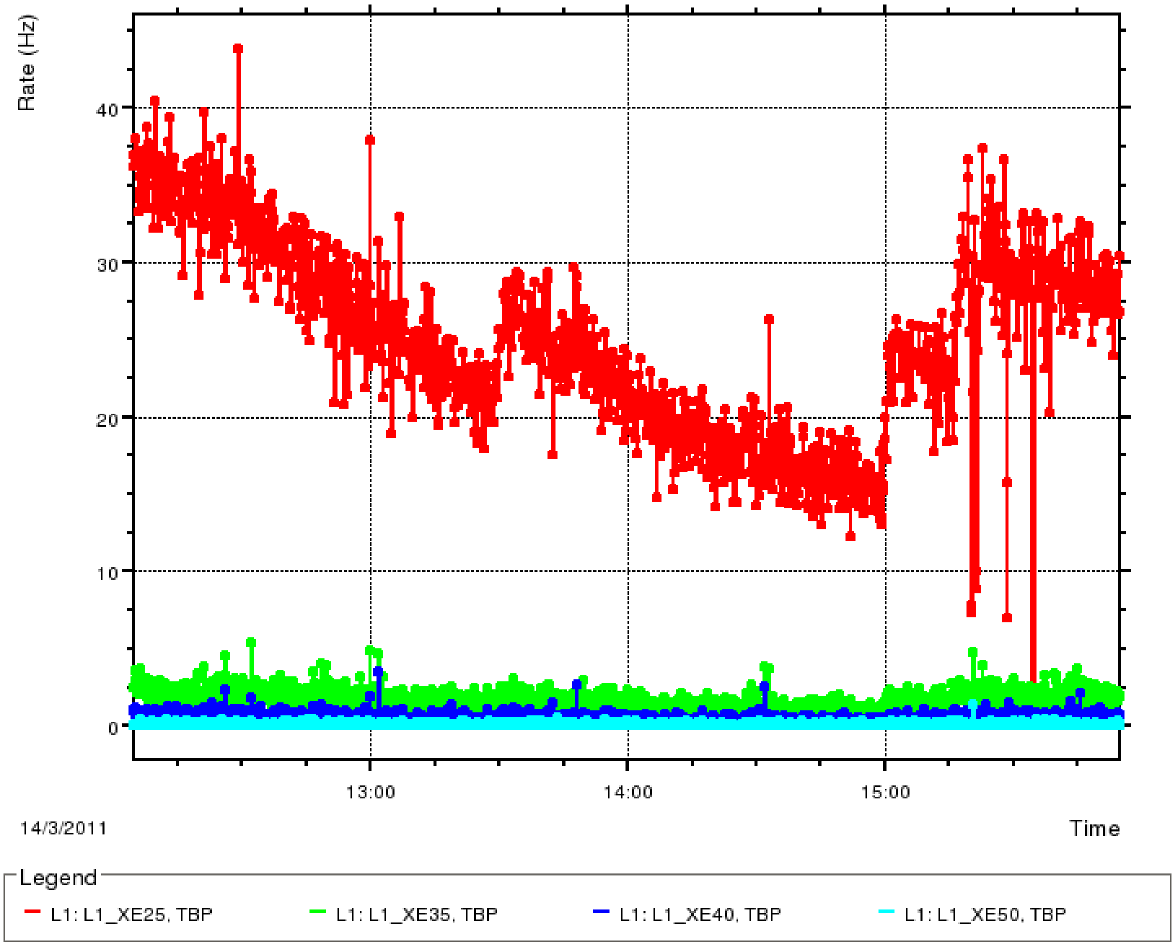

Figure 4.25: *Rates in Hz of L1 XE trigger items for run 177540. TBP stands for triggered before prescales.*

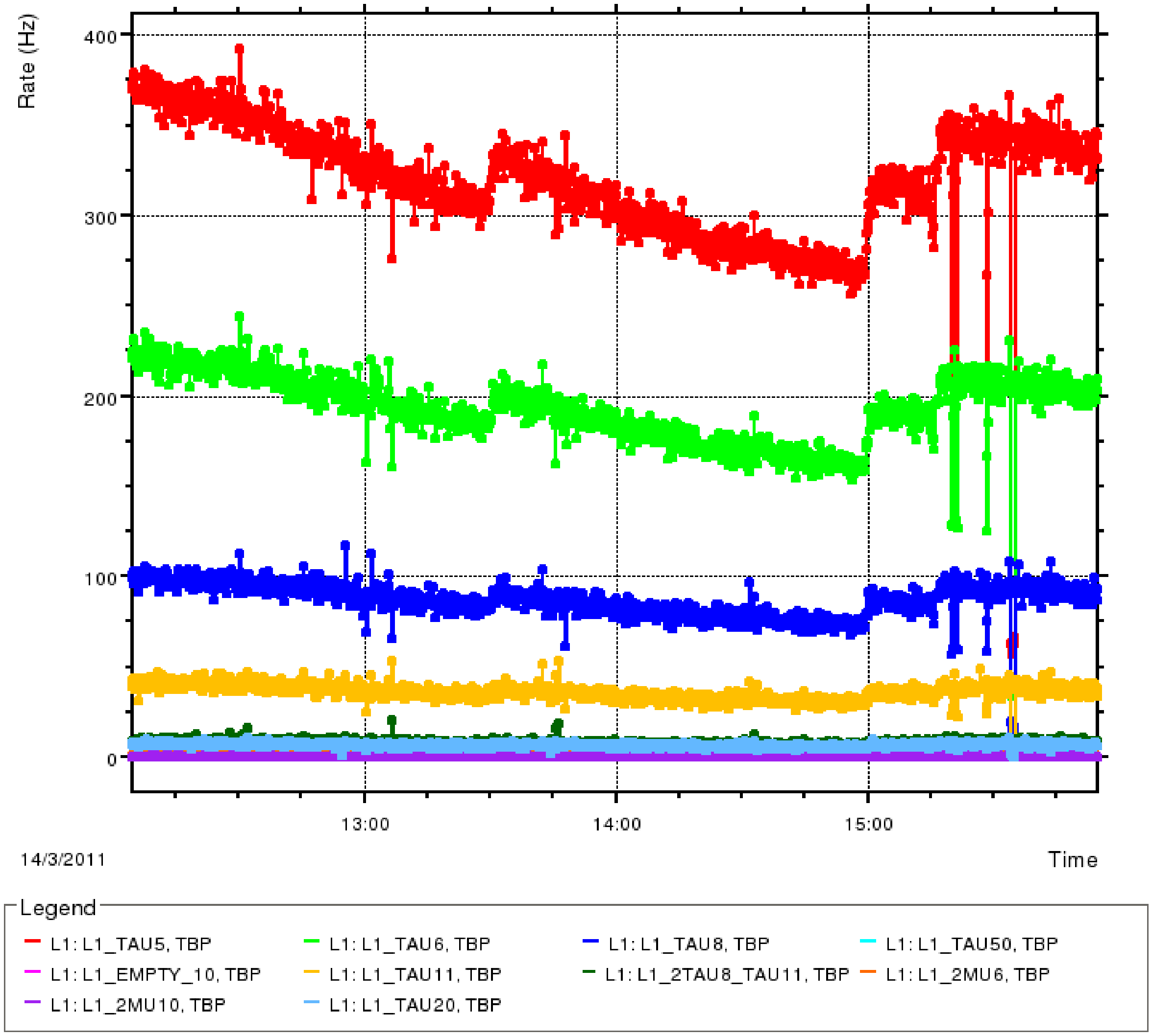

Figure 4.26: *Rates in Hz of L1 TAU trigger items for run 177540.TBP stands for triggered before prescales.*

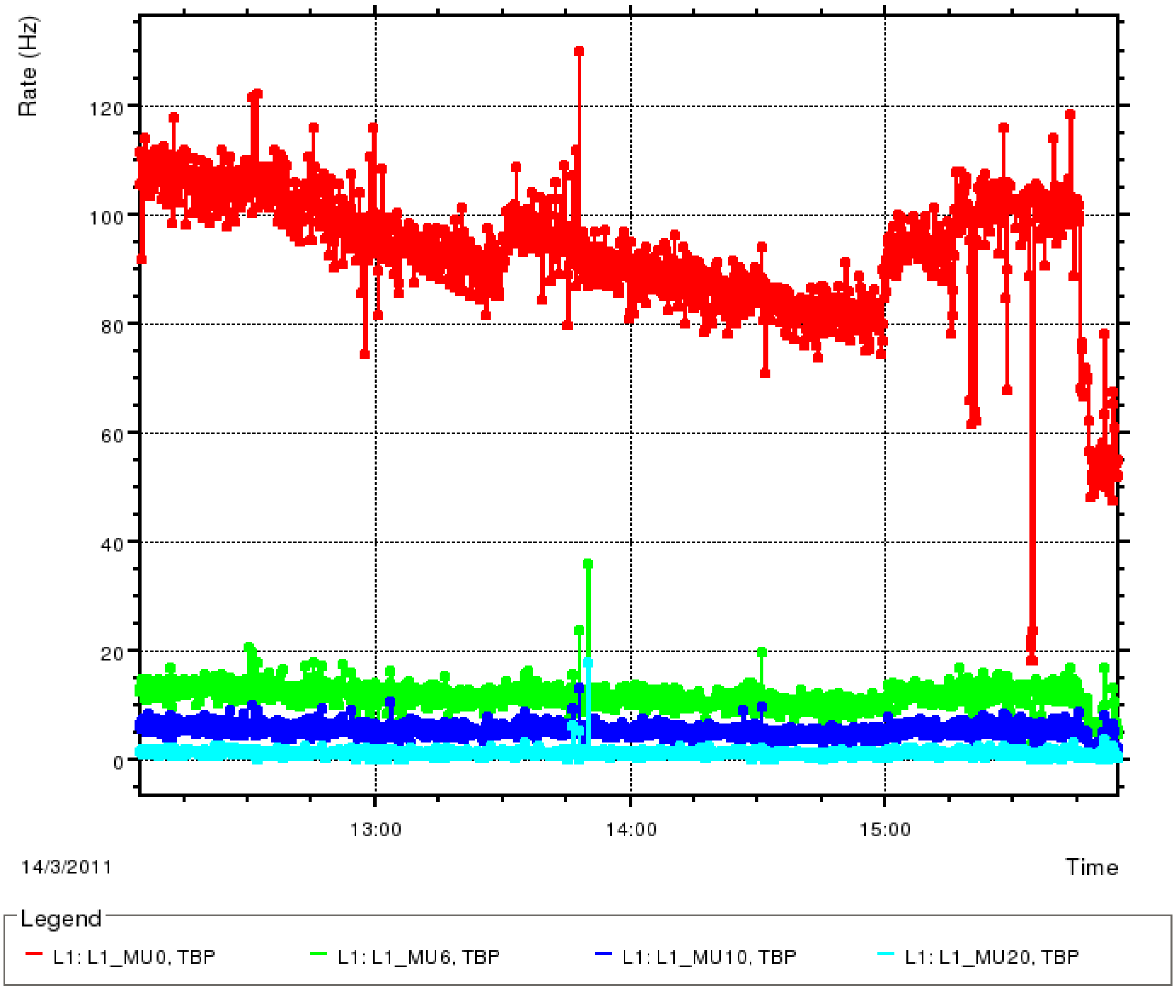

Figure 4.27: *Rates in Hz of L1 MU trigger items for run 177540. TBP stands for triggered before prescales.*

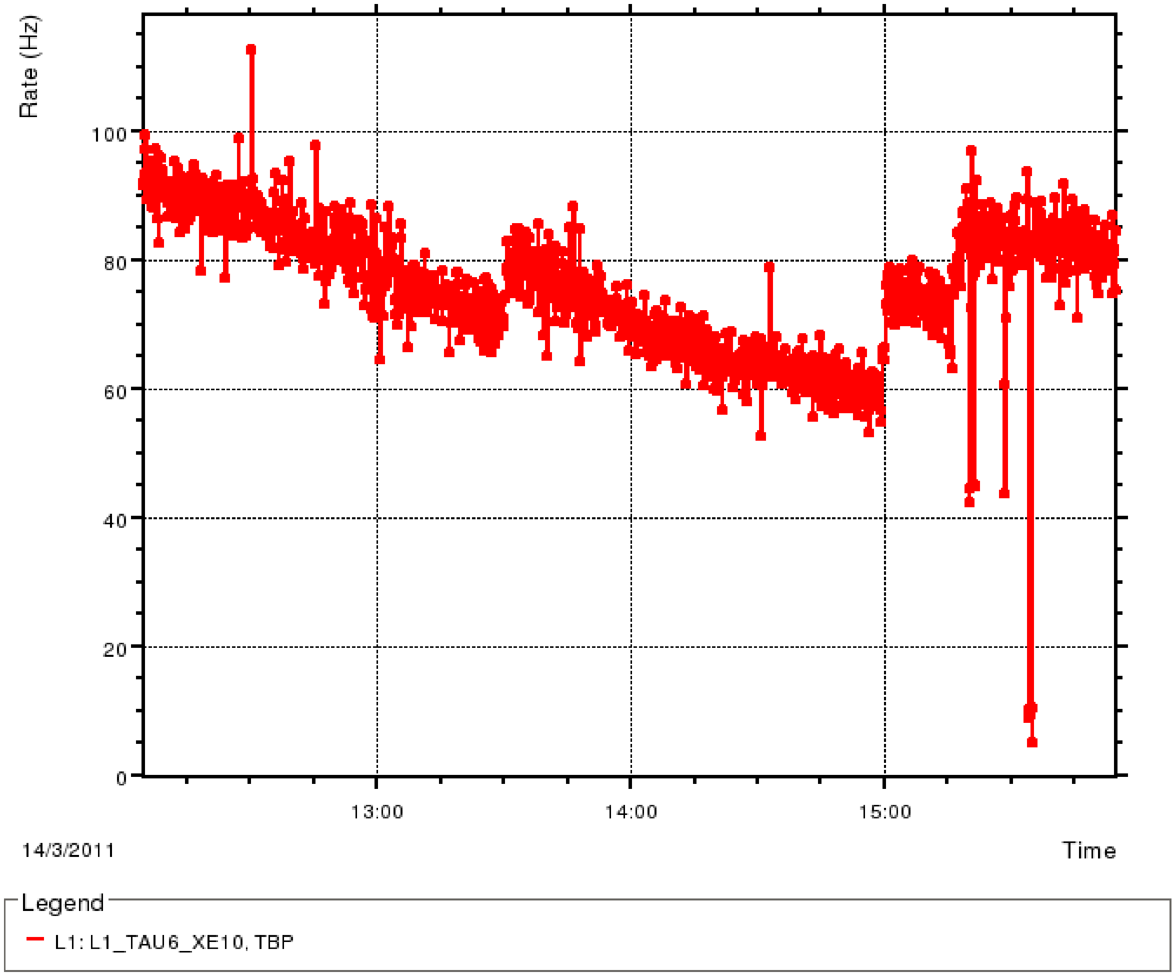

Figure 4.28: *Rates in Hz of combined L1 TAU6 XE10 items for run 177540. TBP stands for triggered before prescales.*

The L1 “TAU” triggers have a fairly high rate all over, for the three lowest thresholds it is at the order of 100 and above. Recall that the total rate of L1 should be ∼75 kHz. With the number of L1 items being at the order of 100, the rate of each item should be around or below 100 Hz; this is coarsely speaking and not taking into account that some item type are considered more interesting than others. This means that L1 TAU items of low threshold are likely to be prescaled and indeed it can be seen in Figure 5.38 in the Appendix that all lower threshold items were prescaled or vetoed in this run. Figure 4.24 shows the luminosity over the run, with a peak luminosity of 10^{30}. Current/Planned luminosities are 3 orders of magnitude higher, so that the rates are expected to increase substantially.

The rate plots in Figure 4.27 reveal that “MU20” should not be causing any kind of overload if set to pass, as it stays below 10 Hz during nearly the full run.

L1 “XE” rates are shown in Figure 4.25 and being promising as for all four thresholds shown it stays below 50 Hz for threshold=25 GeV and for 35 GeV, 40 GeV and 50 GeV even below 5 Hz.

4.8 Conclusion

A L2 trigger for SMPs has been developed The background processes without muons are nearly eliminated when using "MU" RoIs for seeding the chain algorithm. $t\bar{t}$ and $Z \rightarrow \tau\tau$ events are not fully eliminated though surpressed by cutting on the mass variable obtained from the combined Tile Calorimeter and ID FEX'es, however the rejection is reasonable. For SMPs not giving signal in the muon chambers the missing energy and tau L1 items can be used.

When LHC intensifies, and hence prescales + thresholds on L1 triggers are raised, the obtainable trigger efficiencies are limited to the ones shown in Figure 4.29 with the uncertainty regarding $\tilde{g}$ R-hadrons interactions with matter held.

Improvements are obtainable if a R-hadron specific L1 calo-item would be implemented, giving efficiences ranging from 9 % for the "intermediate" interaction model to 78 % for a slepton of mass m=150 GeV. A thorough study of such an item would be needed.

Rumors will know that a L1 "ID track trigger" is being designed, but there are grave challenges concerning the timing of such an algorithm, it might otherwise prove to be gratifying for the SMP search.

The L2 trigger developed is indeed promising for $\tilde{\tau}$-pairs with efficiencies of up to $\sim 30\%$. For $\tilde{t}$-pairs an efficiency of $\sim 15\%$ is attainable.

Outlook

For $\tilde{g}$ R-hadrons the probability of forming a $g - \tilde{g}$ bound state (gluino-ball) it theoretically uknown; in the samples used the probability was set to 10 %. Testing the efficiency for other gluino-ball probabilities should be done.

Running the trigger chain on a larger sample of background events, preferably so-called data-driven backgrounds is due.

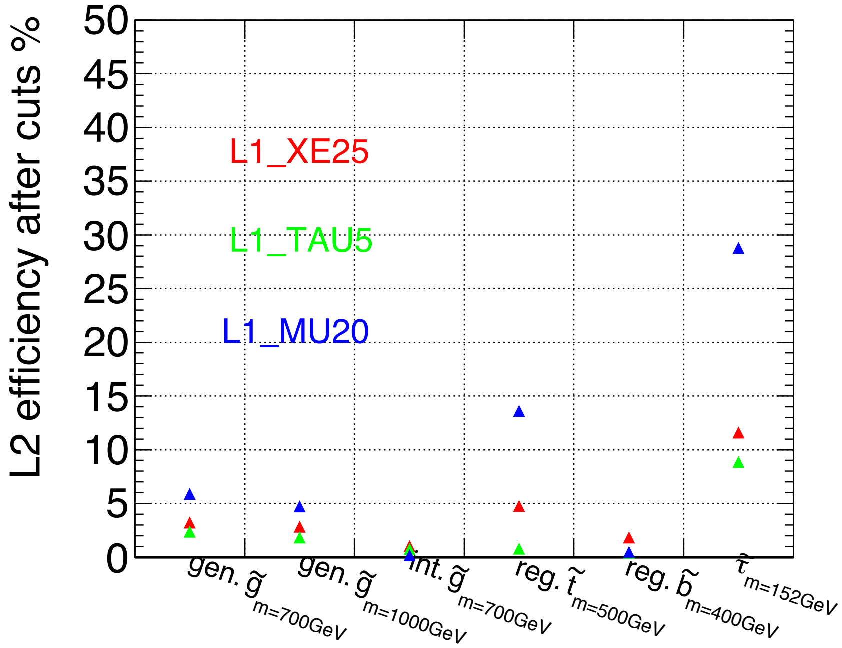

Figure 4.29: *L2 efficiency of three L1 seeds after setting a cut on the mass variable of 100 GeV.*

Chapter 5

Appendix

5.0.1 Signal plots

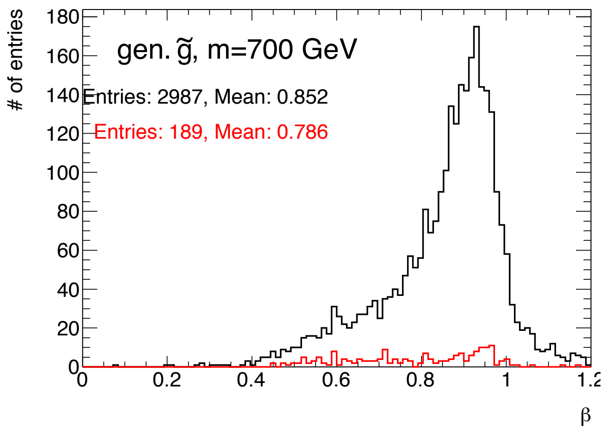

(a) jet (E_T 5 GeV) RoIs

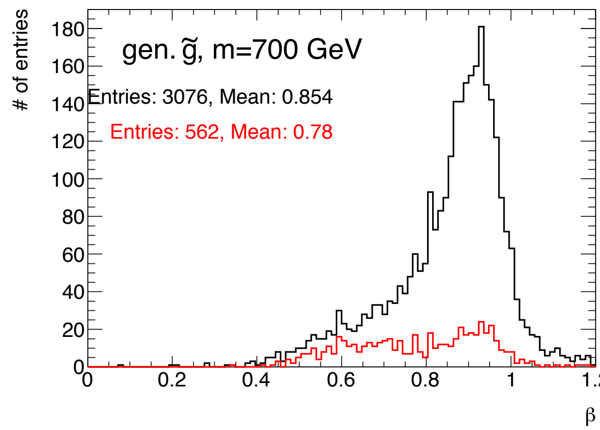

(b) tau (E_T 5 GeV) RoIs

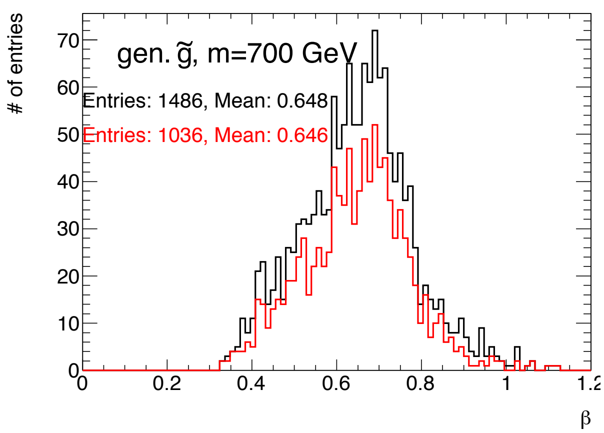

(c) muon (p_T 20 GeV) RoI

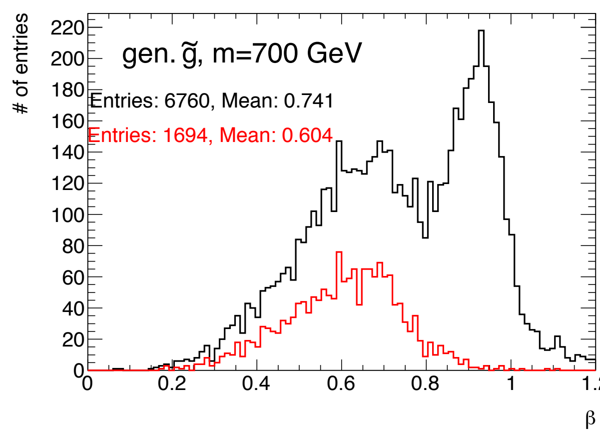

(d) No RoI

Figure 5.1: *β distribution of candidates found in the Tile Calorimeter scan of regions of interest based on 5.1(a) jet (E_T 5 GeV), 5.1(b) τ (E_T 5 GeV), 5.1(c) μ (p_T 20 GeV) and 5.1(d) a full scan for $\tilde{g}$ of 700 GeV with the generic interaction model and with candidates from truth matched RoIs shown marked red.*

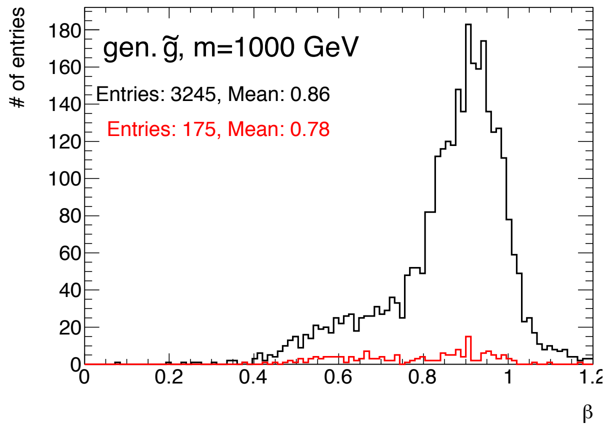

(a) jet (E_T 5 GeV) RoIs

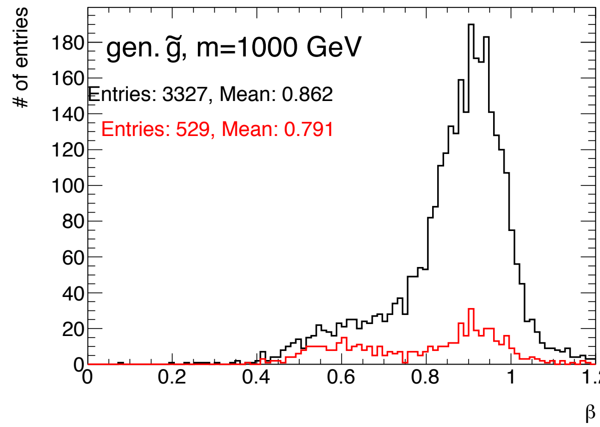

(b) tau (E_T 5 GeV) RoIs

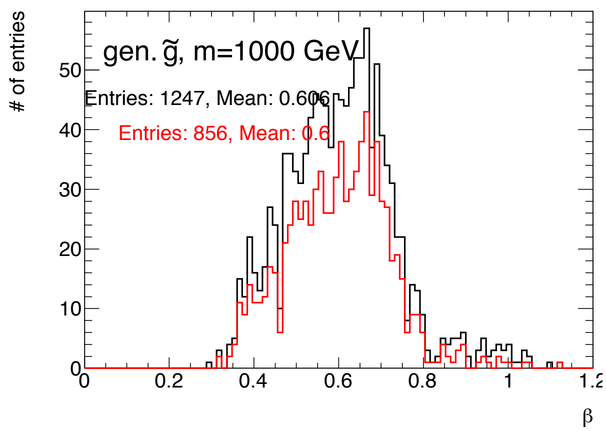

(c) muon (p_T 20 GeV) RoI

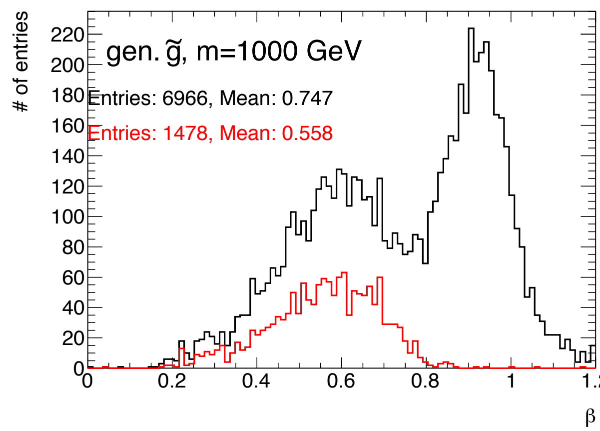

(d) No RoI

Figure 5.2: *β distribution of candidates found in the Tile Calorimeter scan of regions of interest based on 5.2(a) jet (E_T 5 GeV), 5.2(b) τ (E_T 5 GeV), 5.2(c) μ (p_T 20 GeV) and 5.2(d) a full scan for $\tilde{g}$ of 1000 GeV with the generic interaction model and with candidates from truth matched RoIs shown marked red.*

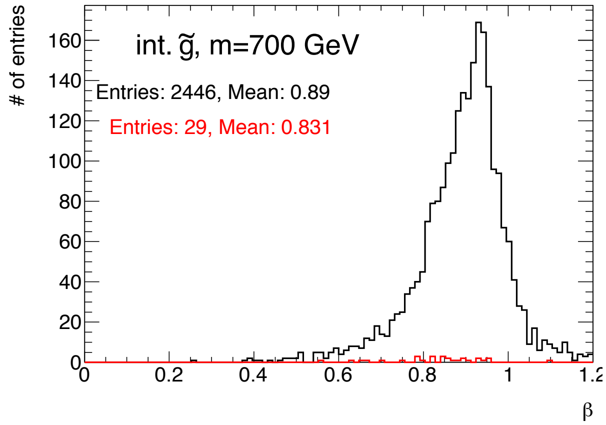

(a) jet (E_T 5 GeV) RoIs

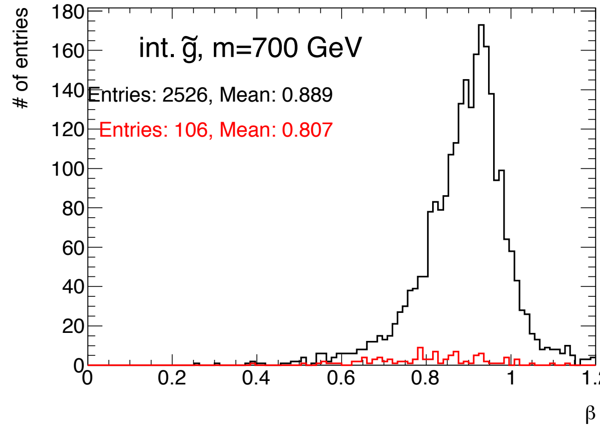

(b) tau (E_T 5 GeV) RoIs

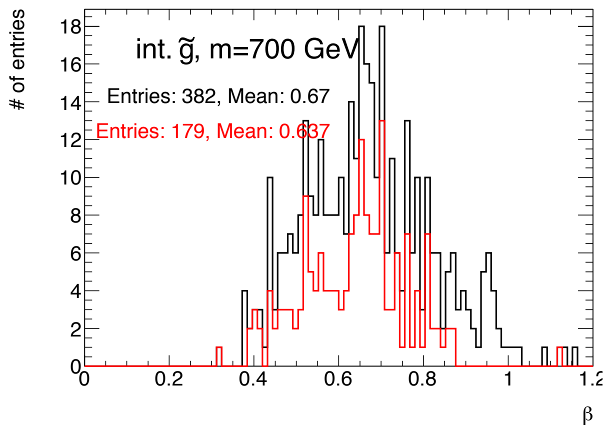

(c) muon (p_T 20 GeV) RoI

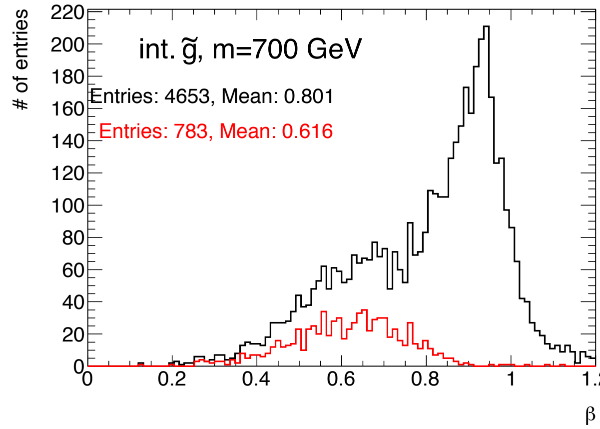

(d) No RoI

Figure 5.3: *β distribution of candidates found in the Tile Calorimeter scan of regions of interest based on 5.3(a) jet (E_T 5 GeV), 5.3(b) τ (E_T 5 GeV), 5.3(c) μ (p_T 20 GeV) and 5.3(d) a full scan for $\tilde{g}$ of 700 GeV with the intermediate interaction model and with candidates from truth matched RoIs shown marked red.*

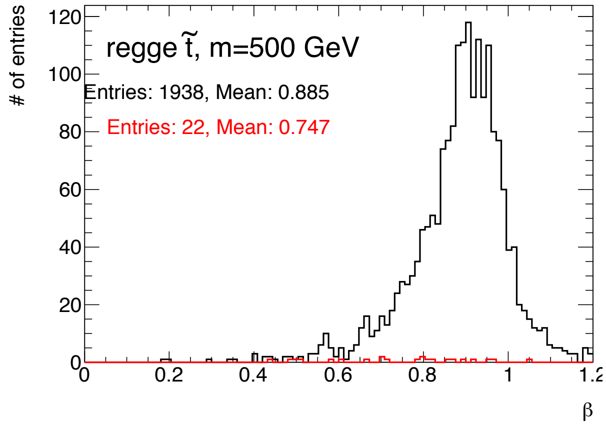

(a) jet (E_T 5 GeV) RoIs

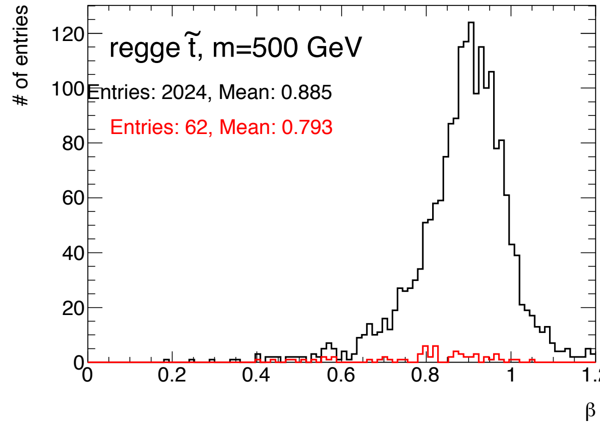

(b) tau (E_T 5 GeV) RoIs

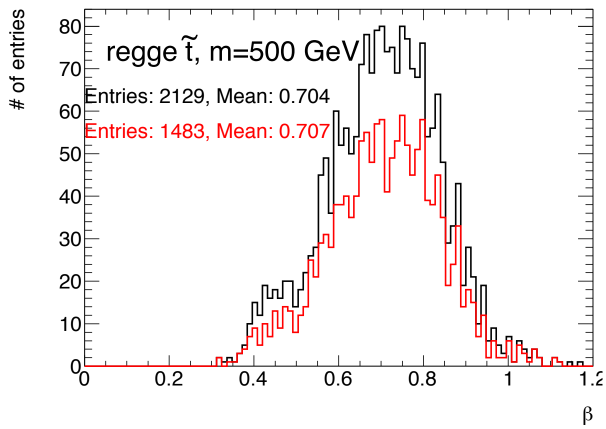

(c) muon (p_T 20 GeV) RoI

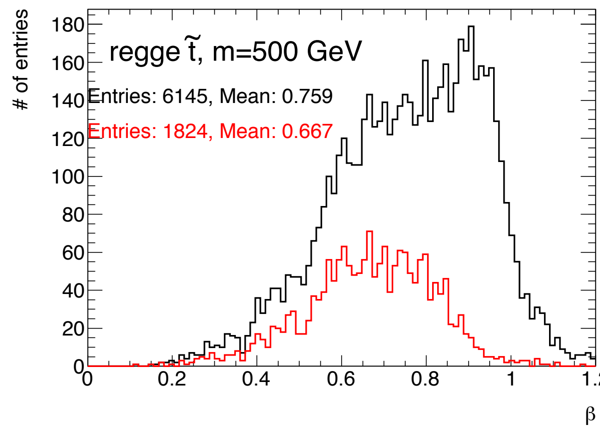

(d) No RoI

Figure 5.4: *β distribution of candidates found in the Tile Calorimeter scan of regions of interest based on 5.4(a) jet (E_T 5 GeV), 5.4(b) τ (E_T 5 GeV), 5.4(c) μ (p_T 20 GeV) and 5.4(d) a full scan for $\tilde{t}$ of 500 GeV with the regge interaction model and with candidates from truth matched RoIs shown marked red.*

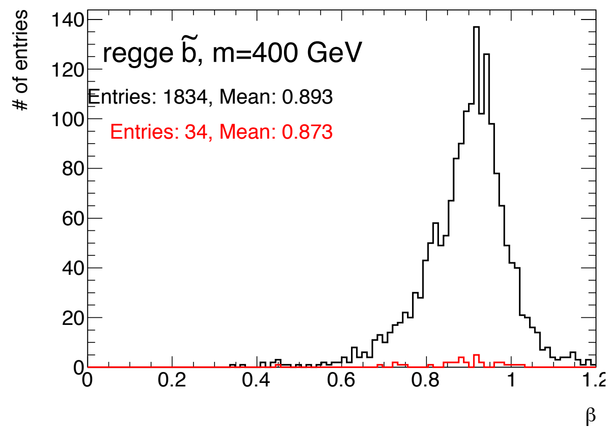

(a) jet (E_T 5 GeV) RoIs

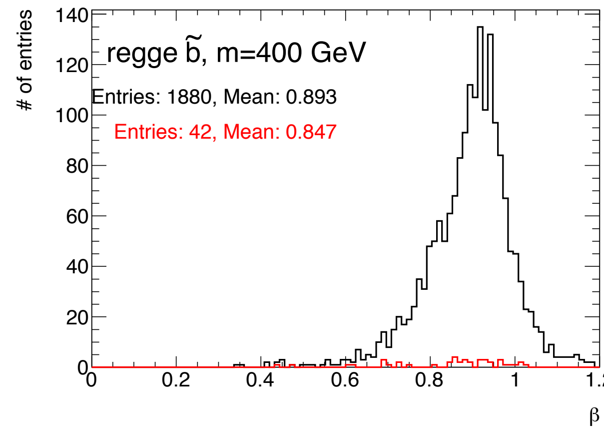

(b) tau (E_T 5 GeV) RoIs

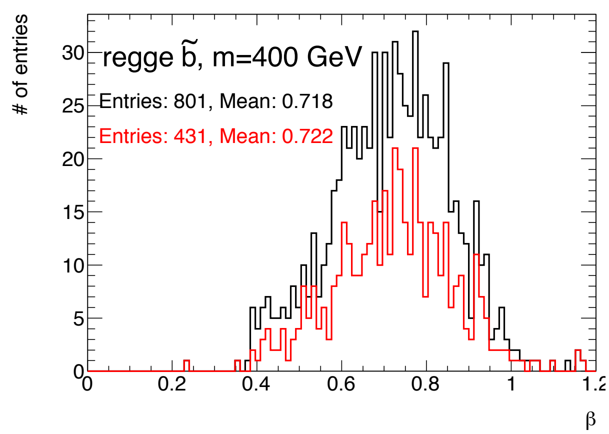

(c) muon (p_T 20 GeV) RoI

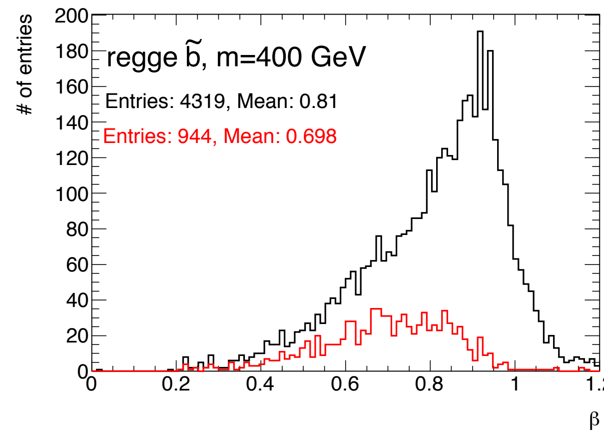

(d) No RoI

Figure 5.5: *β distribution of candidates found in the Tile Calorimeter scan of regions of interest based on 5.5(a) jet (E_T 5 GeV), 5.5(b) τ (E_T 5 GeV), 5.5(c) μ (p_T 20 GeV) and 5.5(d) a full scan for $\tilde{t}$ of 500 GeV with the regge interaction model and with candidates from truth matched RoIs shown marked red.*

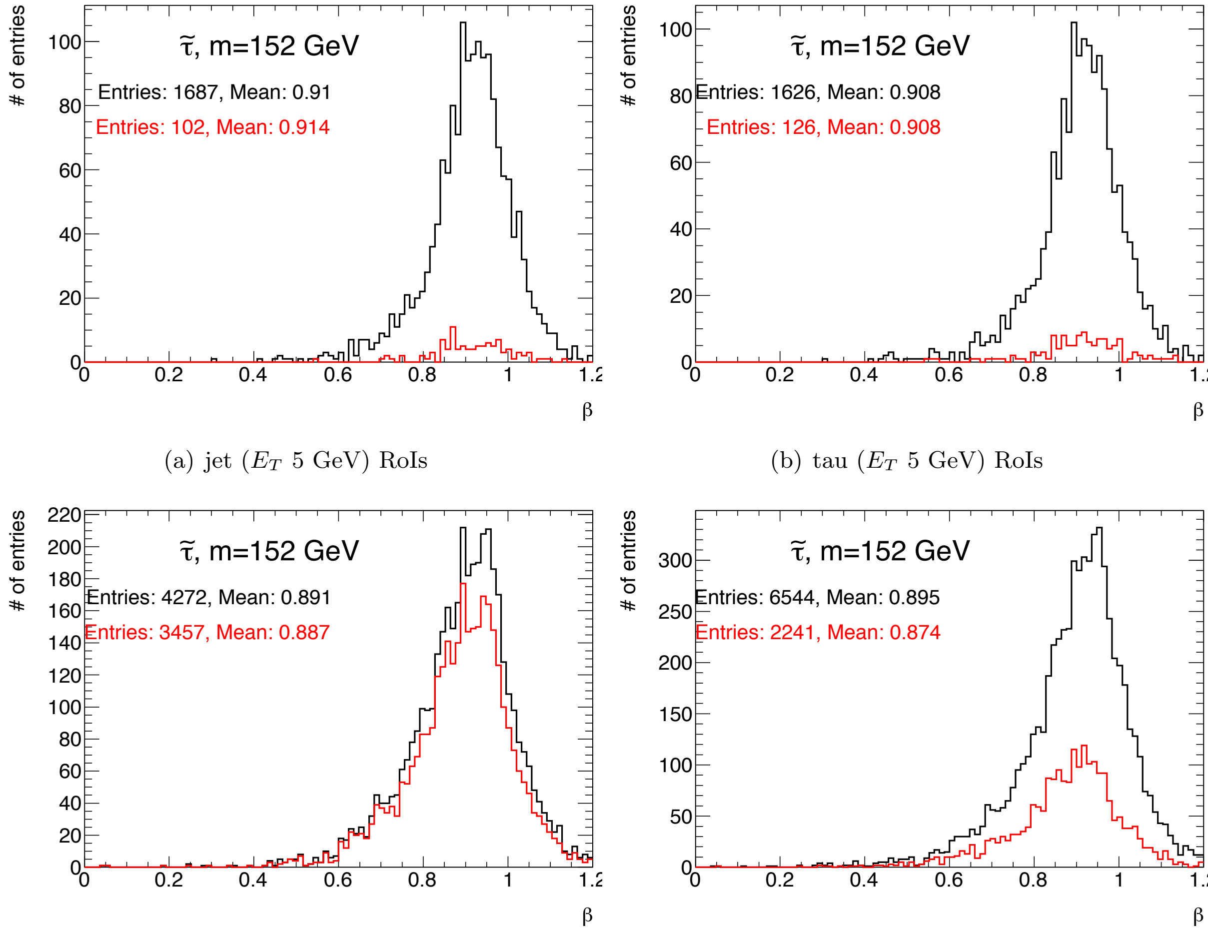

(a) jet (E_T 5 GeV) RoIs

(b) tau (E_T 5 GeV) RoIs

(c) muon (p_T 20 GeV) RoI

(d) No RoI

Figure 5.6: *β distribution of candidates found in the Tile Calorimeter scan of regions of interest based on 5.6(a) jet (E_T 5 GeV), 5.6(b) τ (E_T 5 GeV), 5.6(c) μ (p_T 20 GeV) and 5.6(d) 2 GeV deposit in the EM calorimeter for $\tilde{\tau}$ of 152 GeV and with candidates from truth matched RoIs shown marked red.*

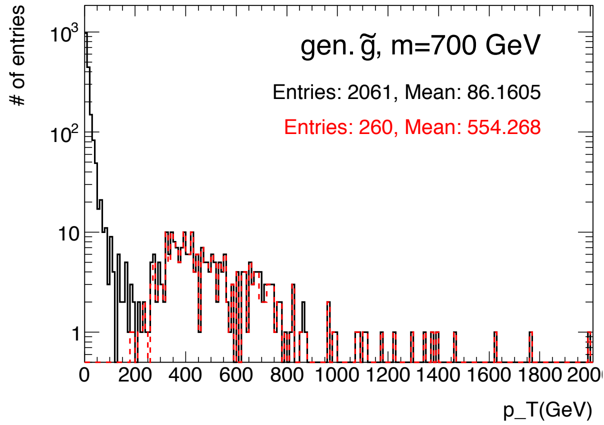

(a) jet (E_T 5 GeV) RoIs

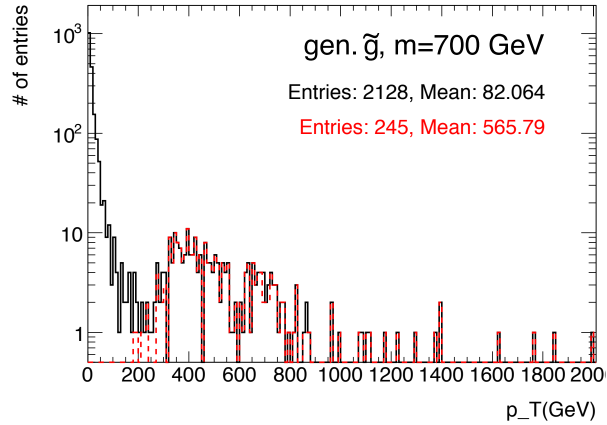

(b) tau (E_T 5 GeV) RoIs

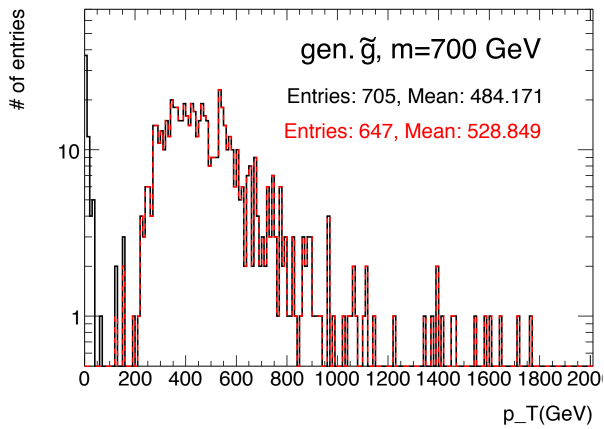

(c) muon (p_T 20 GeV) RoI

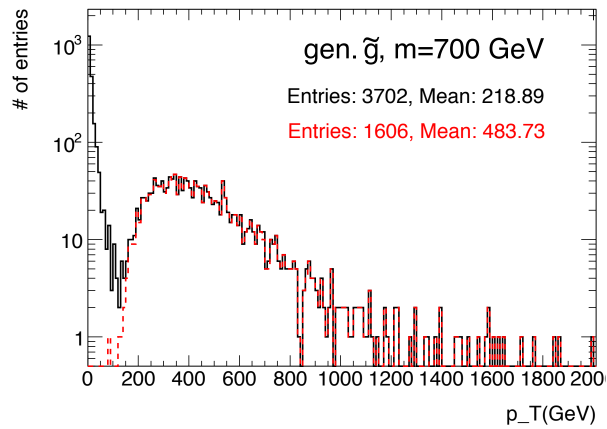

(d) unseeded

Figure 5.7: *p_T distribution of candidates found in the Tile Calorimeter scan of regions of interest based on 5.7(a) jet (E_T 5 GeV), 5.7(b) τ (E_T 5 GeV), 5.7(c) μ (p_T 20 GeV) and 5.7(d) unseeded for $\tilde{g}$ of 700 GeV with the generic interaction model and with candidates from truth matched RoIs shown marked red.*

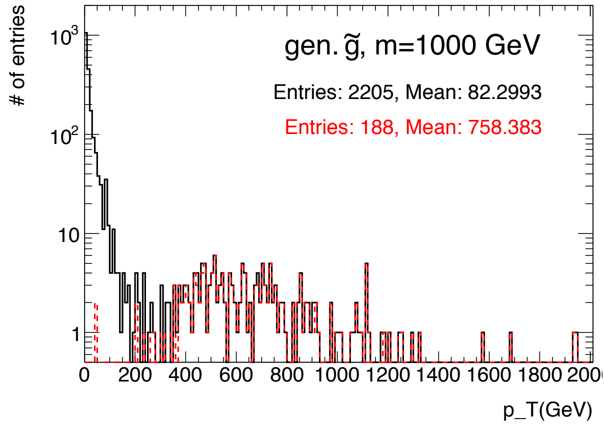

(a) jet (E_T 5 GeV) RoIs

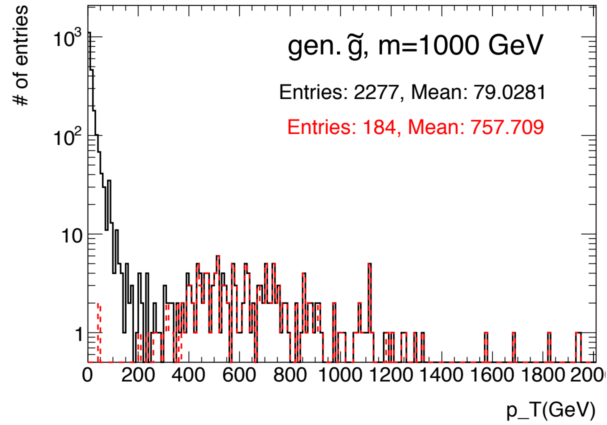

(b) tau (E_T 5 GeV) RoIs

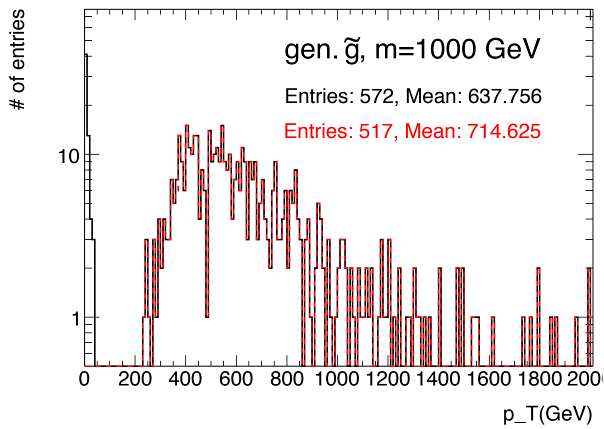

(c) muon (p_T 20 GeV) RoI

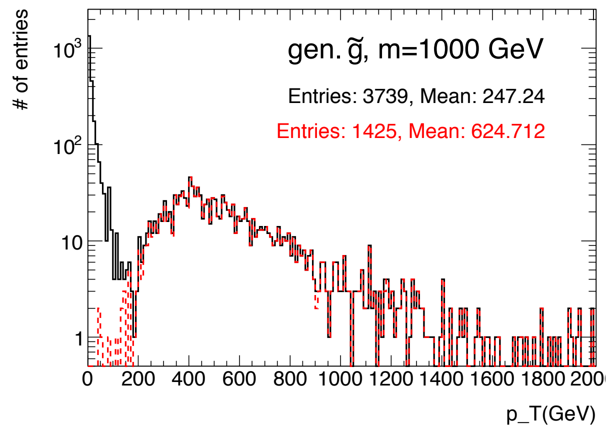

(d) unseeded

Figure 5.8: *p_T distribution of candidates found in the Tile Calorimeter scan of regions of interest based on 5.8(a) jet (E_T 5 GeV), 5.8(b) τ (E_T 5 GeV), 5.8(c) μ (p_T 20 GeV) and 5.8(d) unseeded for $\tilde{g}$ of 1000 GeV with the generic interaction model and with candidates from truth matched RoIs shown marked red.*

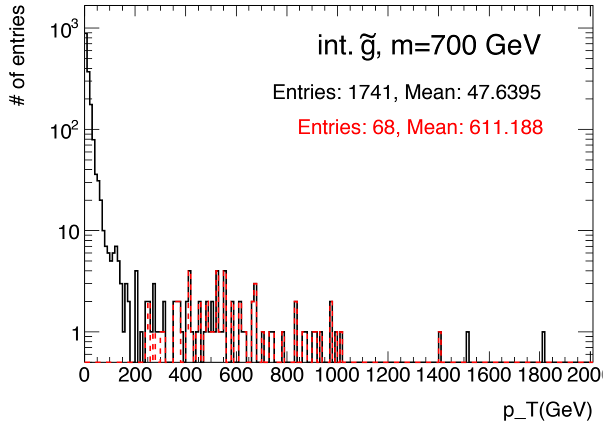

(a) jet (E_T 5 GeV) RoIs

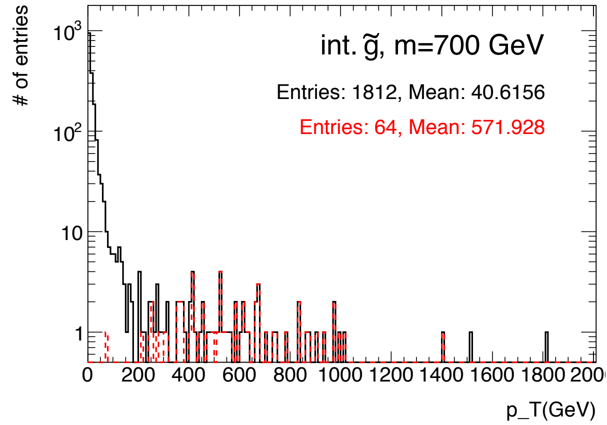

(b) tau (E_T 5 GeV) RoIs

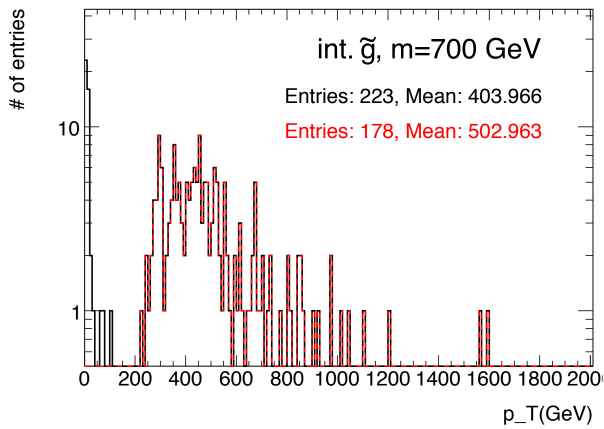

(c) muon (p_T 20 GeV) RoI

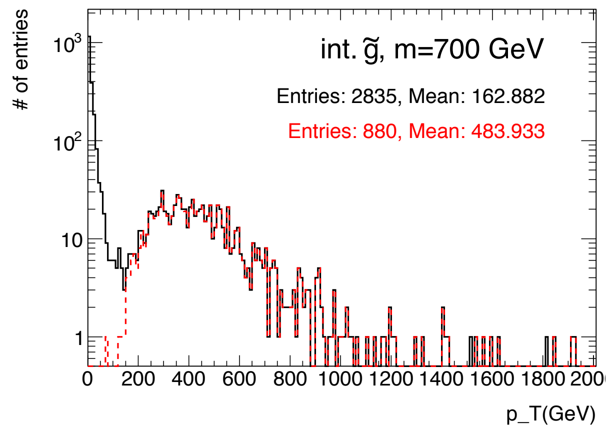

(d) unseeded

Figure 5.9: *p_T distribution of candidates found in the tile calorimeter scan of regions of interest based on 5.9(a) jet (E_T 5 GeV), 5.9(b) τ (E_T 5 GeV), 5.9(c) μ (p_T 20 GeV) and 5.9(d) unseeded for $\tilde{g}$ of 700 GeV with the intermediate interaction model and with candidates from truth matched RoIs shown marked red.*

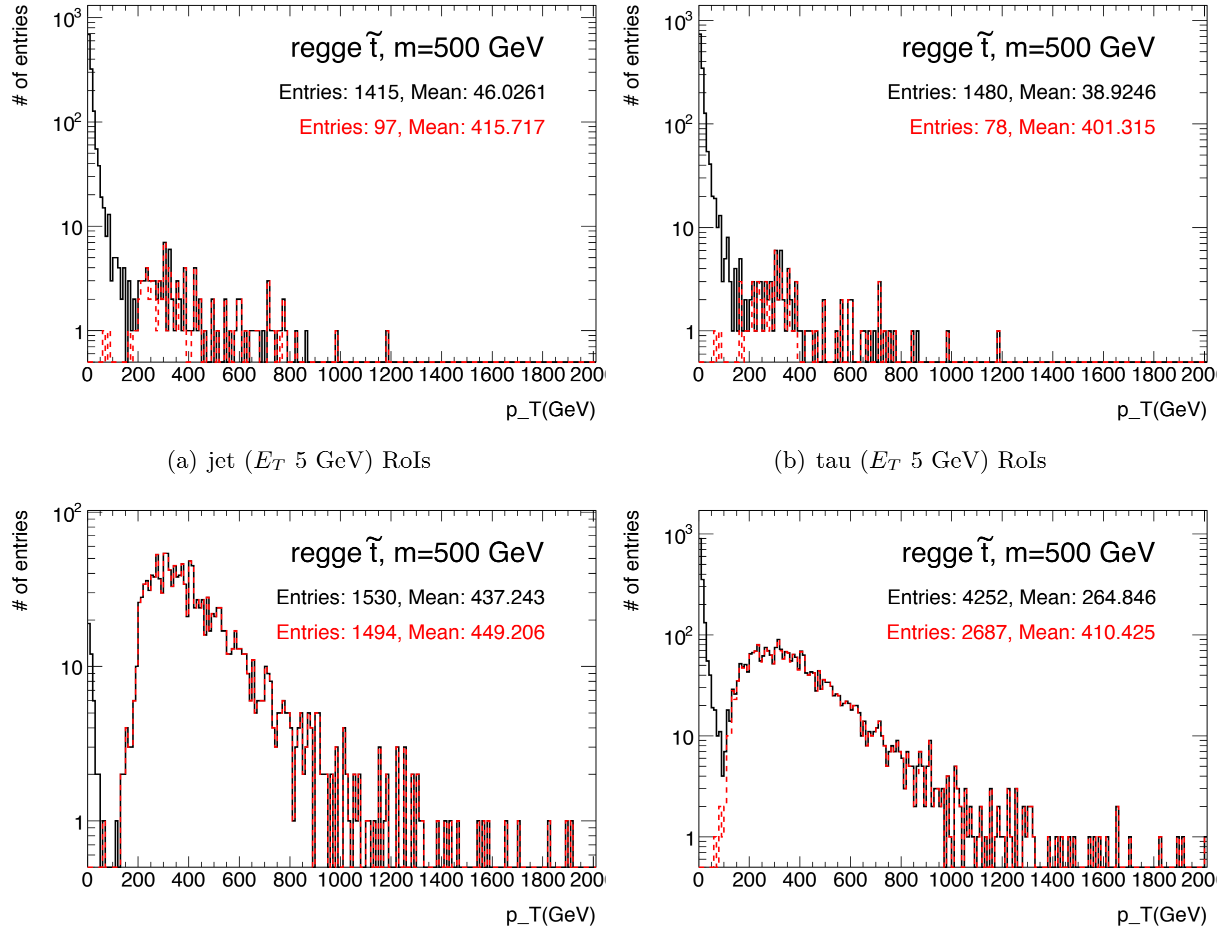

(a) jet (E_T 5 GeV) RoIs

(b) tau (E_T 5 GeV) RoIs

(c) muon (p_T 20 GeV) RoI

(d) unseeded

Figure 5.10: *p_T distribution of candidates found in the Tile Calorimeter scan of regions of interest based on 5.10(a) jet (E_T 5 GeV), 5.10(b) τ (E_T 5 GeV), 5.10(c) μ (p_T 20 GeV) and 5.10(d) unseeded for $\tilde{t}$ of 500 GeV with the regge interaction model and with candidates from truth matched RoIs shown marked red.*

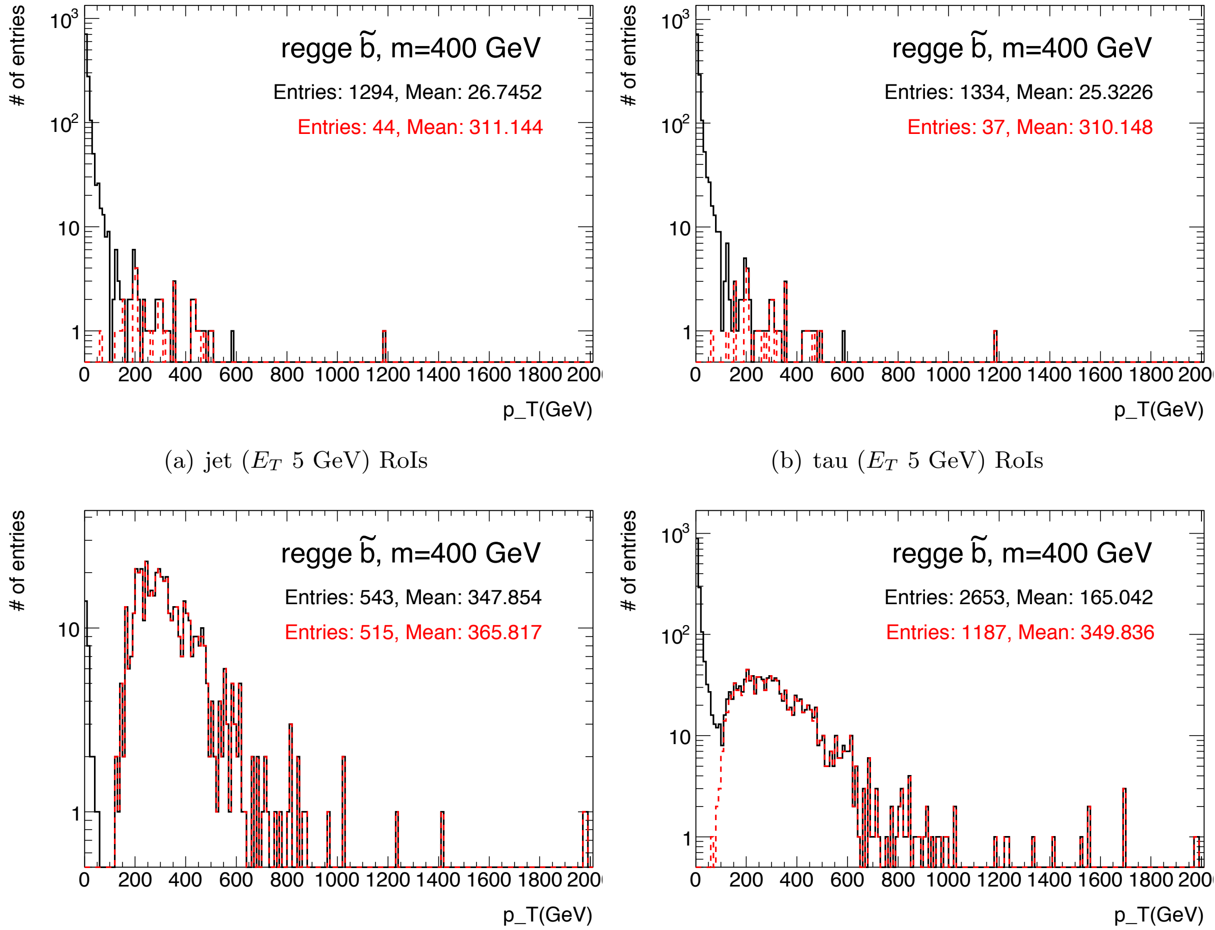

(a) jet (E_T 5 GeV) RoIs

(b) tau (E_T 5 GeV) RoIs

(c) muon (p_T 20 GeV) RoI

(d) unseeded

Figure 5.11: *p_T distribution of candidates found in the Tile Calorimeter scan of regions of interest based on 5.11(a) jet (E_T 5 GeV), 5.11(b) τ (E_T 5 GeV), 5.11(c) μ (p_T 20 GeV) and 5.11(d) unseeded for $\tilde{b}$ of 400 GeV with the regge interaction model and with candidates from truth matched RoIs shown marked red.*

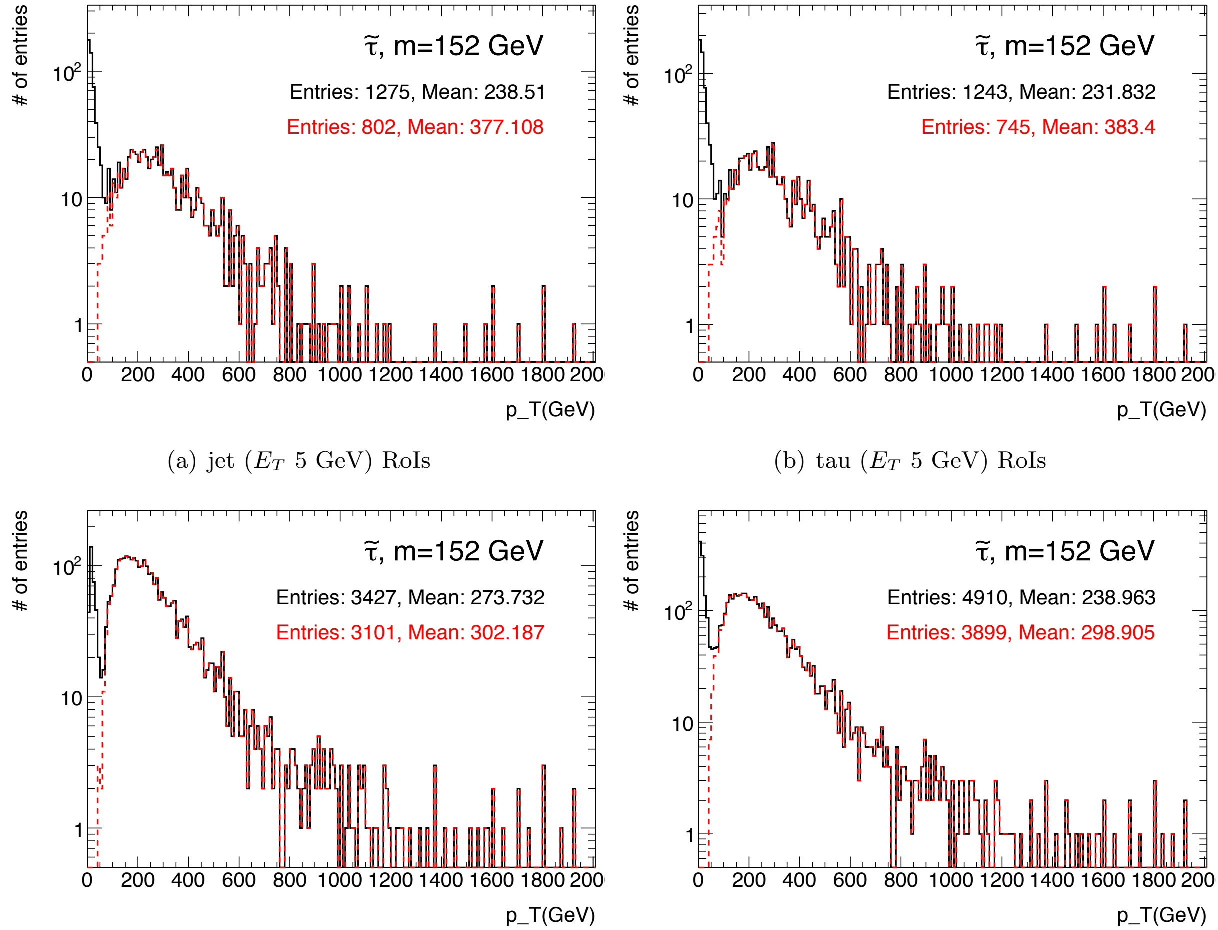

(a) jet (E_T 5 GeV) RoIs

(b) tau (E_T 5 GeV) RoIs

(c) muon (p_T 20 GeV) RoI

(d) No RoI

Figure 5.12: *p_T distribution of candidates found in the Tile Calorimeter scan of regions of interest based on 5.12(a) jet (E_T 5 GeV), 5.12(b) τ (E_T 5 GeV), 5.12(c) μ (p_T 20 GeV) and 5.12(d) a full scan for $\tilde{\tau}$ of 152 GeV and with candidates from truth matched RoIs shown marked red.*

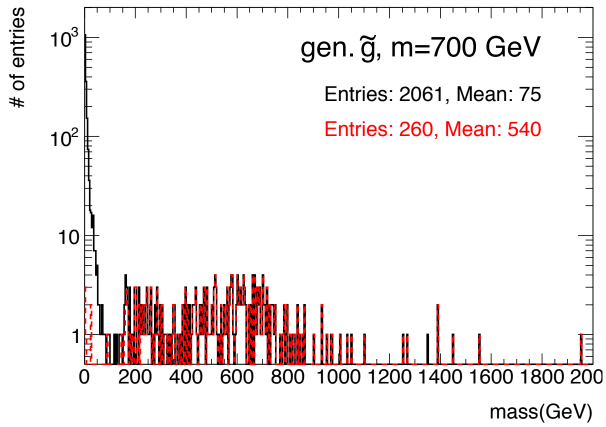

(a) jet (E_T 5 GeV) RoIs

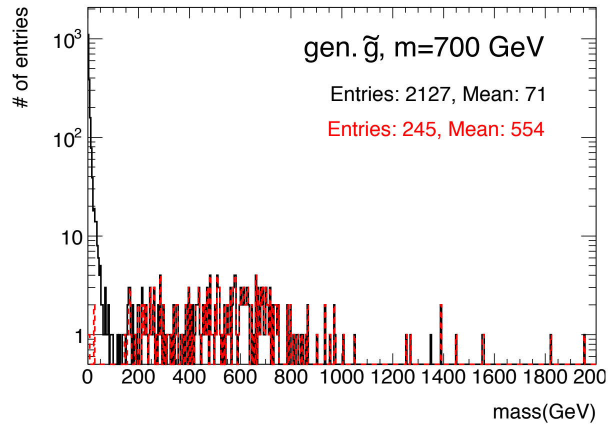

(b) tau (E_T 5 GeV) RoIs

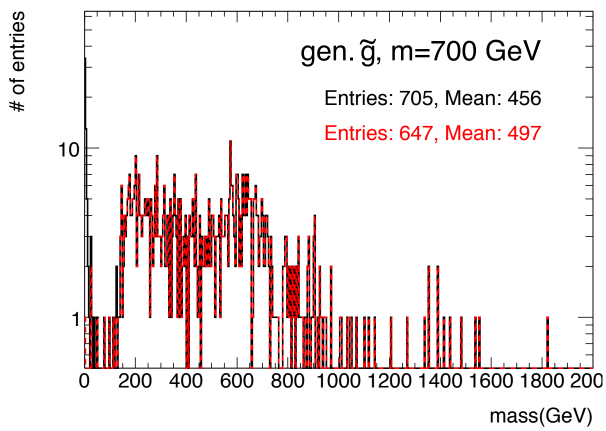

(c) muon (p_T 20 GeV) RoI

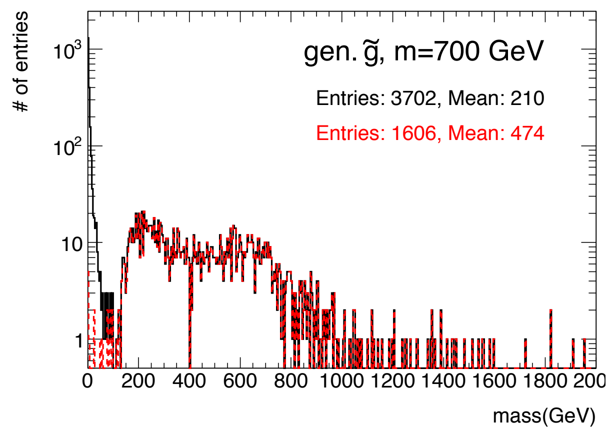

(d) No RoI

Figure 5.13: *Mass distribution of candidates found in the Tile Calorimeter scan of regions of interest based on 5.13(a) jet (E_T 5 GeV), 5.13(b) τ (E_T 5 GeV), 5.13(c) μ (p_T 20 GeV) and 5.13(d) a full scan for $\tilde{g}$ of 700 GeV with the generic interaction model and with candidates from truth matched RoIs shown marked red.*

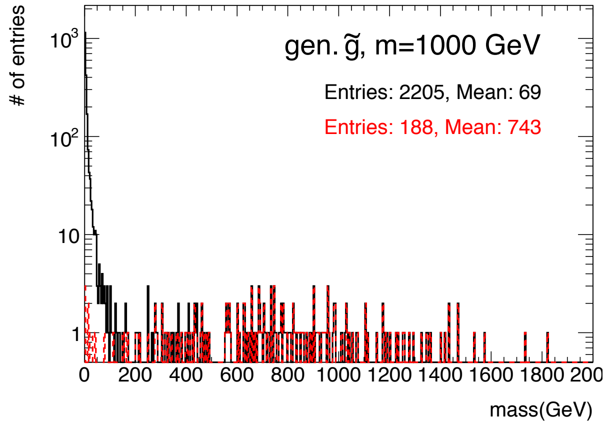

(a) jet (E_T 5 GeV) RoIs

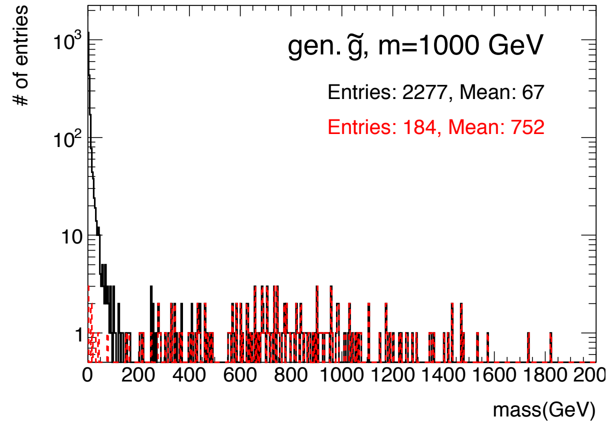

(b) tau (E_T 5 GeV) RoIs

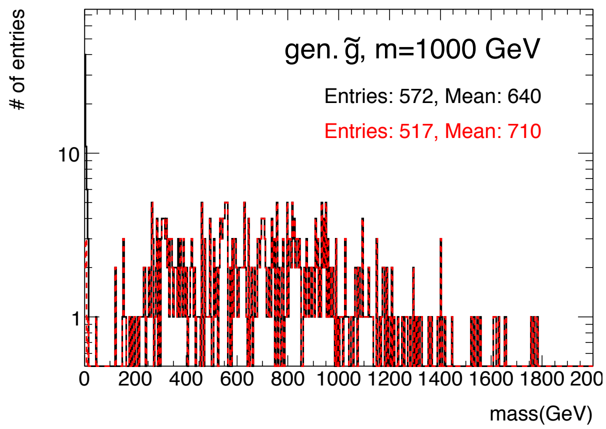

(c) muon (p_T 20 GeV) RoI

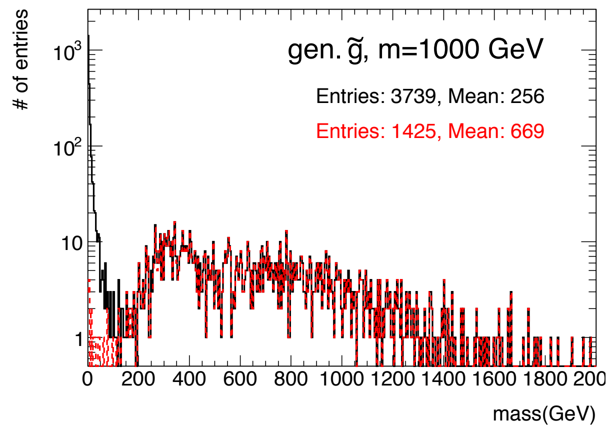

(d) No RoI

Figure 5.14: *Mass distribution of candidates found in the Tile Calorimeter scan of regions of interest based on 5.14(a) jet (E_T 5 GeV), 5.14(b) τ (E_T 5 GeV), 5.14(c) μ (p_T 20 GeV) and 5.14(d) a full scan for $\tilde{g}$ of 1000 GeV with the generic interaction model and with candidates from truth matched RoIs shown marked red.*

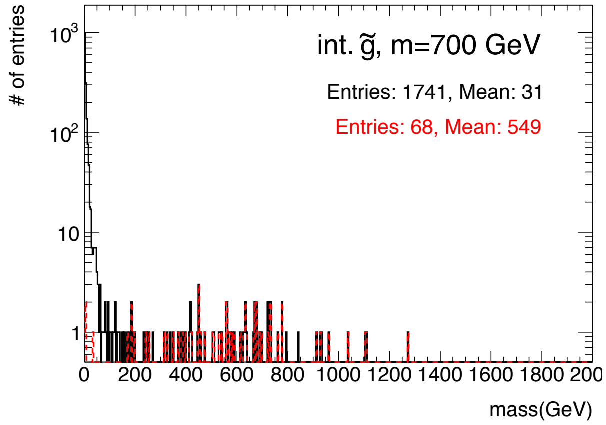

(a) jet (E_T 5 GeV) RoIs

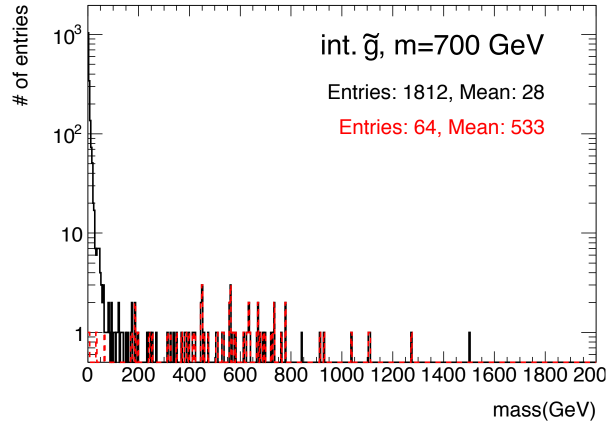

(b) tau (E_T 5 GeV) RoIs

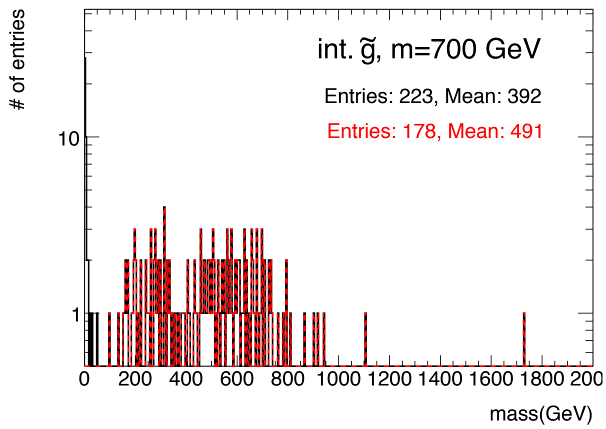

(c) muon (p_T 20 GeV) RoI

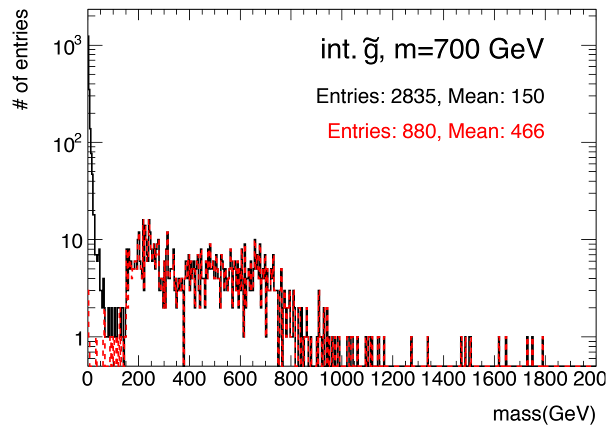

(d) No RoI

Figure 5.15: *Mass distribution of candidates found in the Tile Calorimeter scan of regions of interest based on 5.15(a) jet (E_T 5 GeV), 5.15(b) τ (E_T 5 GeV), 5.15(c) μ (p_T 20 GeV) and 5.15(d) a full scan for $\tilde{g}$ of 700 GeV with the intermediate interaction model and with candidates from truth matched RoIs shown marked red.*

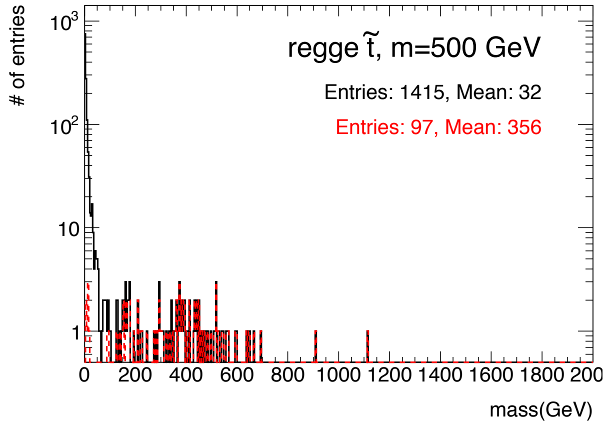

(a) jet (E_T 5 GeV) RoIs

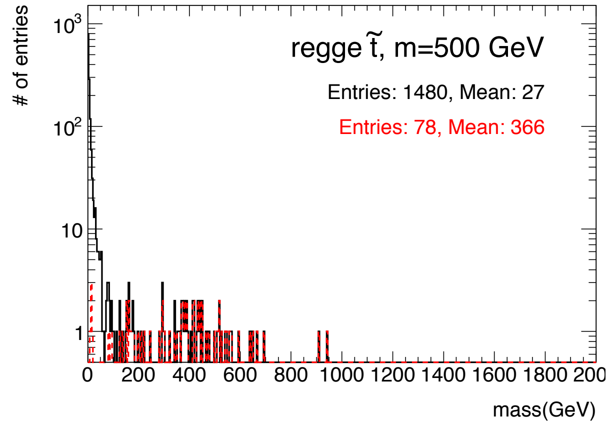

(b) tau (E_T 5 GeV) RoIs

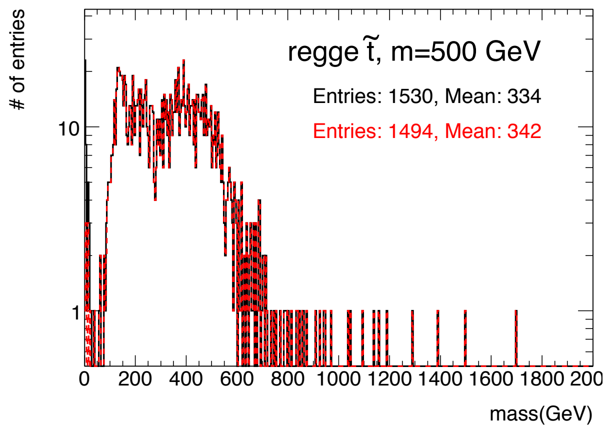

(c) muon (p_T 20 GeV) RoI

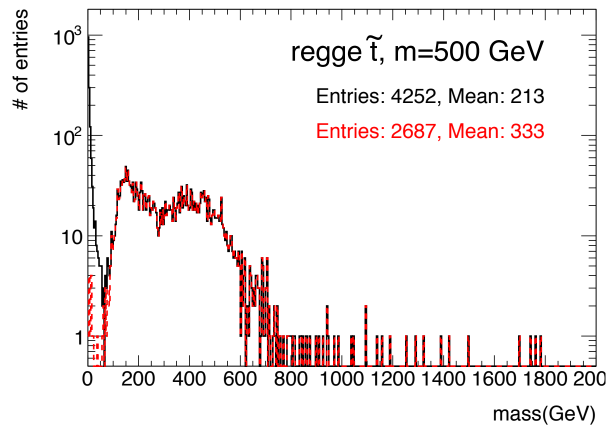

(d) No RoI

Figure 5.16: *Mass distribution of candidates found in the Tile Calorimeter scan of regions of interest based on 5.16(a) jet (E_T 5 GeV), 5.16(b) τ (E_T 5 GeV), 5.16(c) μ (p_T 20 GeV) and 5.16(d) a full scan for $\tilde{t}$ of 500 GeV with the regge interaction model and with candidates from truth matched RoIs shown marked red.*

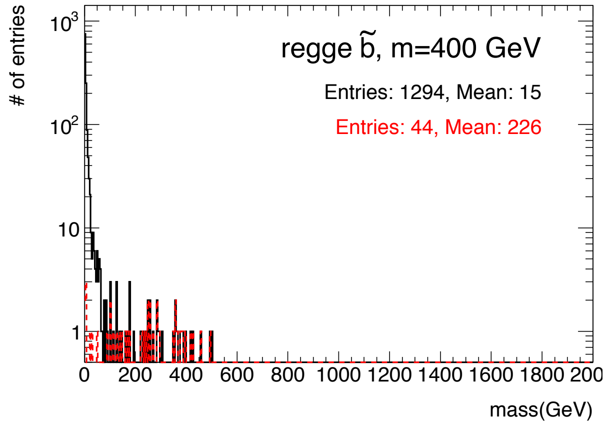

(a) jet (E_T 5 GeV) RoIs

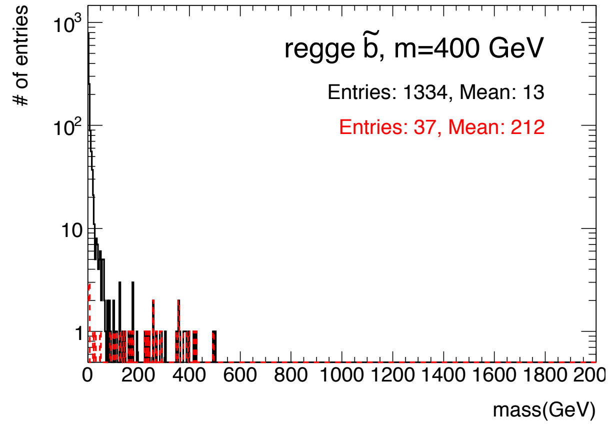

(b) tau (E_T 5 GeV) RoIs

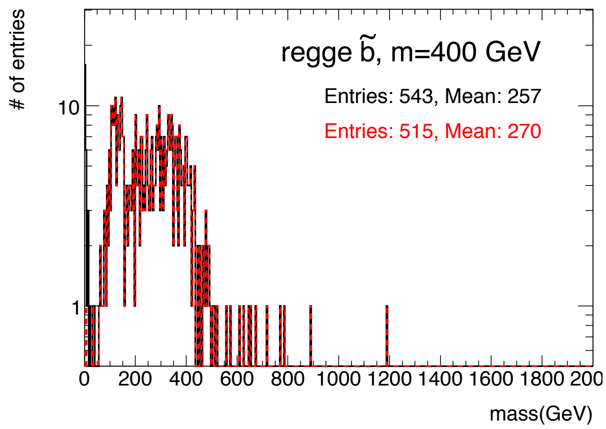

(c) muon (p_T 20 GeV) RoI

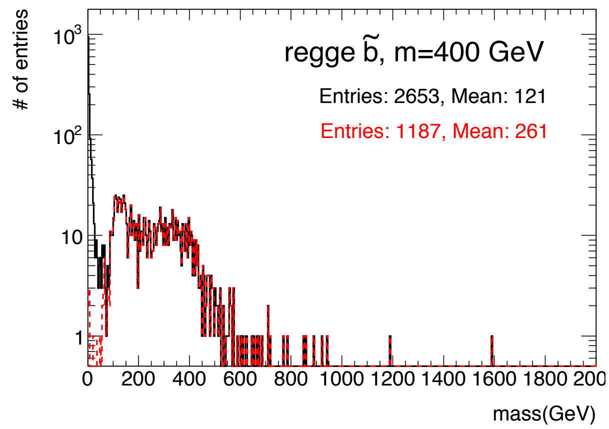

(d) No RoI

Figure 5.17: *Mass distribution of candidates found in the Tile Calorimeter scan of regions of interest based on 5.17(a) jet (E_T 5 GeV), 5.17(b) τ (E_T 5 GeV), 5.17(c) μ (p_T 20 GeV) and 5.17(d) a full scan for $\tilde{t}$ of 500 GeV with the regge interaction model and with candidates from truth matched RoIs shown marked red.*

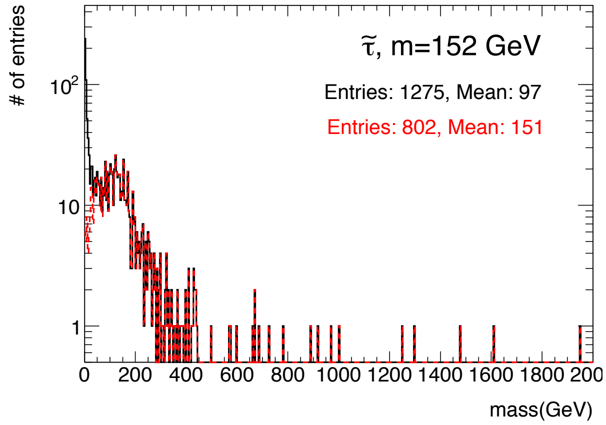

(a) jet (E_T 5 GeV) RoIs

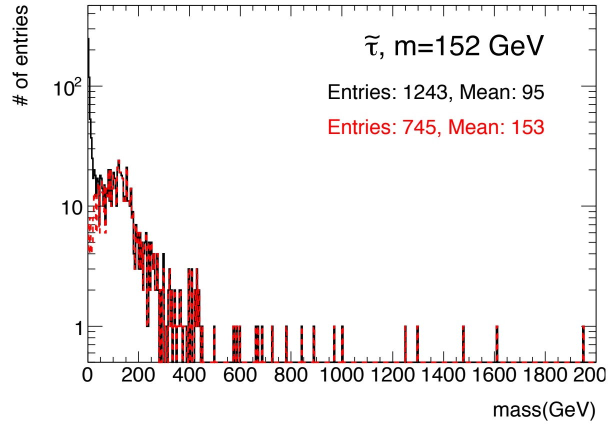

(b) tau (E_T 5 GeV) RoIs

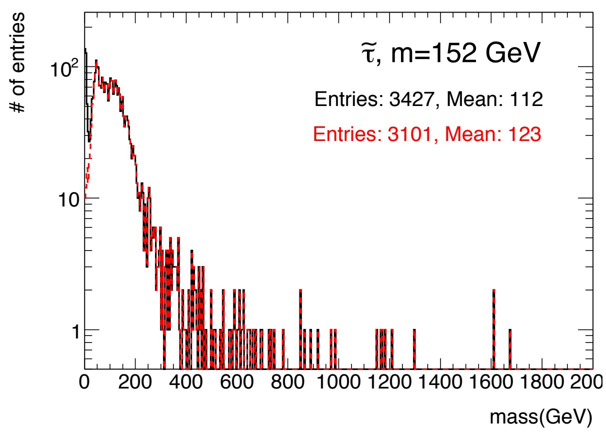

(c) muon (p_T 20 GeV) RoI

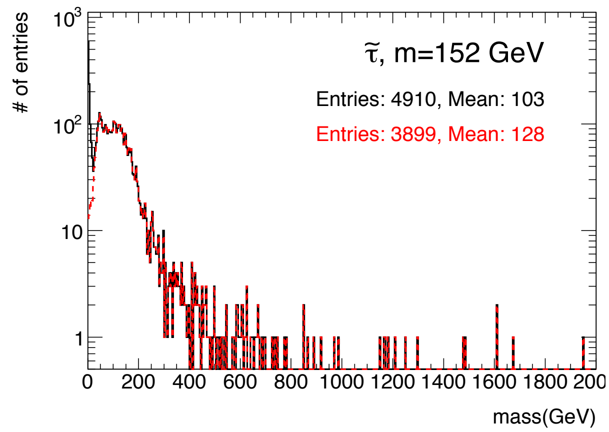

(d) No RoI

Figure 5.18: *Mass distribution of candidates found in the Tile Calorimeter scan of regions of interest based on 5.18(a) jet (E_T 5 GeV), 5.18(b) τ (E_T 5 GeV), 5.18(c) μ (p_T 20 GeV) and 5.18(d) a full scan for $\tilde{\tau}$ of 152 GeV and with candidates from truth matched RoIs shown marked red.*

5.0.2 Background plots

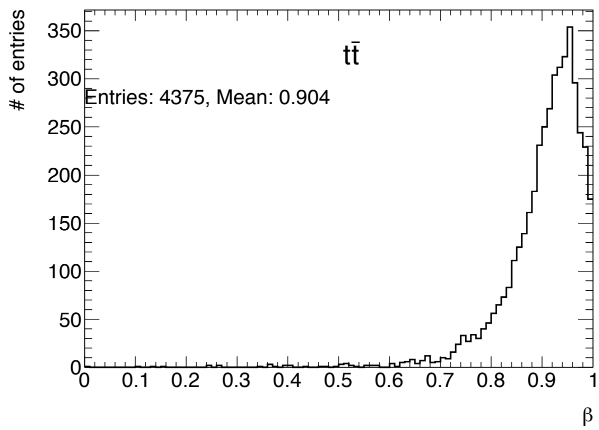

(a) jet (E_T 5 GeV) RoIs

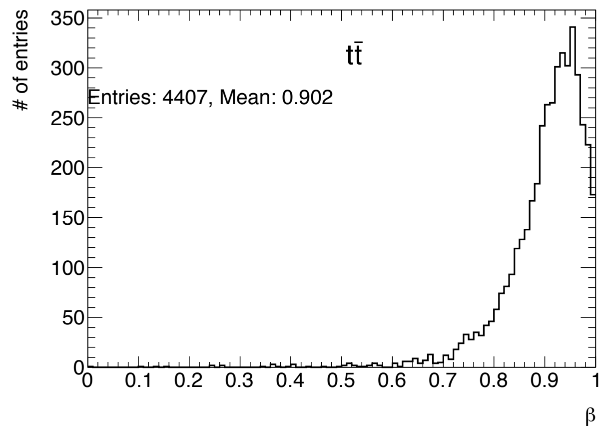

(b) tau (E_T 5 GeV) RoIs

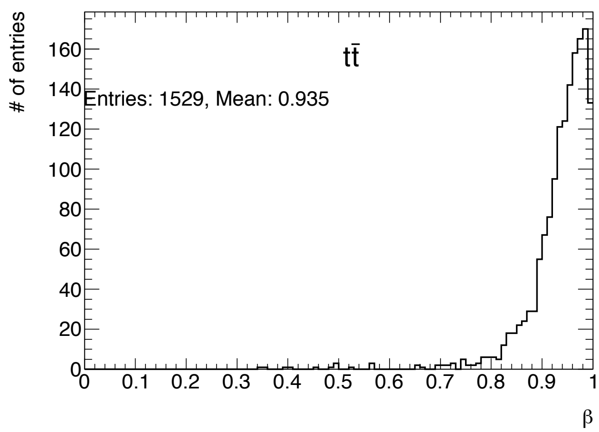

(c) muon (p_T 20 GeV) RoI

Figure 5.19: *Beta distribution of particles in $t\bar{t}$ events surviving L2 selection in the Tile Calorimeter. The three distributions result from scanning the Tile Calorimeter with different L1 regions of interest based on (a) single jet with E_T 5 GeV, (b) single τ with E_T 5 GeV and single μ with p_T 20 GeV.*

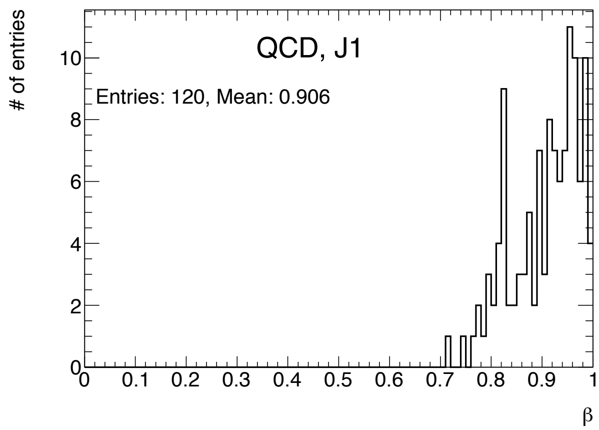

(a) jet (E_T 5 GeV) RoIs

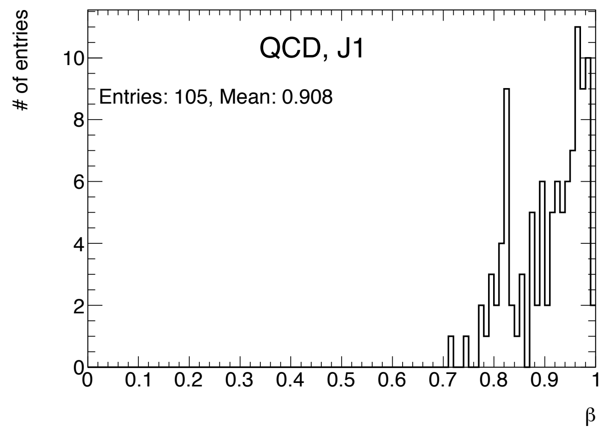

(b) tau (E_T 5 GeV) RoIs

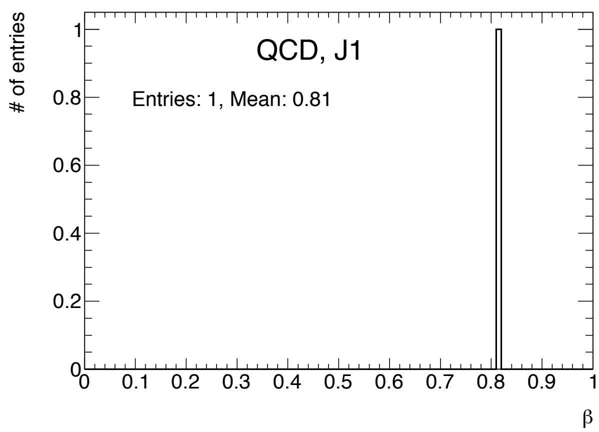

(c) muon (p_T 20 GeV) RoI

Figure 5.20: *Beta distribution of particles in QCD di-jet events surviving L2 selection in the Tile Calorimeter. The three distributions result from scanning the Tile Calorimeter with different L1 regions of interest based on (a) single jet with E_T 5 GeV, (b) single τ with E_T 5 GeV and single μ with p_T 20 GeV.*

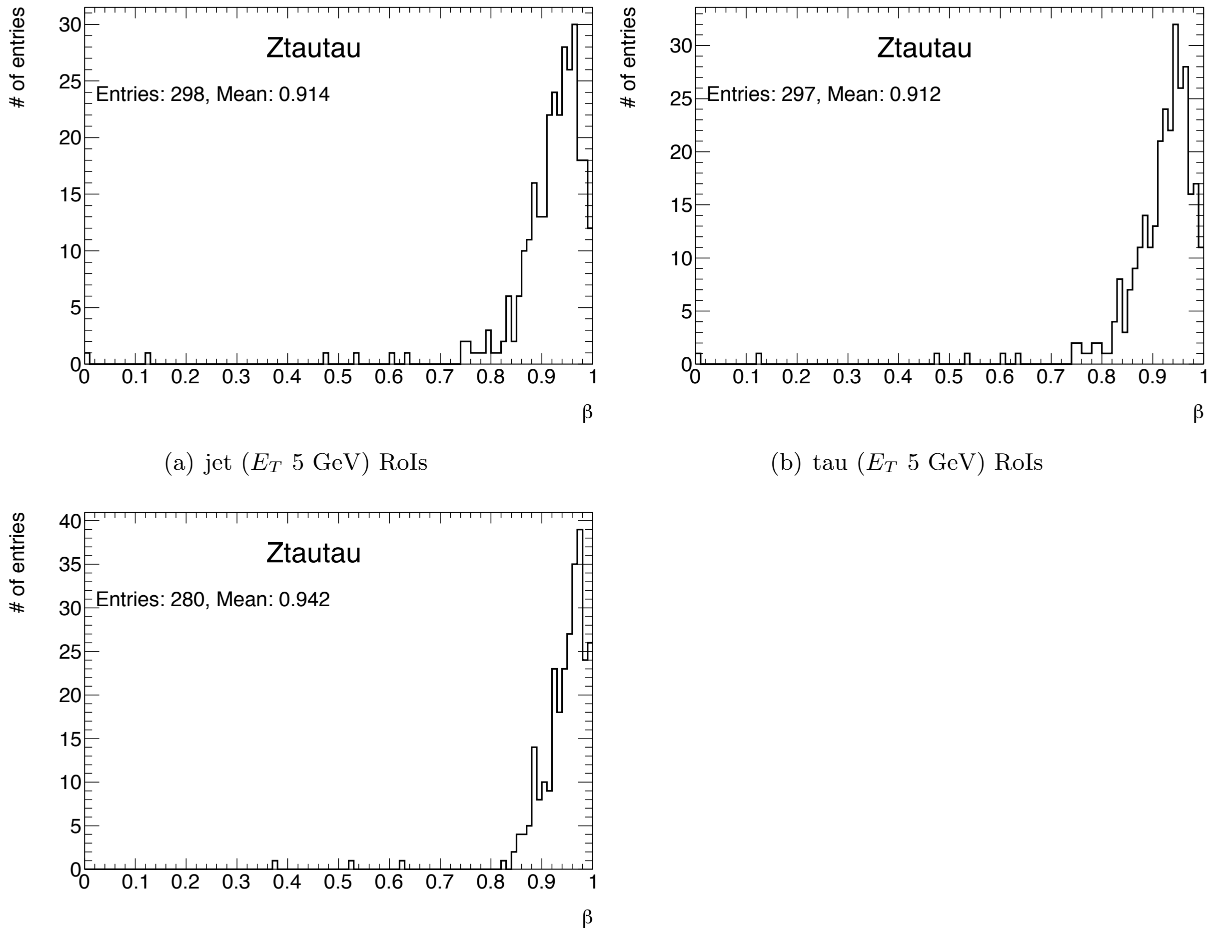

(a) jet (E_T 5 GeV) RoIs

(b) tau (E_T 5 GeV) RoIs

(c) muon (p_T 20 GeV) RoI

Figure 5.21: *Beta distribution of particles in Z→ $\tau\tau$ events surviving L2 selection in the Tile Calorimeter. The three distributions result from scanning the Tile Calorimeter with different L1 regions of interest based on (a) single jet with E_T 5 GeV, (b) single τ with E_T 5 GeV and single μ with p_T 20 GeV.*

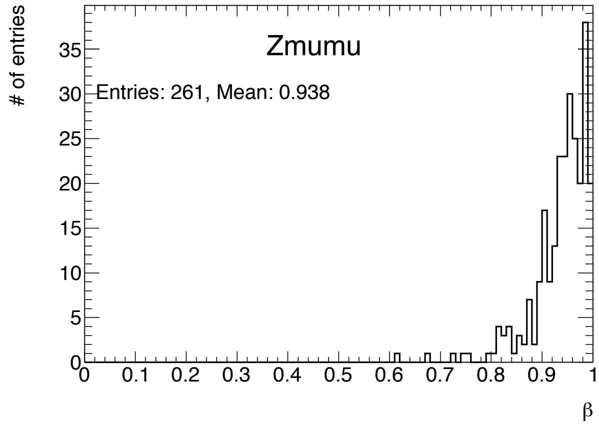

(a) jet (E_T 5 GeV) RoIs

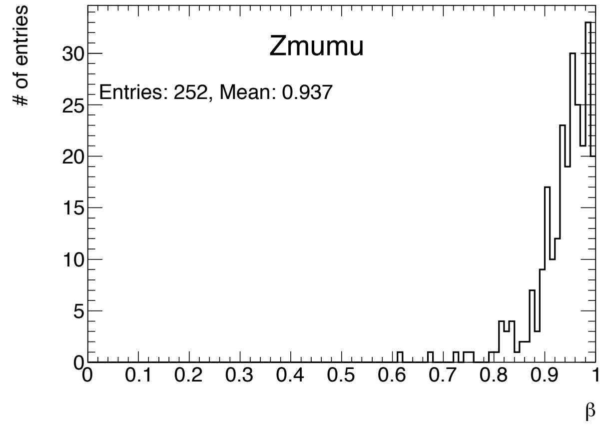

(b) tau (E_T 5 GeV) RoIs

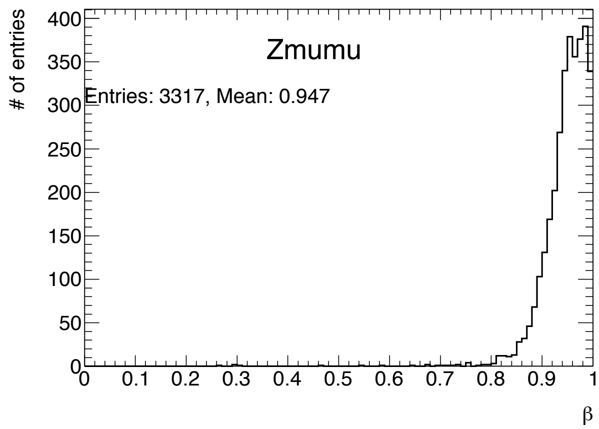

(c) muon (p_T 20 GeV) RoI

Figure 5.22: *Beta distribution of particles in $Z \to \mu\mu$ events surviving L2 selection in the Tile Calorimeter. The three distributions result from scanning the Tile Calorimeter with different L1 regions of interest based on (a) single jet with E_T 5 GeV, (b) single τ with E_T 5 GeV and single μ with p_T 20 GeV.*

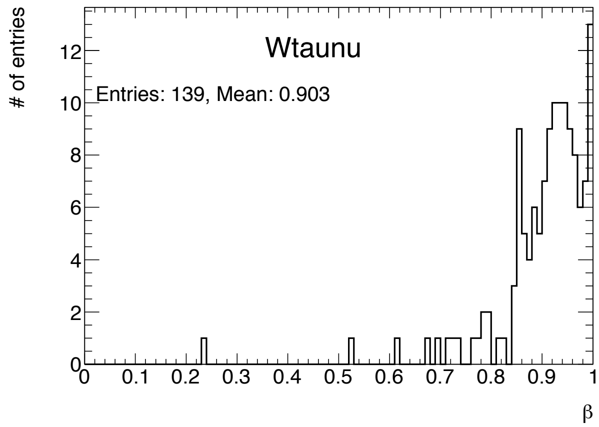

(a) jet (E_T 5 GeV) RoIs

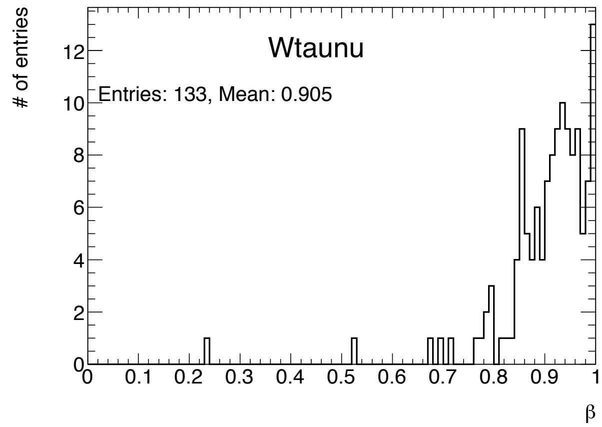

(b) tau (E_T 5 GeV) RoIs

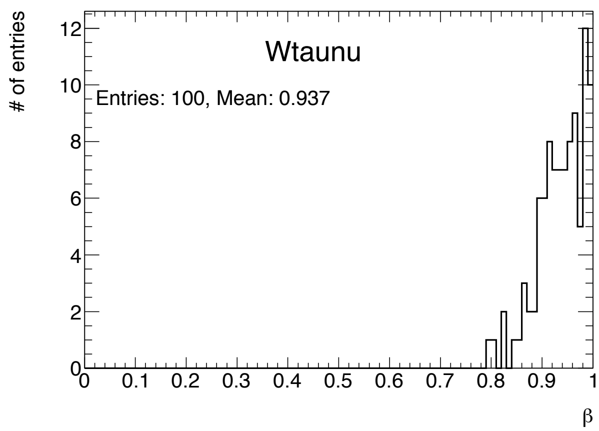

(c) muon (p_T 20 GeV) RoI

Figure 5.23: *Beta distribution of particles in $W\tau\nu$ events surviving L2 selection in the Tile Calorimeter. The three distributions result from scanning the Tile Calorimeter with different L1 regions of interest based on (a) single jet with E_T 5 GeV, (b) single τ with E_T 5 GeV and single μ with p_T 20 GeV.*

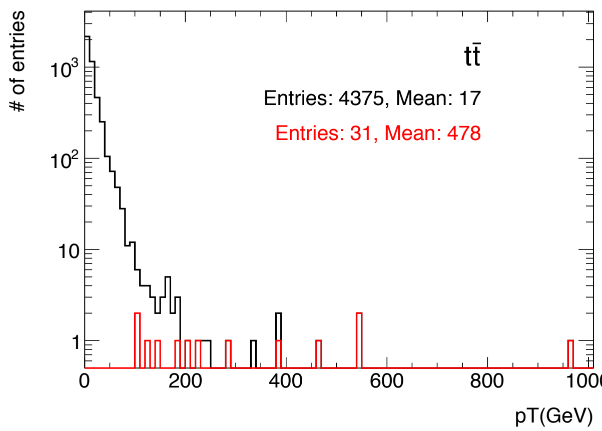

(a) jet (E_T 5 GeV) RoIs

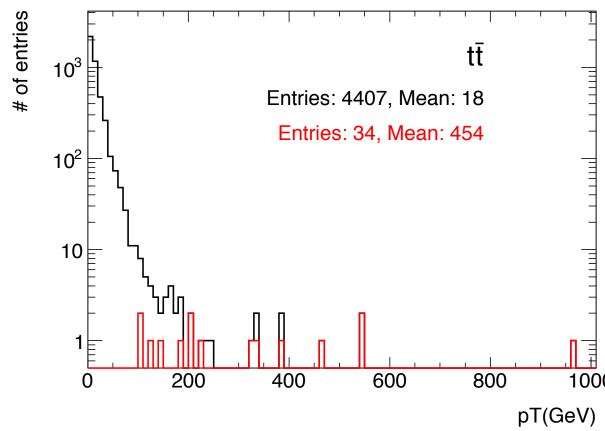

(b) tau (E_T 5 GeV) RoIs

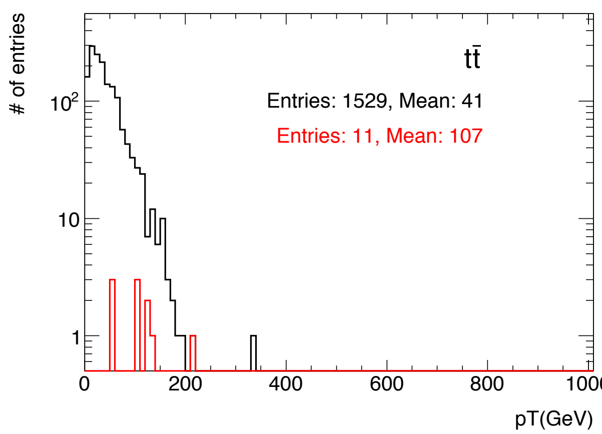

(c) muon (p_T 20 GeV) RoI

Figure 5.24: *Transverse momentum distribution of particles in $t\bar{t}$ events surviving L2 selection in the Tile Calorimeter and having a matching ID track. The three distribution were based on seeding the chain with different regions of interest based on (a) single jet with E_T 5 GeV, (b) single τ with E_T 5 GeV and (c) single μ with p_T 20 GeV. The distributions marked* red *result from setting a upper cut of 100 GeV on the mass variable obtained from combining the β-estimate and the ID momentum estimate, as described in Section 4.4.*

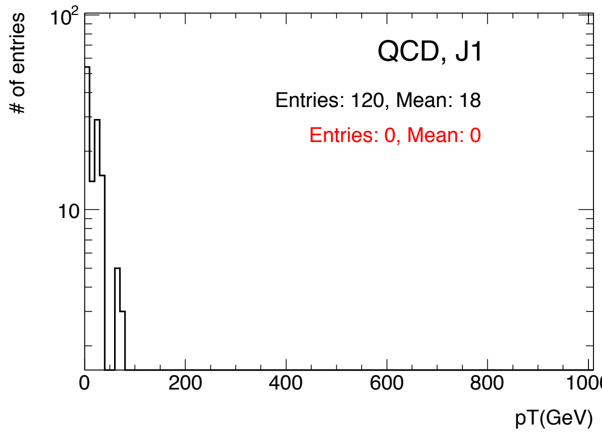

(a) jet (E_T 5 GeV) RoIs

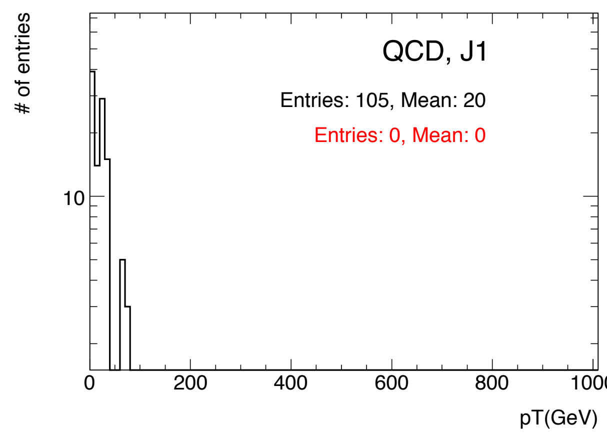

(b) tau (E_T 5 GeV) RoIs

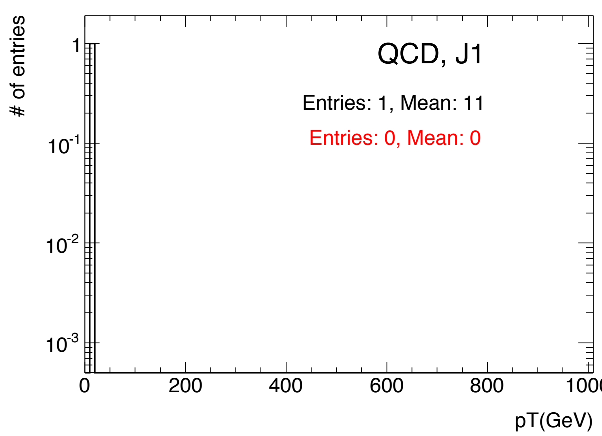

(c) muon (p_T 20 GeV) RoI

Figure 5.25: *Transverse momentum distribution of particles in QCD di-jet events surviving L2 selection in the Tile Calorimeter and having a matching ID track. The three distribution were based on seeding the chain with different regions of interest based on (a) single jet with E_T 5 GeV, (b) single τ with E_T 5 GeV and (c) single μ with p_T 20 GeV. The distributions marked* red *result from setting a upper cut of 100 GeV on the mass variable obtained from combining the β-estimate and the ID momentum estimate, as described in Section 4.4.*

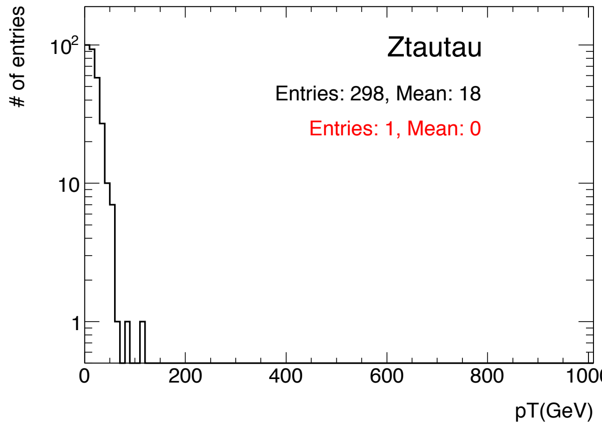

(a) jet (E_T 5 GeV) RoIs

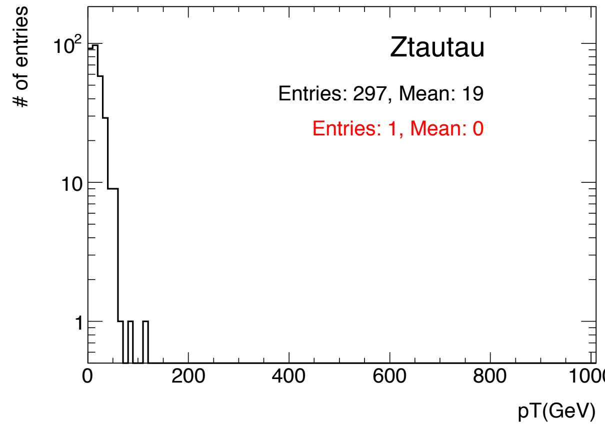

(b) tau (E_T 5 GeV) RoIs

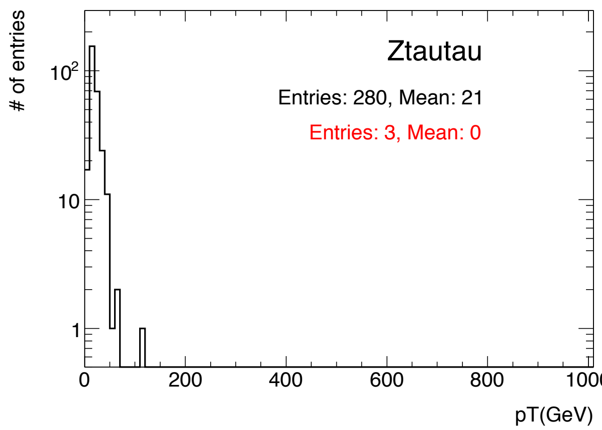

(c) muon (p_T 20 GeV) RoI

Figure 5.26: *Transverse momentum distribution of particles in $Z \to \tau\tau$ events surviving L2 selection in the Tile Calorimeter and having a matching ID track. The three distribution were based on seeding the chain with different regions of interest based on (a) single jet wiht E_T 5 GeV, (b) single τ with E_T 5 GeV and (c) single μ with p_T 20 GeV. The distributions marked* red *result from setting a upper cut of 100 GeV on the mass variable obtained from combining the β-estimate and the ID momentum estimate, as described in Section 4.4.*

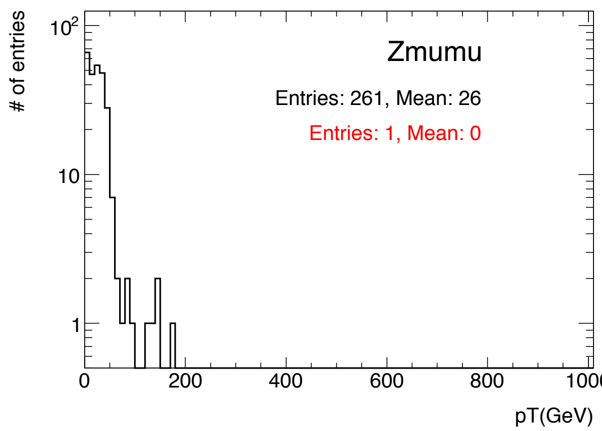

(a) jet (E_T 5 GeV) RoIs

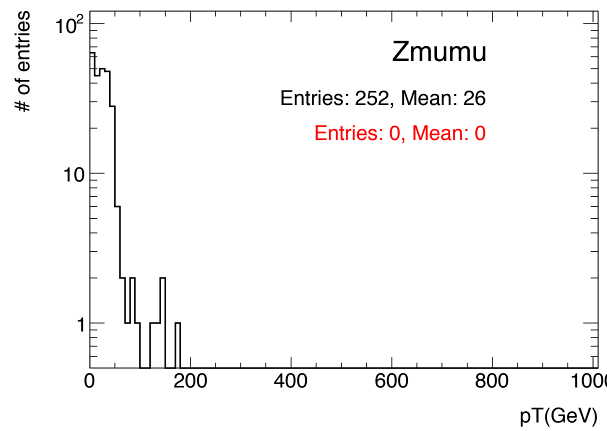

(b) tau (E_T 5 GeV) RoIs

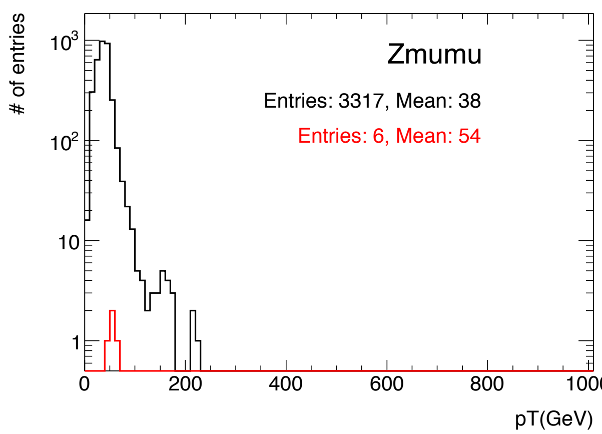

(c) muon (p_T 20 GeV) RoI

Figure 5.27: *Transverse momentum distribution of particles in $Z \rightarrow \mu\mu$ events surviving L2 selection in the Tile Calorimeter and having a matching ID track. The three distribution were based on seeding the chain with different regions of interest based on (a) single jet wiht E_T 5 GeV, (b) single τ with E_T 5 GeV and (c) single μ with p_T 20 GeV. The distributions marked* red *result from setting a upper cut of 100 GeV on the mass variable obtained from combining the β-estimate and the ID momentum estimate, as described in Section 4.4.*

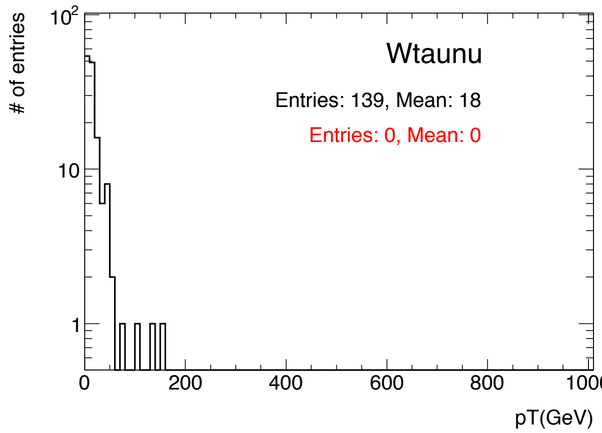

(a) jet (E_T 5 GeV) RoIs

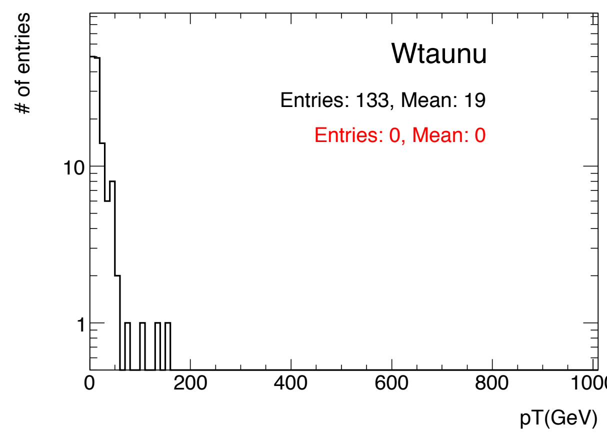

(b) tau (E_T 5 GeV) RoIs

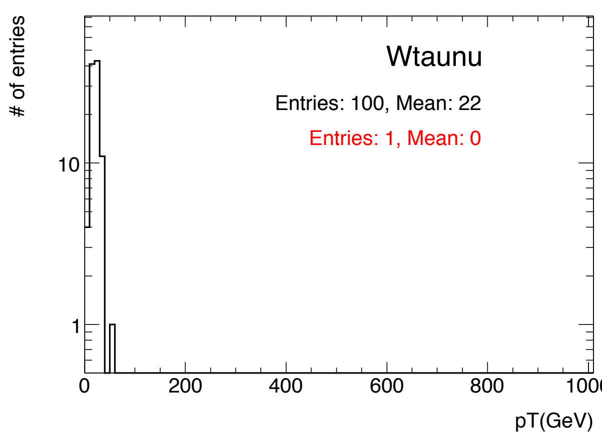

(c) muon (p_T 20 GeV) RoI

Figure 5.28: *Transverse momentum distribution of particles in $Z \to \mu\mu$ events surviving L2 selection in the Tile Calorimeter and having a matching ID track. The three distribution were based on seeding the chain with different regions of interest based on (a) single jet wiht E_T 5 GeV, (b) single τ with E_T 5 GeV and (c) single μ with p_T 20 GeV. The distributions marked* red *result from setting a upper cut of 100 GeV on the mass variable obtained from combining the β-estimate and the ID momentum estimate, as described in Section 4.4.*

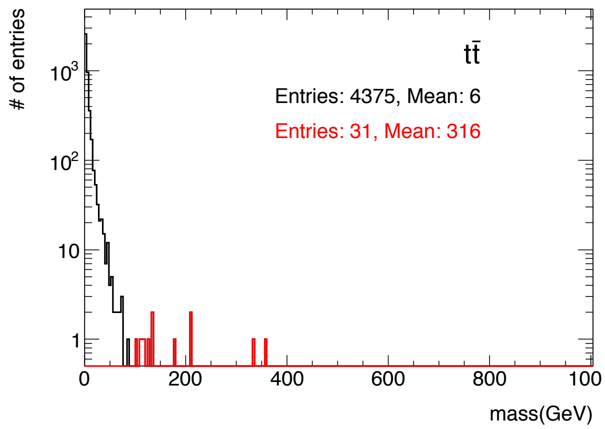

(a) jet (E_T 5 GeV) RoIs

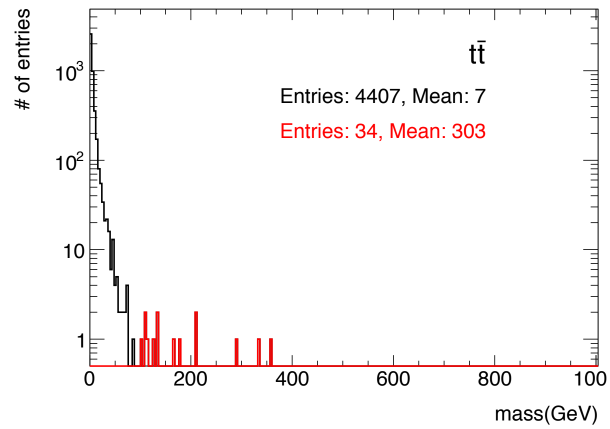

(b) tau (E_T 5 GeV) RoIs

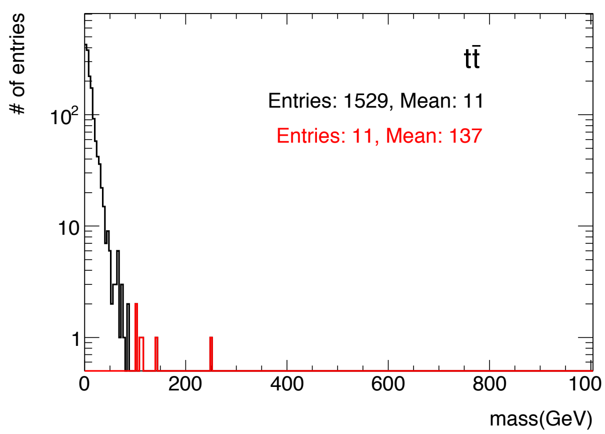

(c) muon (p_T 20 GeV) RoI

Figure 5.29: *Mass distribution of particles in $t\bar{t}$ events surviving L2 selection in the Tile Calorimeter and having a matching ID track. The three distribution were based on seeding the chain with different regions of interest based on (a) single jet wiht E_T 5 GeV, (b) single τ with E_T 5 GeV and (c) single μ with p_T 20 GeV. The distributions marked* red *result from setting a upper cut of 100 GeV on the mass variable obtained from combining the β-estimate and the ID momentum estimate, as described in Section 4.4.*

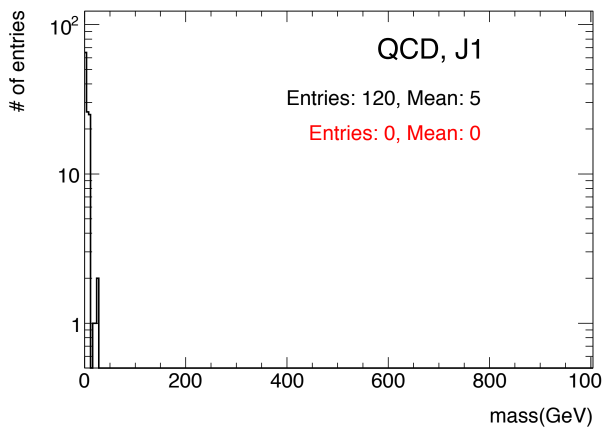

(a) jet (E_T 5 GeV) RoIs

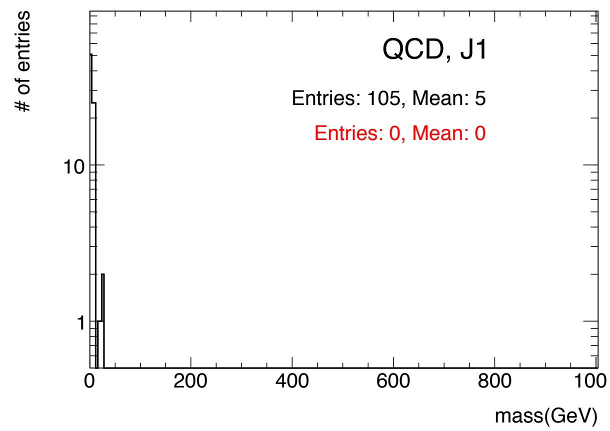

(b) tau (E_T 5 GeV) RoIs

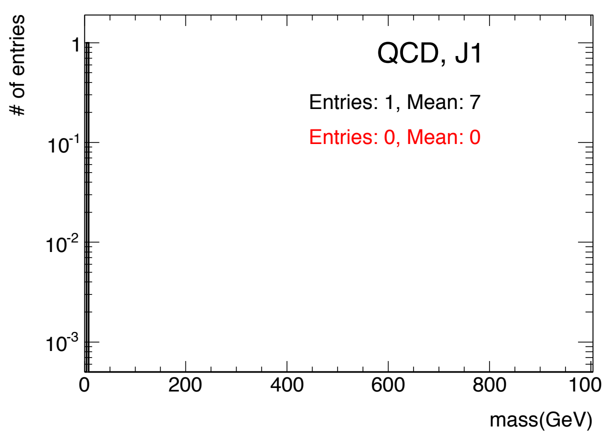

(c) muon (p_T 20 GeV) RoI

Figure 5.30: *Mass distribution of particles in QCD di-jet events surviving L2 selection in the Tile Calorimeter and having a matching ID track. The three distribution were based on seeding the chain with different regions of interest based on (a) single jet wiht E_T 5 GeV, (b) single τ with E_T 5 GeV and (c) single μ with p_T 20 GeV. The distributions marked* red *result from setting a upper cut of 100 GeV on the mass variable obtained from combining the β-estimate and the ID momentum estimate, as described in Section 4.4.*

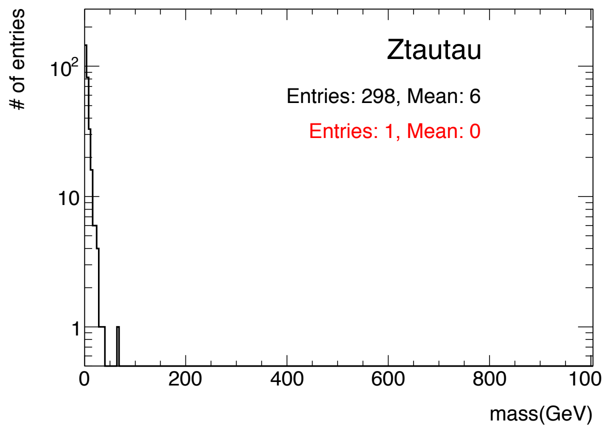

(a) jet (E_T 5 GeV) RoIs

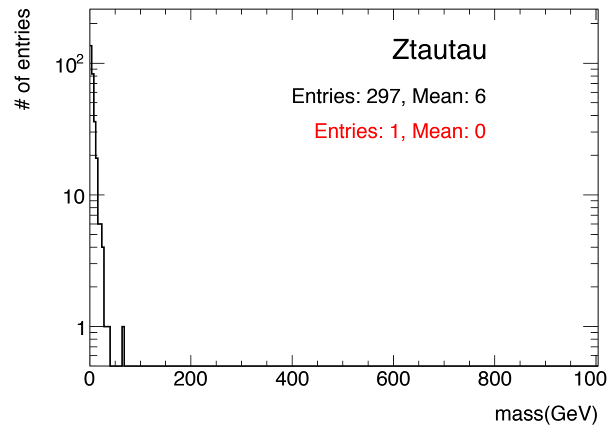

(b) tau (E_T 5 GeV) RoIs

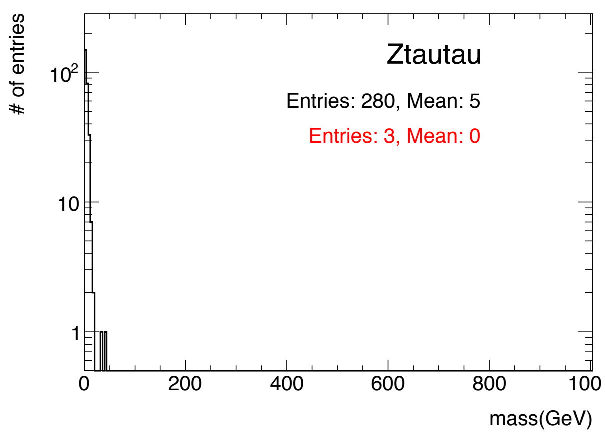

(c) muon (p_T 20 GeV) RoI

Figure 5.31: *Mass distribution of particles in $Z \rightarrow \tau\tau$ events surviving L2 selection in the Tile Calorimeter and having a matching ID track. The three distribution were based on seeding the chain with different regions of interest based on (a) single jet wiht E_T 5 GeV, (b) single τ with E_T 5 GeV and (c) single μ with p_T 20 GeV. The distributions marked* red *result from setting a upper cut of 100 GeV on the mass variable obtained from combining the β-estimate and the ID momentum estimate, as described in Section 4.4.*

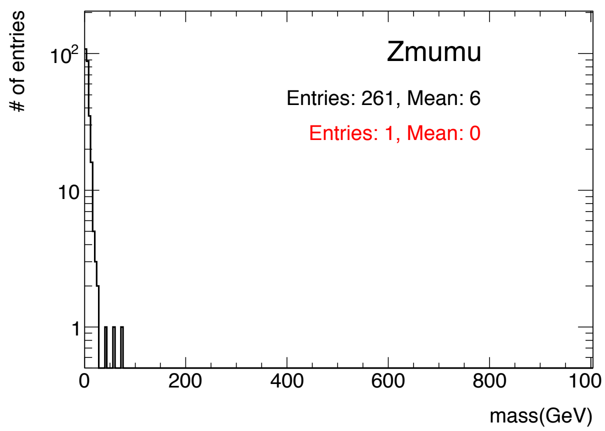

(a) jet (E_T 5 GeV) RoIs

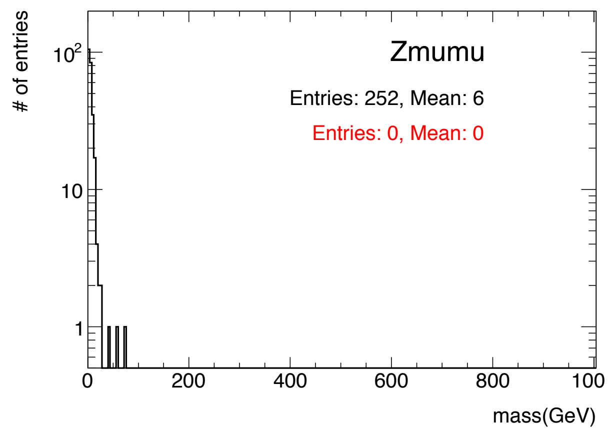

(b) tau (E_T 5 GeV) RoIs

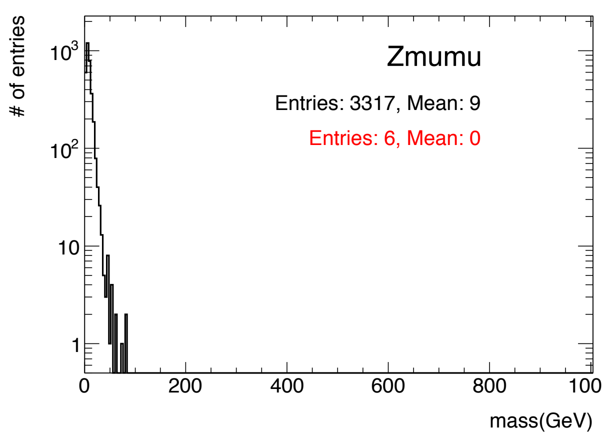

(c) muon (p_T 20 GeV) RoI

Figure 5.32: *Mass distribution of particles in $Z \rightarrow \mu\mu$ events surviving L2 selection in the Tile Calorimeter and having a matching ID track. The three distribution were based on seeding the chain with different regions of interest based on (a) single jet wiht E_T 5 GeV, (b) single τ with E_T 5 GeV and (c) single μ with p_T 20 GeV. The distributions marked* red *result from setting a upper cut of 100 GeV on the mass variable obtained from combining the β-estimate and the ID momentum estimate, as described in Section 4.4.*

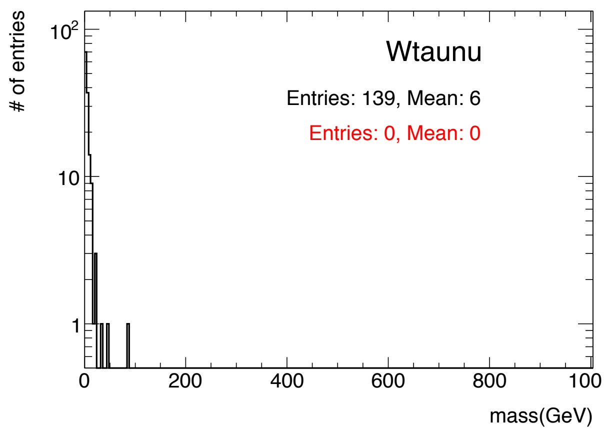

(a) jet (E_T 5 GeV) RoIs

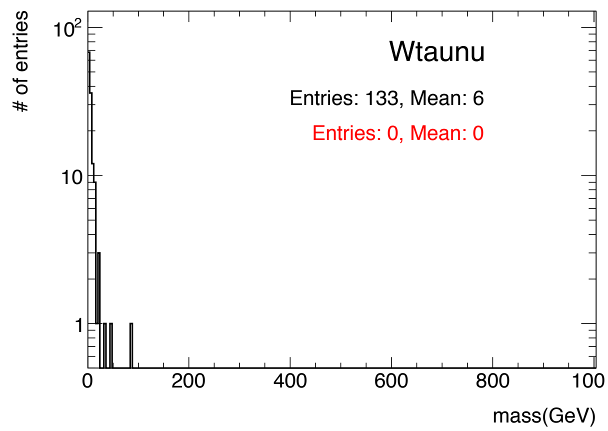

(b) tau (E_T 5 GeV) RoIs

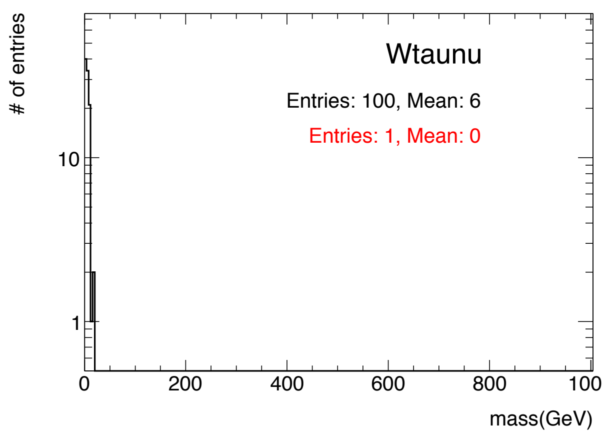

(c) muon (p_T 20 GeV) RoI

Figure 5.33: *Mass distribution of particles in $W \rightarrow \tau\nu$ events surviving L2 selection in the Tile Calorimeter and having a matching ID track. The three distribution were based on seeding the chain with different regions of interest based on (a) single jet wiht E_T 5 GeV, (b) single τ with E_T 5 GeV and (c) single μ with p_T 20 GeV. The distributions marked* red *result from setting a upper cut of 100 GeV on the mass variable obtained from combining the β-estimate and the ID momentum estimate, as described in Section 4.4.*

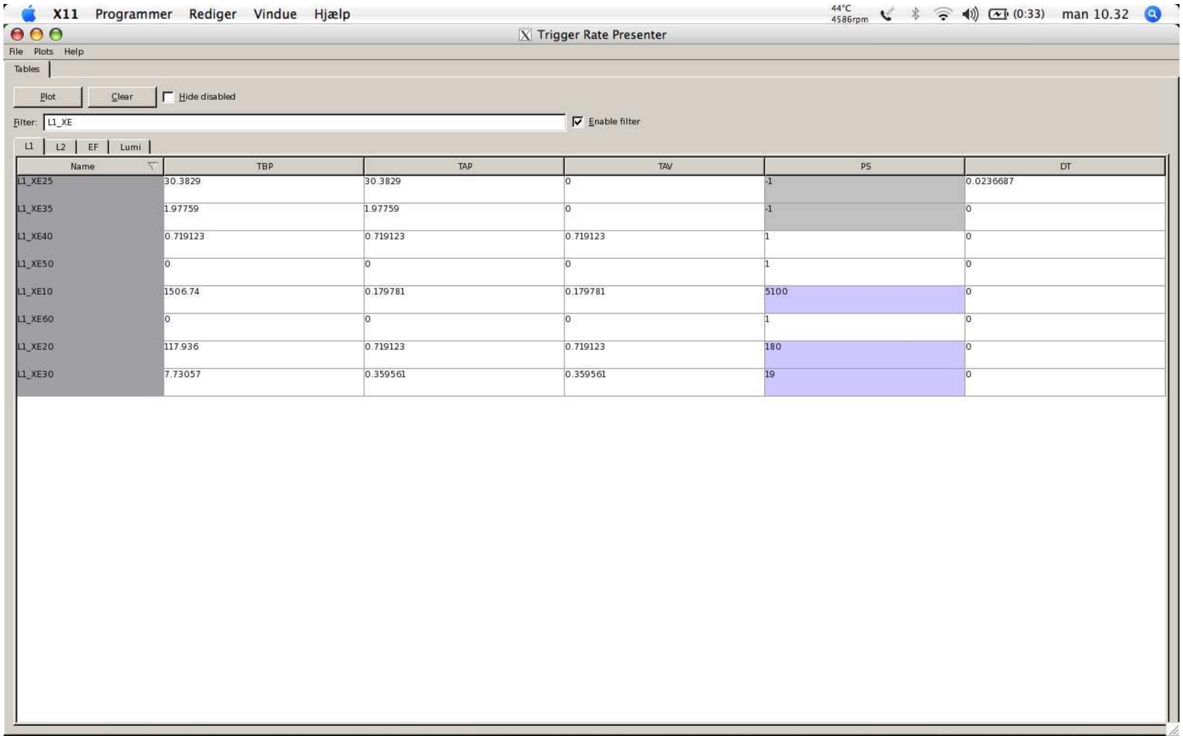

Figure 5.34: *Run rates and prescales of L1 J trigger items for run 177540*

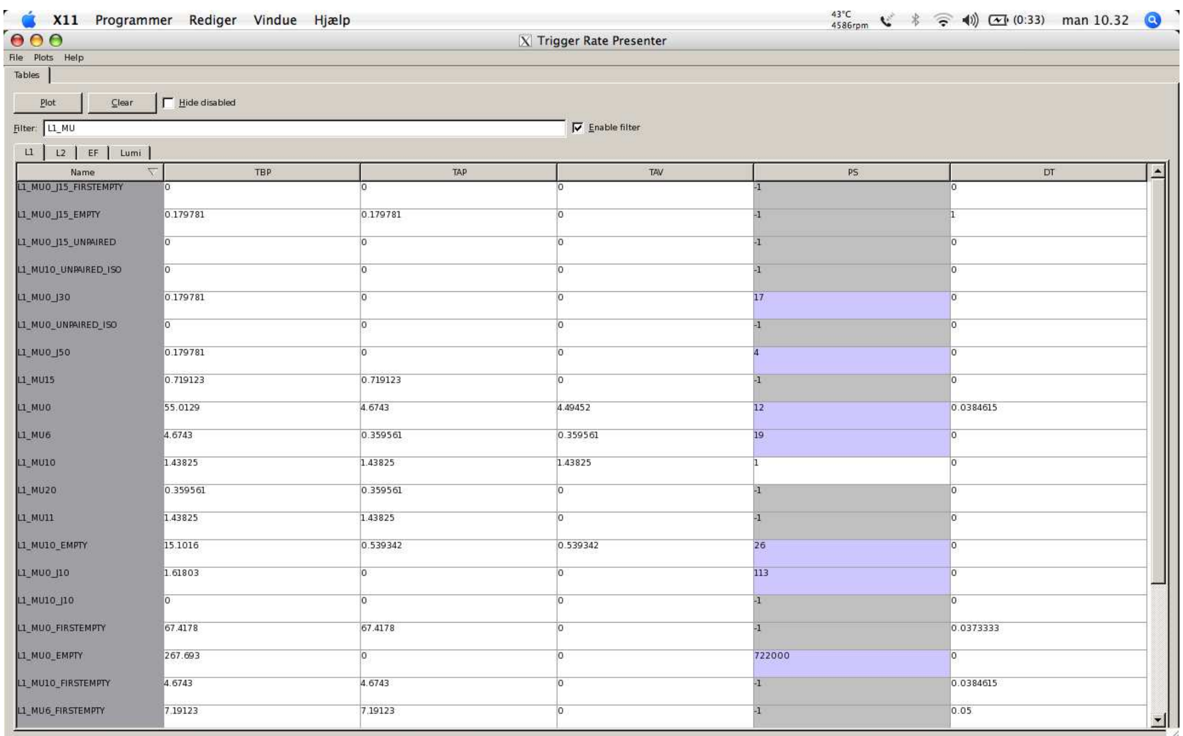

Figure 5.35: *Run rates and precales of L1 XE trigger items for run 177540*

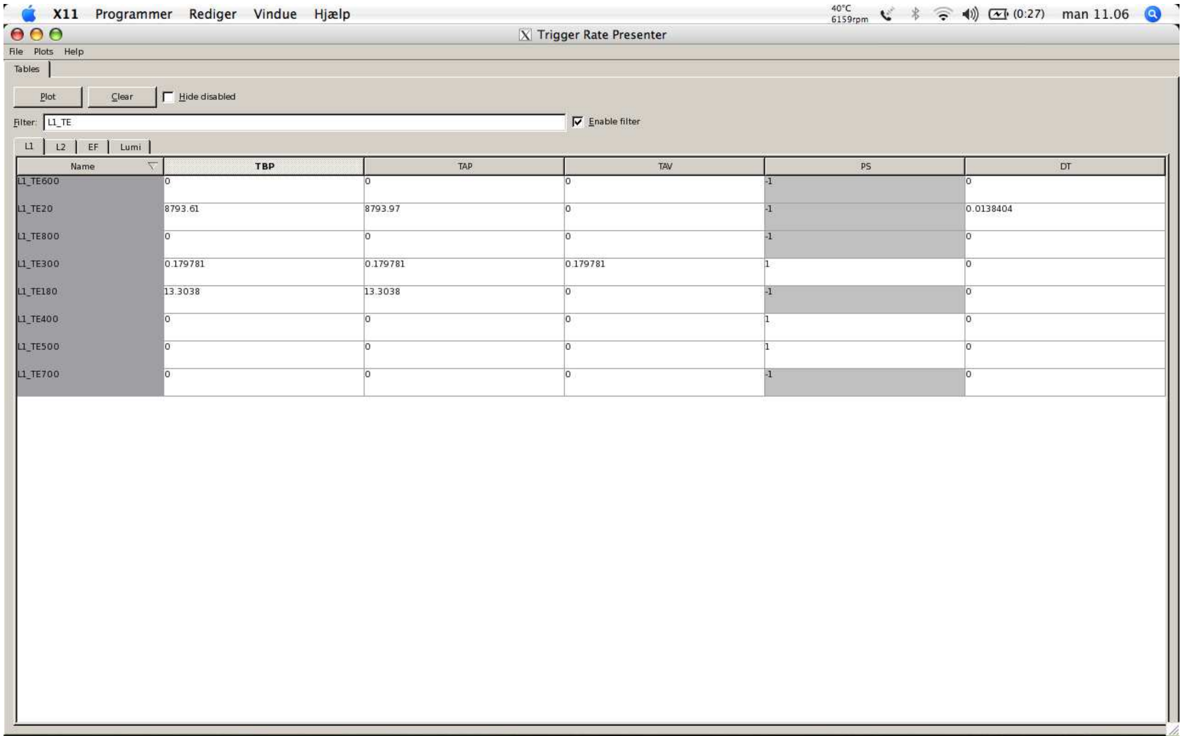

Name	TBP	TAP	TAV	PS	DT
L1_TE600	0	0	0	-1	0
L1_TE20	8793.61	8793.97	0	-1	0.0138404
L1_TE800	0	0	0	-1	0
L1_TE300	0.179781	0.179781	0.179781	1	0
L1_TE180	13.3038	13.3038	0	-1	0
L1_TE400	0	0	0	1	0
L1_TE500	0	0	0	1	0
L1_TE700	0	0	0	-1	0

Figure 5.36: *Run rates of and prescales of L1 MU trigger items for run 177540*

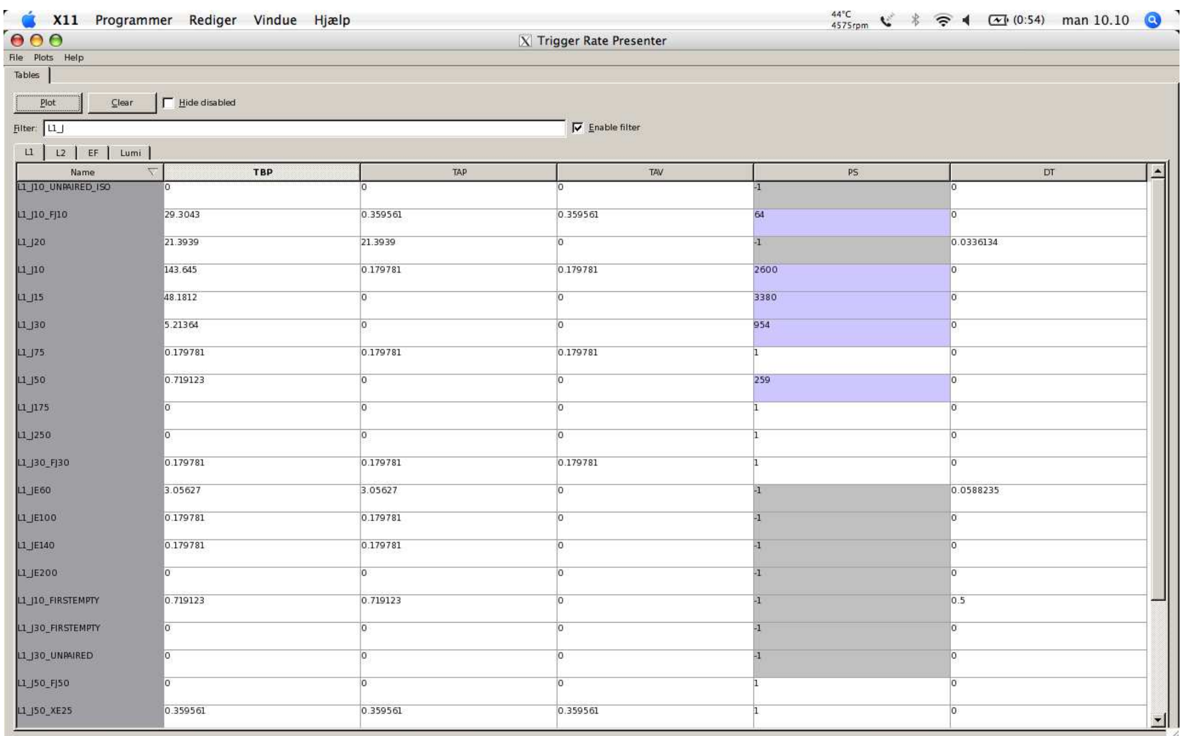

Name	TBP	TAP	TAV	PS	DT
L1_J10_UNPAIRED_ISO	0	0	0	-1	0
L1_J10_FJ10	29.3043	0.359561	0.359561	64	0
L1_J20	21.3939	21.3939	0	-1	0.0336134
L1_J10	143.645	0.179781	0.179781	2600	0
L1_J15	48.1812	0	0	3380	0
L1_J30	5.21364	0	0	954	0
L1_J75	0.179781	0.179781	0.179781	1	0
L1_J50	0.719123	0	0	259	0
L1_J175	0	0	0	1	0
L1_J250	0	0	0	1	0
L1_J30_FJ30	0.179781	0.179781	0.179781	1	0
L1_JE60	3.05627	3.05627	0	-1	0.0588235
L1_JE100	0.179781	0.179781	0	-1	0
L1_JE140	0.179781	0.179781	0	-1	0
L1_JE200	0	0	0	-1	0
L1_J10_FIRSTEMPTY	0.719123	0.719123	0	-1	0.5
L1_J30_FIRSTEMPTY	0	0	0	-1	0
L1_J30_UNPAIRED	0	0	0	-1	0
L1_J50_FJ50	0	0	0	1	0
L1_J50_XE25	0.359561	0.359561	0.359561	1	0

Figure 5.37: *Run rates and prescales of L1 TE trigger items for run 177540*

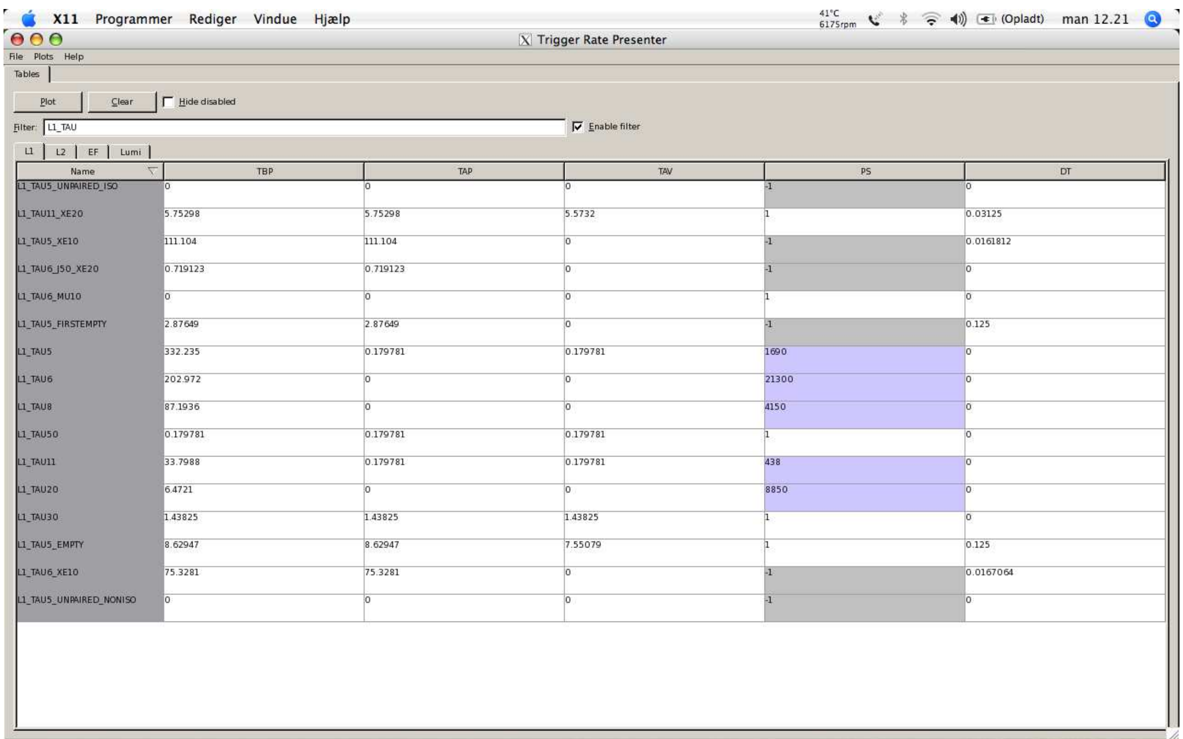

Name	TBP	TAP	TAV	PS	DT
L1_TAU5_UNPAIRED_ISO	0	0	0	-1	0
L1_TAU11_XE20	5.75298	5.75298	5.5732	1	0.03125
L1_TAU5_XE10	111.104	111.104	0	-1	0.0161812
L1_TAU6_J50_XE20	0.719123	0.719123	0	-1	0
L1_TAU6_MU10	0	0	0	1	0
L1_TAU5_FIRSTEMPTY	2.87649	2.87649	0	-1	0.125
L1_TAU5	332.235	0.179781	0.179781	1690	0
L1_TAU6	202.972	0	0	21300	0
L1_TAU8	87.1936	0	0	4150	0
L1_TAU50	0.179781	0.179781	0.179781	1	0
L1_TAU11	33.7988	0.179781	0.179781	438	0
L1_TAU20	6.4721	0	0	8850	0
L1_TAU30	1.43825	1.43825	1.43825	1	0
L1_TAU5_EMPTY	8.62947	8.62947	7.55079	1	0.125
L1_TAU6_XE10	75.3281	75.3281	0	-1	0.0167064
L1_TAU5_UNPAIRED_NONISO	0	0	0	-1	0

Figure 5.38: *Run rates and prescales of L1 TAU trigger items for run 177540*

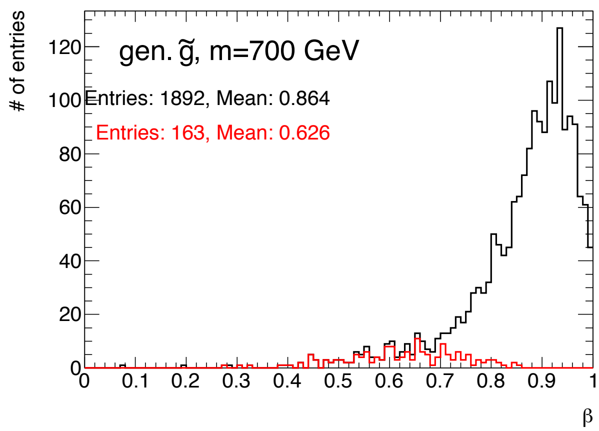

(a) jet (E_T 5 GeV) RoIs

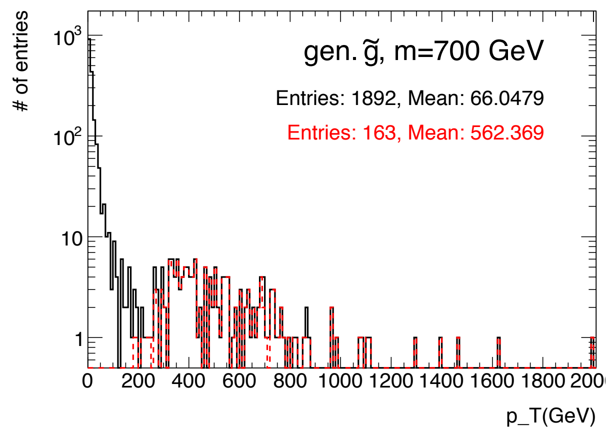

(b) jet (E_T 5 GeV) RoIs

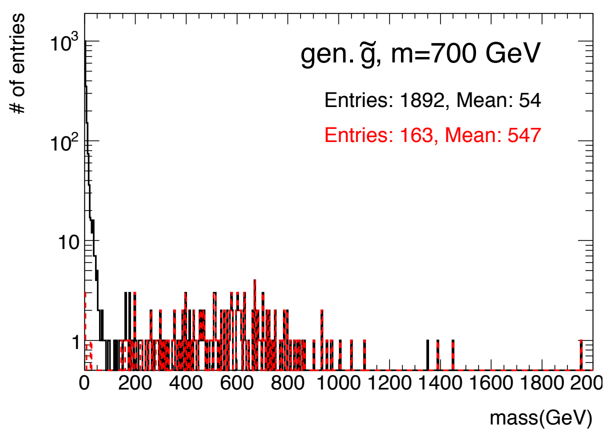

(c) jet (E_T 5 GeV) RoIs

Figure 5.39: *Perfomance of L2 SMP chain with L1XE20 with J5 (single jet, E_T 5 GeV) RoIs for $\tilde{g}$ of 700 GeV with the generic interaction model and with candidates from truth matched RoIs shown marked red.*

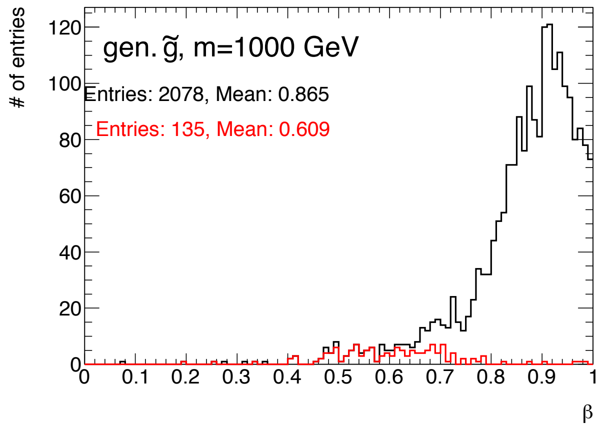

(a) jet (E_T 5 GeV) RoIs

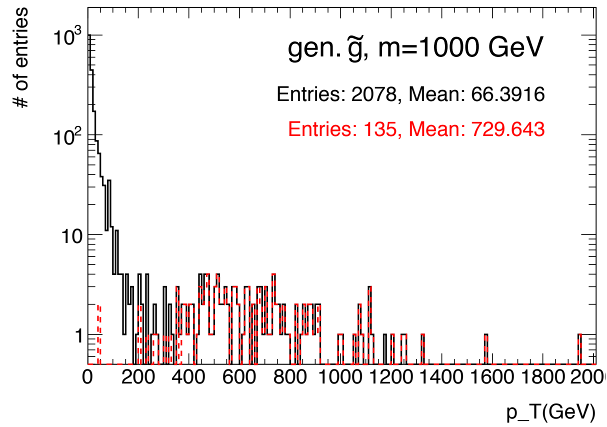

(b) jet (E_T 5 GeV) RoIs

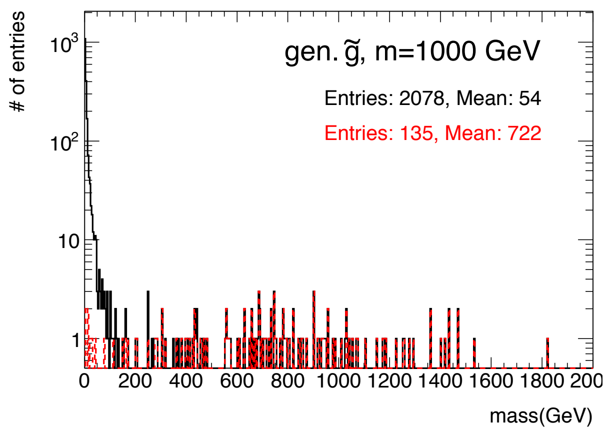

(c) jet (E_T 5 GeV) RoIs

Figure 5.40: *Perfomance of L2 SMP chain with L1XE20 with J5 (single jet, E_T 5 GeV) RoIs for $\tilde{g}$ of 1000 GeV with the generic interaction model and with candidates from truth matched RoIs shown marked red.*

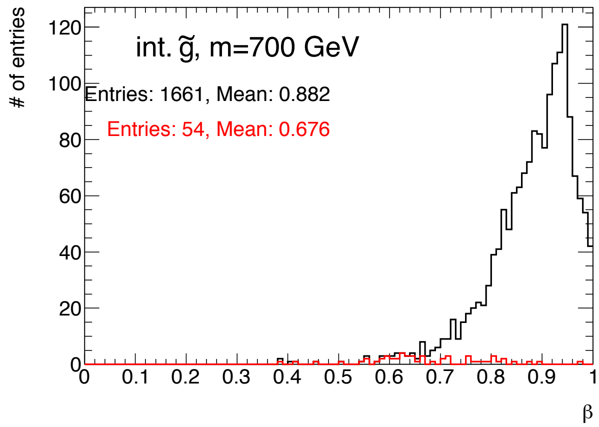

(a) jet (E_T 5 GeV) RoIs

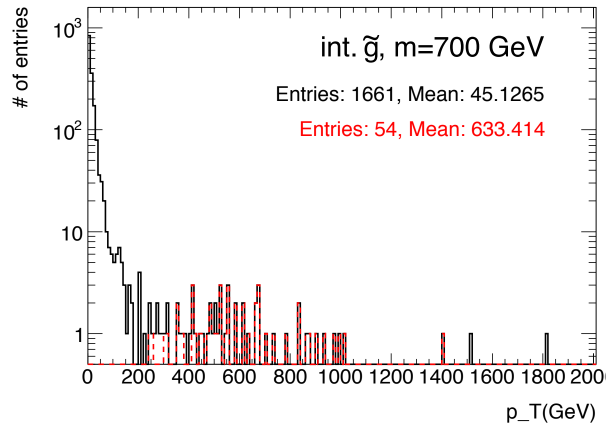

(b) jet (E_T 5 GeV) RoIs

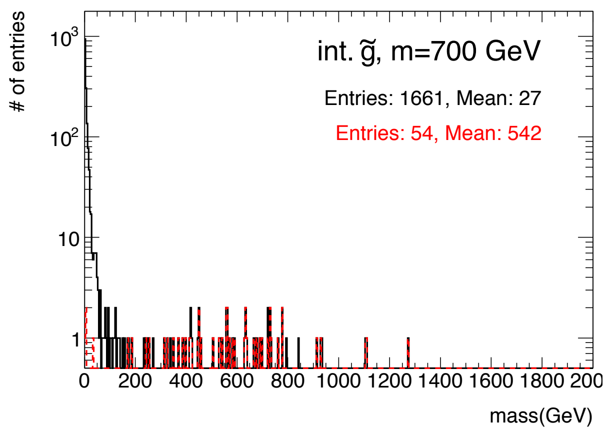

(c) jet (E_T 5 GeV) RoIs

Figure 5.41: *Perfomance of L2 SMP chain with L1XE20 with J5 (single jet, E_T 5 GeV) RoIs for $\tilde{g}$ of 700 GeV with the intermediate interaction model and with candidates from truth matched RoIs shown marked red.*

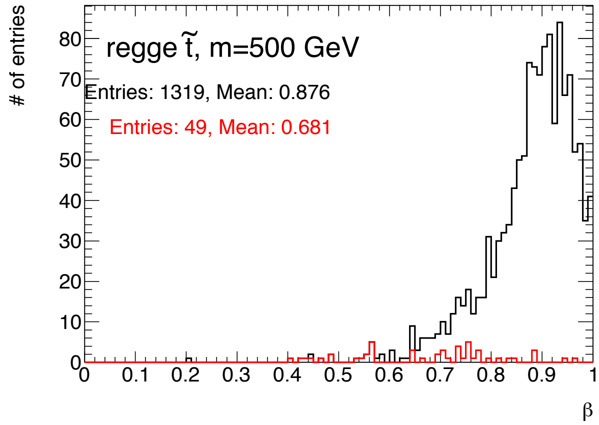

(a) jet (E_T 5 GeV) RoIs

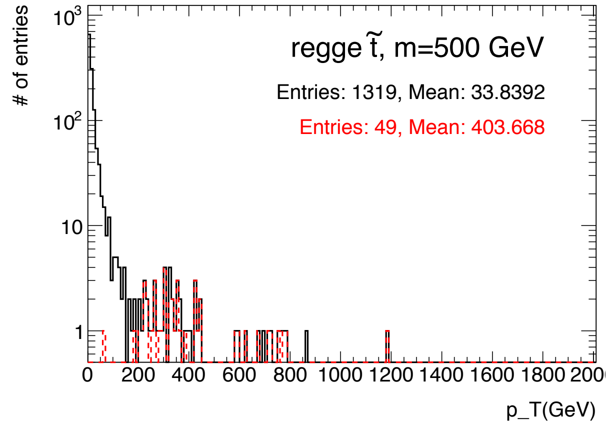

(b) jet (E_T 5 GeV) RoIs

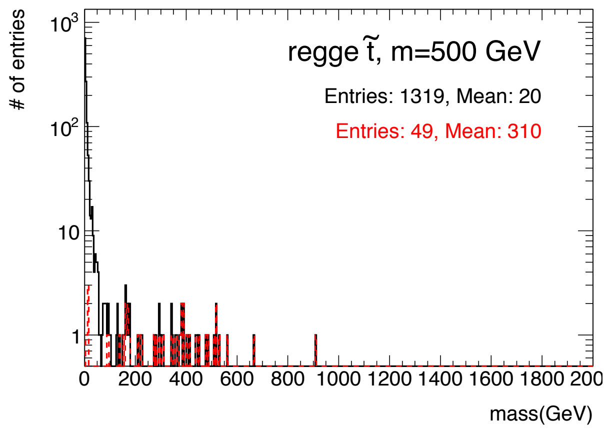

(c) jet (E_T 5 GeV) RoIs

Figure 5.42: *Perfomance of L2 SMP chain with L1XE20 with J5 (single jet, E_T 5 GeV) RoIs for $\tilde{t}$ of 500 GeV with the intermediate interaction model and with candidates from truth matched RoIs shown marked red.*

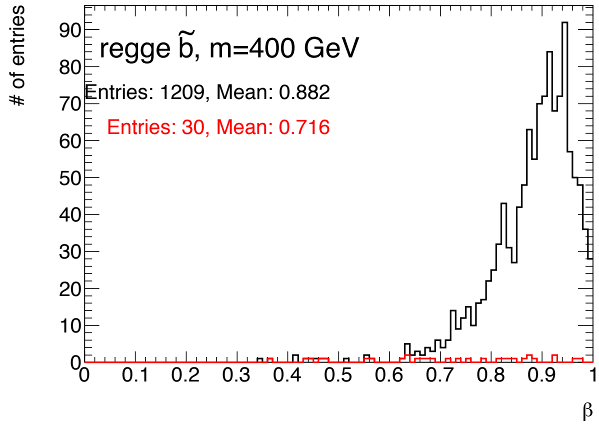

(a) jet (E_T 5 GeV) RoIs

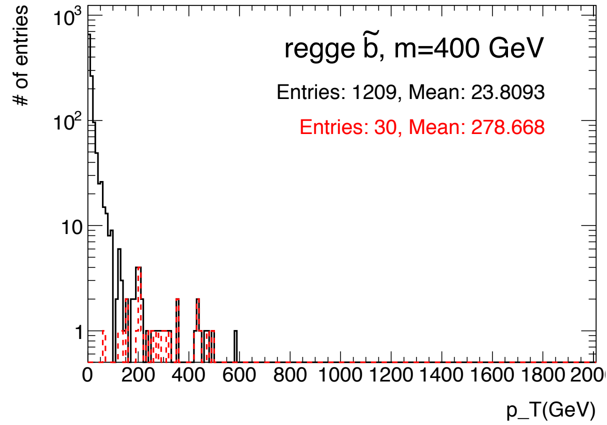

(b) jet (E_T 5 GeV) RoIs

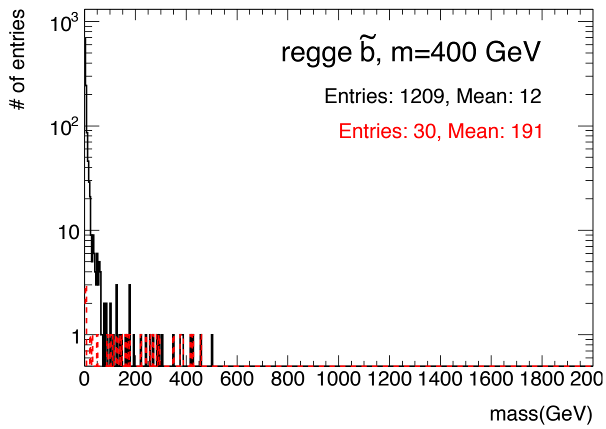

(c) jet (E_T 5 GeV) RoIs

Figure 5.43: *Perfomance of L2 SMP chain with L1XE20 with J5 (single jet, E_T 5 GeV) RoIs for $\tilde{t}$ of 400 GeV with the intermediate interaction model and with candidates from truth matched RoIs shown marked red.*

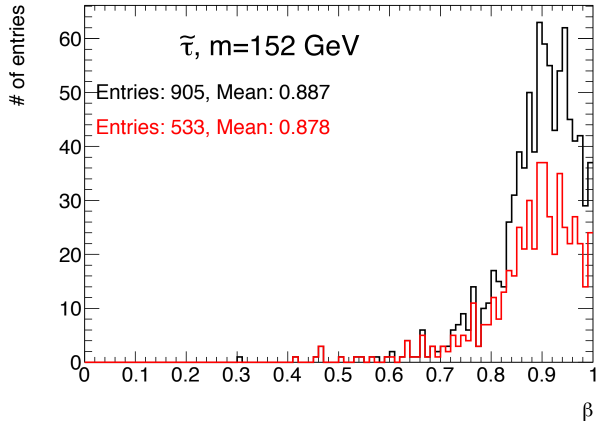

(a) jet (E_T 5 GeV) RoIs

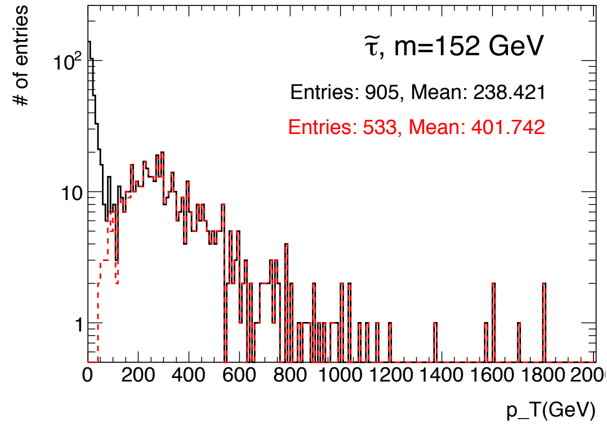

(b) jet (E_T 5 GeV) RoIs

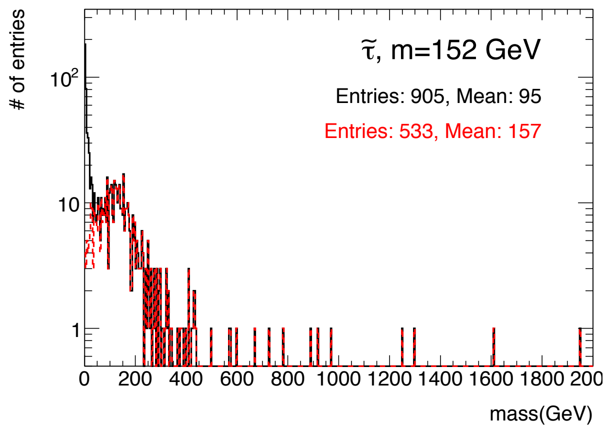

(c) jet (E_T 5 GeV) RoIs

Figure 5.44: *Perfomance of L2 SMP chain with L1XE20 with J5 (single jet, E_T 5 GeV) RoIs for $\tilde{t}$ of 400 GeV with the intermediate interaction model and with candidates from truth matched RoIs shown marked red.*

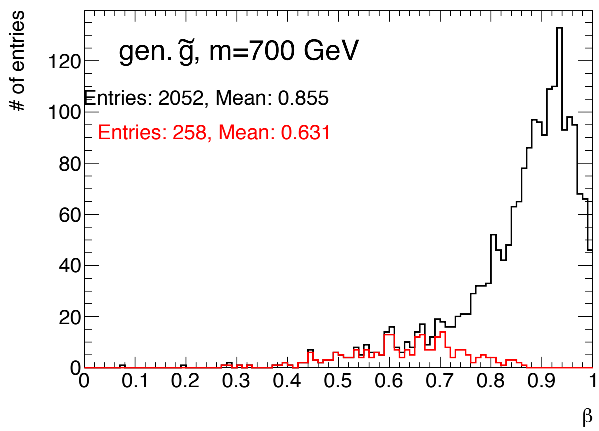

(a) jet (E_T 5 GeV) RoIs

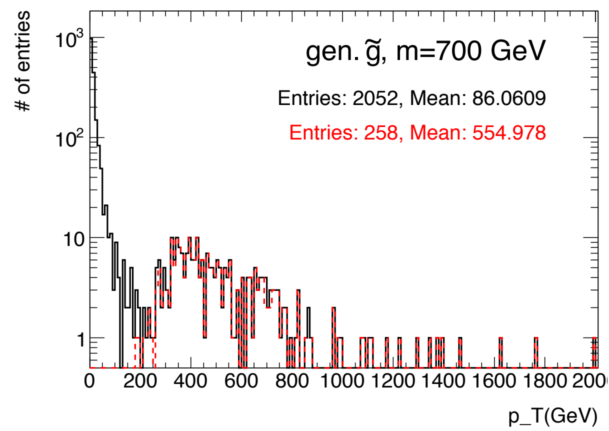

(b) jet (E_T 5 GeV) RoIs

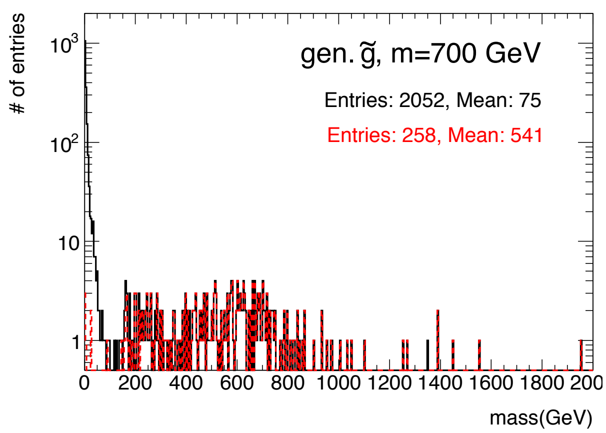

(c) jet (E_T 5 GeV) RoIs

Figure 5.45: *Perfomance of L2 SMP chain with L1TAU5 with J5 (single jet, E_T 5 GeV) RoIs for $\tilde{g}$ of 700 GeV with the generic interaction model and with candidates from truth matched RoIs shown marked red.*

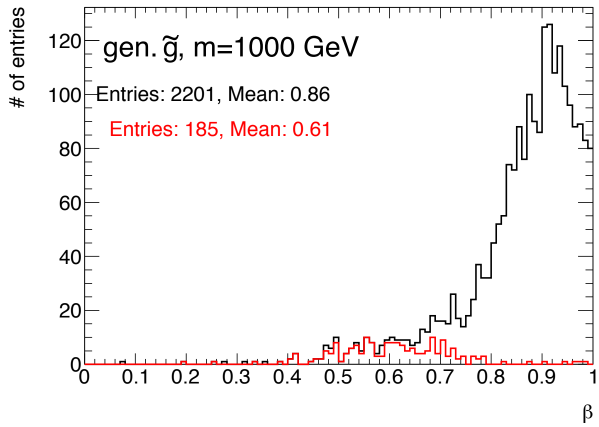

(a) jet (E_T 5 GeV) RoIs

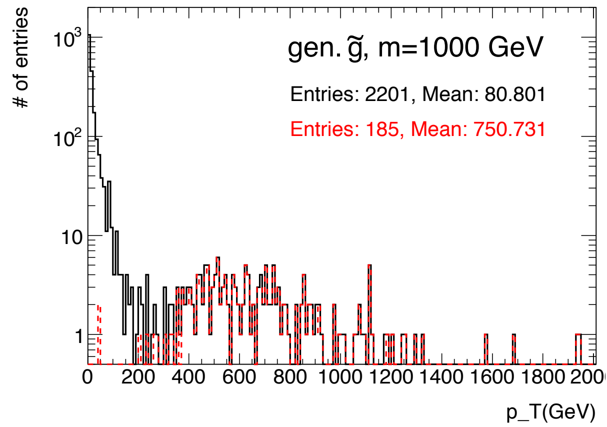

(b) jet (E_T 5 GeV) RoIs

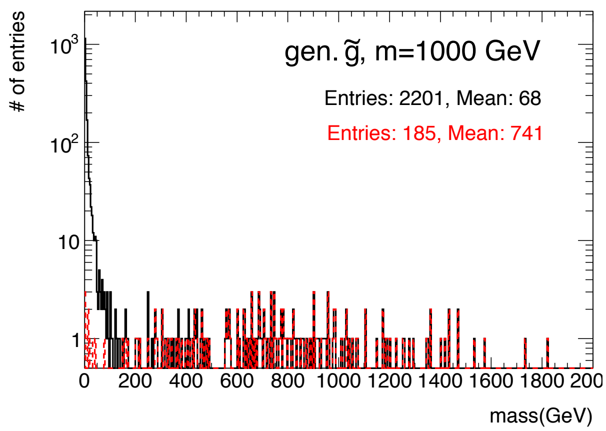

(c) jet (E_T 5 GeV) RoIs

Figure 5.46: *Perfomance of L2 SMP chain with L1TAU5 with J5 (single jet, E_T 5 GeV) RoIs for $\tilde{g}$ of 1000 GeV with the generic interaction model and with candidates from truth matched RoIs shown marked red.*

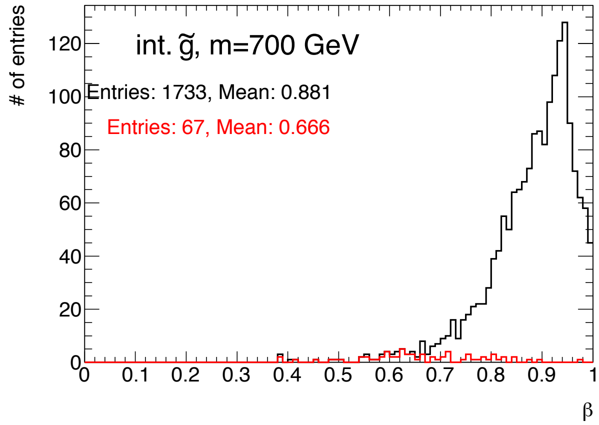

(a) jet (E_T 5 GeV) RoIs

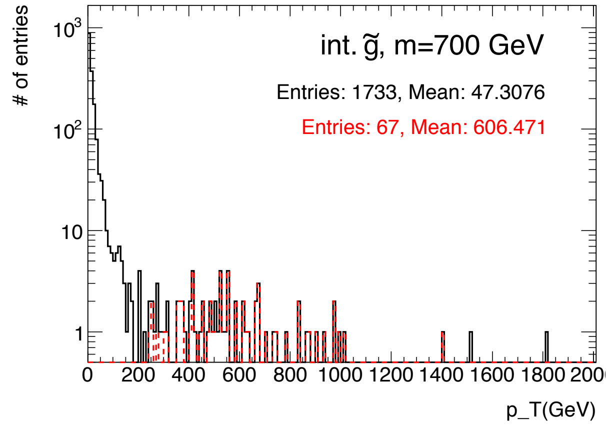

(b) jet (E_T 5 GeV) RoIs

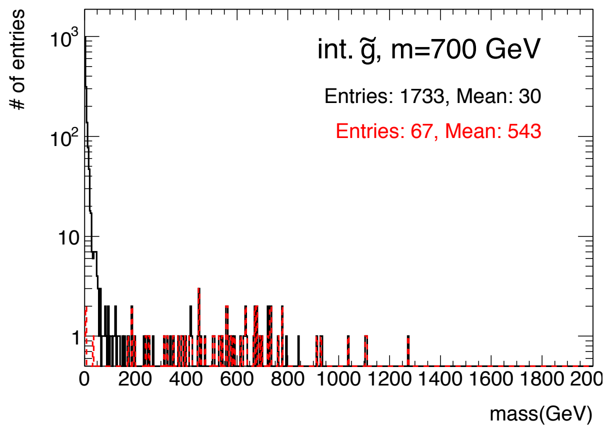

(c) jet (E_T 5 GeV) RoIs

Figure 5.47: *Perfomance of L2 SMP chain with L1TAU5 with J5 (single jet, E_T 5 GeV) RoIs for $\tilde{g}$ of 700 GeV with the intermediate interaction model and with candidates from truth matched RoIs shown marked red.*

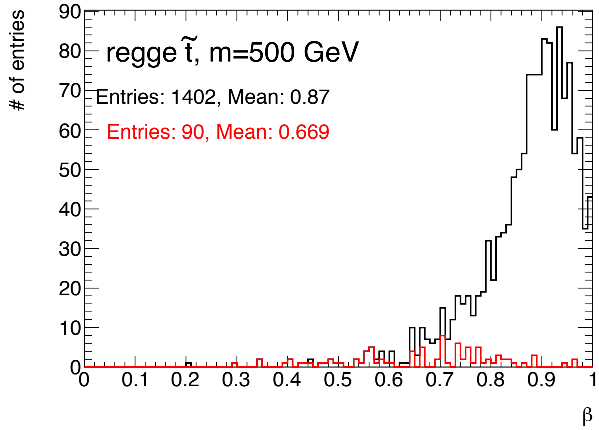

(a) jet (E_T 5 GeV) RoIs

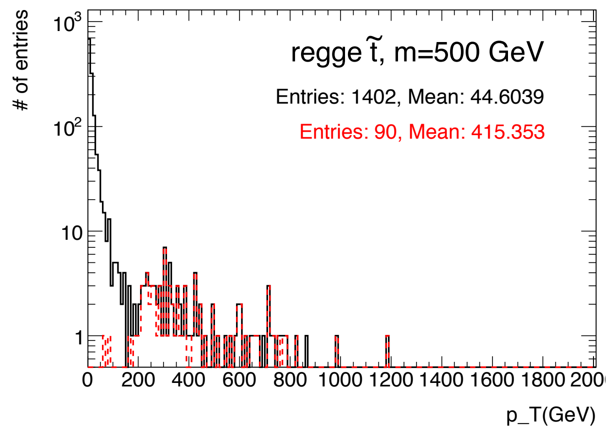

(b) jet (E_T 5 GeV) RoIs

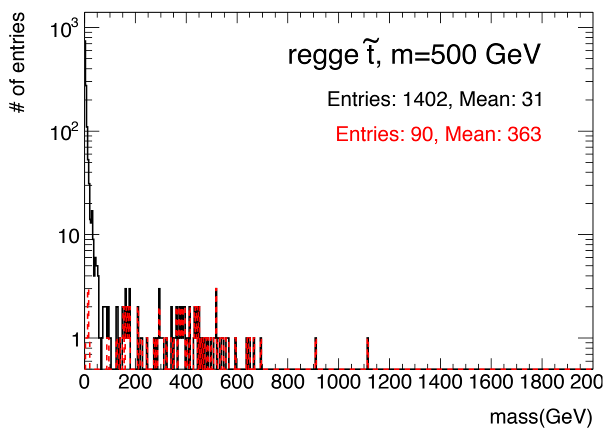

(c) jet (E_T 5 GeV) RoIs

Figure 5.48: *Perfomance of L2 SMP chain with L1TAU5 with J5 (single jet, E_T 5 GeV) RoIs for $\tilde{t}$ of 500 GeV with the intermediate interaction model and with candidates from truth matched RoIs shown marked red.*

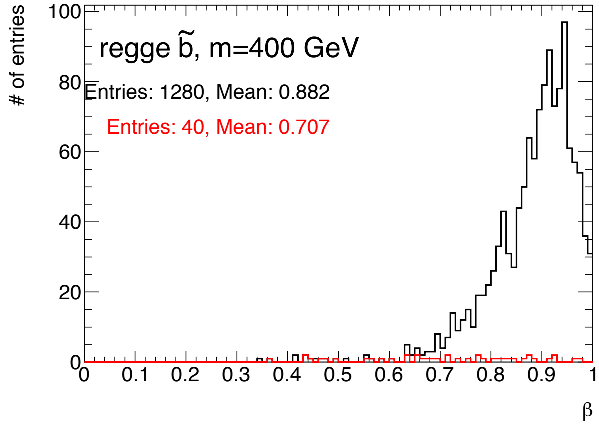

(a) jet (E_T 5 GeV) RoIs

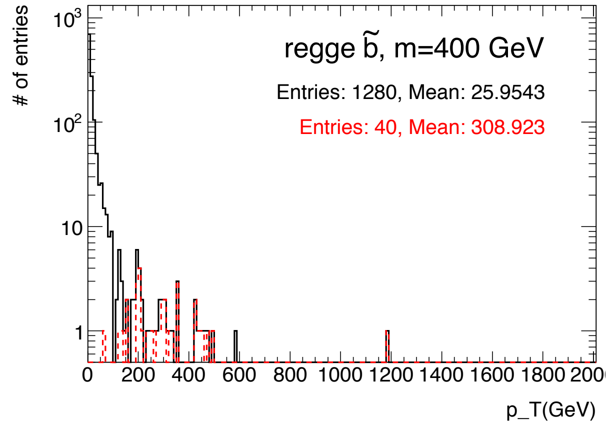

(b) jet (E_T 5 GeV) RoIs

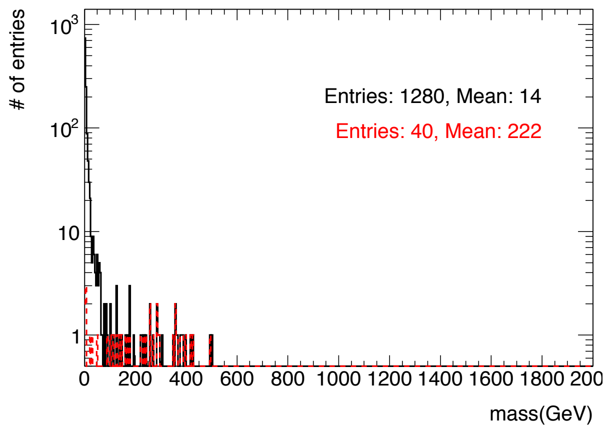

(c) jet (E_T 5 GeV) RoIs

Figure 5.49: *Perfomance of L2 SMP chain with L1TAU5 with J5 (single jet, E_T 5 GeV) RoIs for $\tilde{t}$ of 400 GeV with the intermediate interaction model and with candidates from truth matched RoIs shown marked red.*

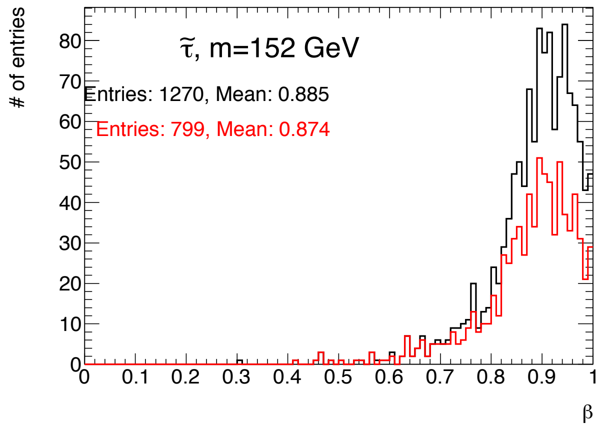

(a) jet (E_T 5 GeV) RoIs

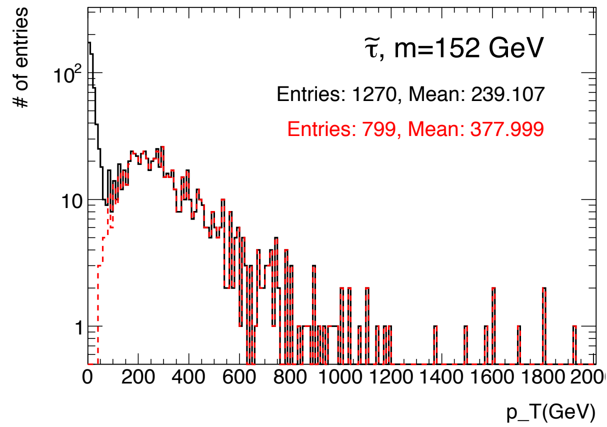

(b) jet (E_T 5 GeV) RoIs

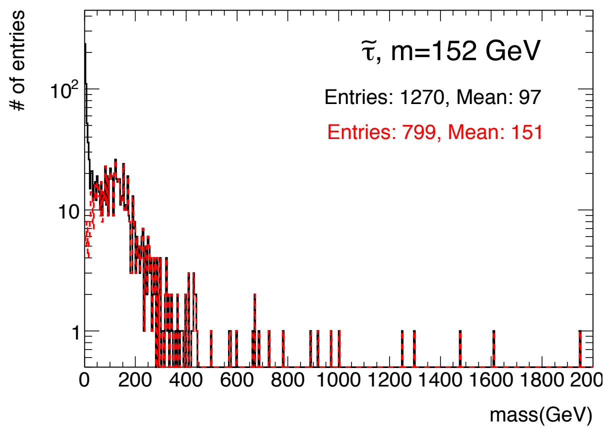

(c) jet (E_T 5 GeV) RoIs

Figure 5.50: *Perfomance of L2 SMP chain with L1TAU5 with J5 (single jet, E_T 5 GeV) RoIs for $\tilde{t}$ of 400 GeV with the intermediate interaction model and with candidates from truth matched RoIs shown marked red.*

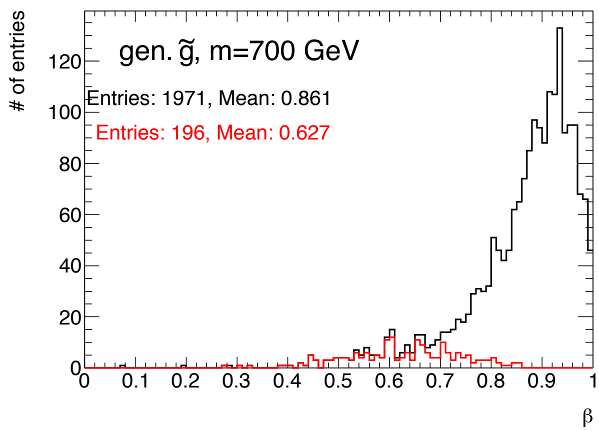

(a) jet (E_T 5 GeV) RoIs

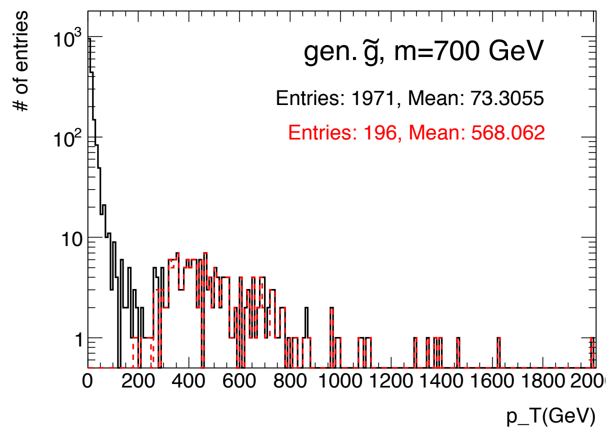

(b) jet (E_T 5 GeV) RoIs

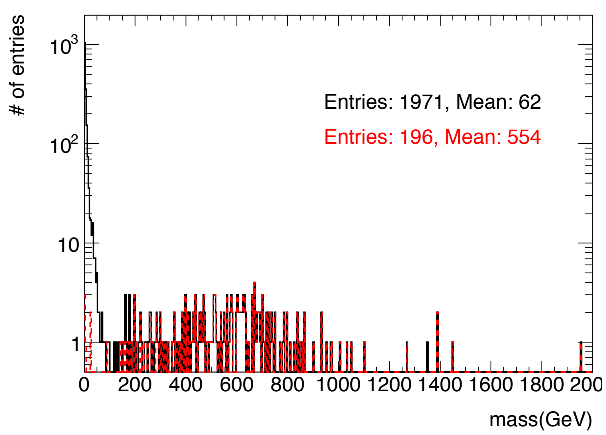

(c) jet (E_T 5 GeV) RoIs

Figure 5.51: *Perfomance of L2 SMP chain with L1TAUXE5 with J5 (single jet, E_T 5 GeV) RoIs for $\tilde{g}$ of 700 GeV with the generic interaction model and with candidates from truth matched RoIs shown marked red.*

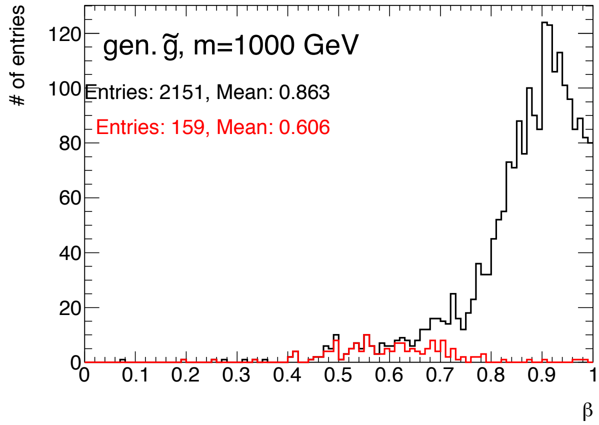

(a) jet (E_T 5 GeV) RoIs

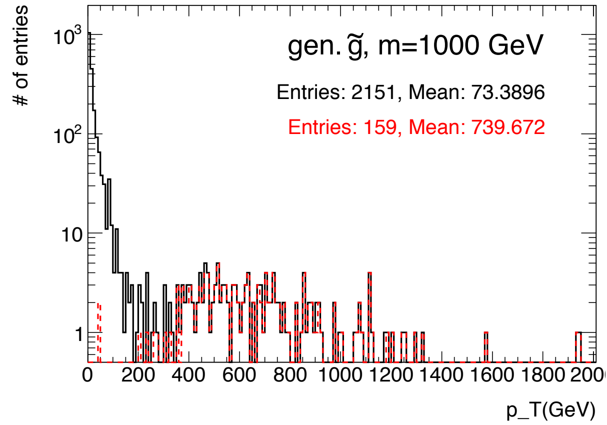

(b) jet (E_T 5 GeV) RoIs

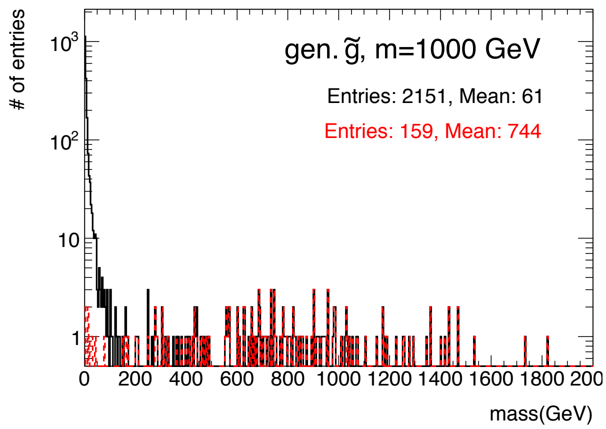

(c) jet (E_T 5 GeV) RoIs

Figure 5.52: *Perfomance of L2 SMP chain with L1TAUXE5 with J5 (single jet, E_T 5 GeV) RoIs for $\tilde{g}$ of 1000 GeV with the generic interaction model and with candidates from truth matched RoIs shown marked red.*

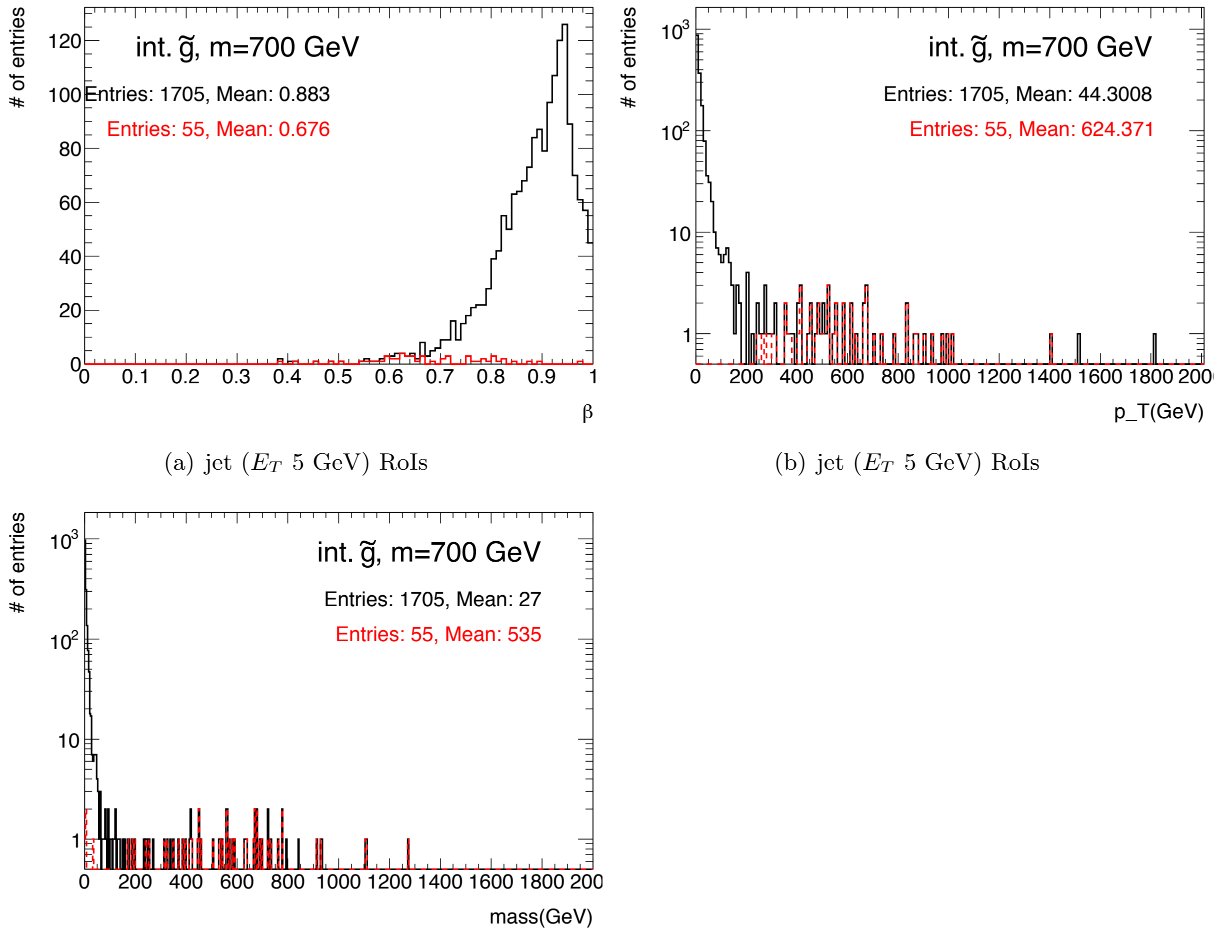

(a) jet (E_T 5 GeV) RoIs

(b) jet (E_T 5 GeV) RoIs

(c) jet (E_T 5 GeV) RoIs

Figure 5.53: *Perfomance of L2 SMP chain with L1TAUXE5 with J5 (single jet, E_T 5 GeV) RoIs for $\tilde{g}$ of 700 GeV with the intermediate interaction model and with candidates from truth matched RoIs shown marked red.*

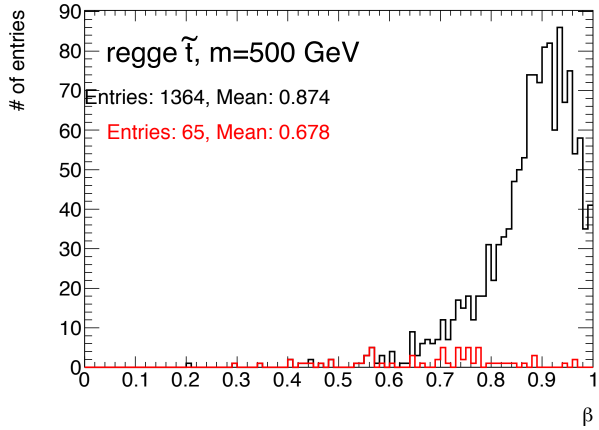

(a) jet (E_T 5 GeV) RoIs

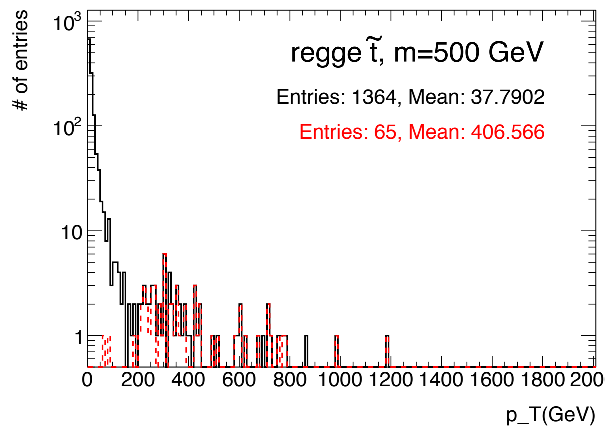

(b) jet (E_T 5 GeV) RoIs

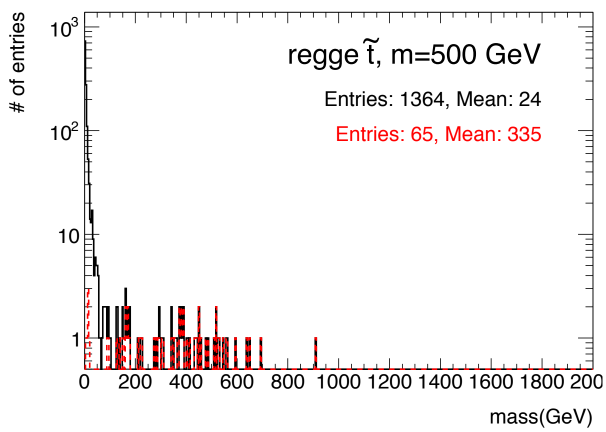

(c) jet (E_T 5 GeV) RoIs

Figure 5.54: *Perfomance of L2 SMP chain with L1TAUXE5 with J5 (single jet, E_T 5 GeV) RoIs for $\tilde{t}$ of 500 GeV with the intermediate interaction model and with candidates from truth matched RoIs shown marked red.*

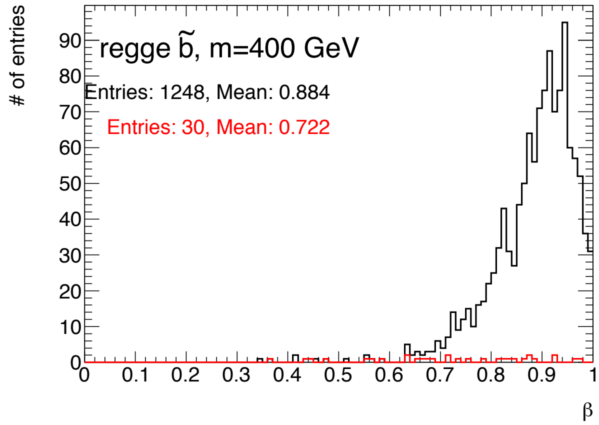

(a) jet (E_T 5 GeV) RoIs

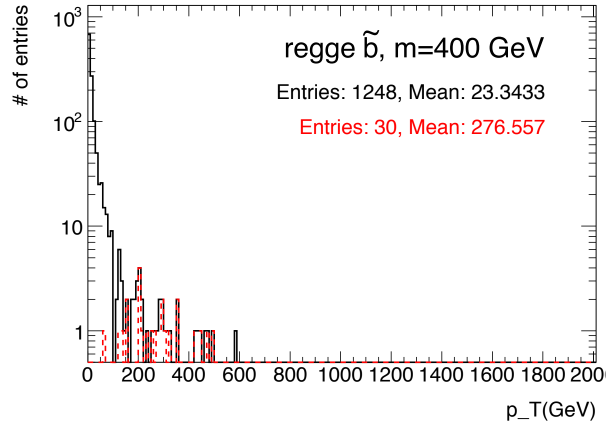

(b) jet (E_T 5 GeV) RoIs

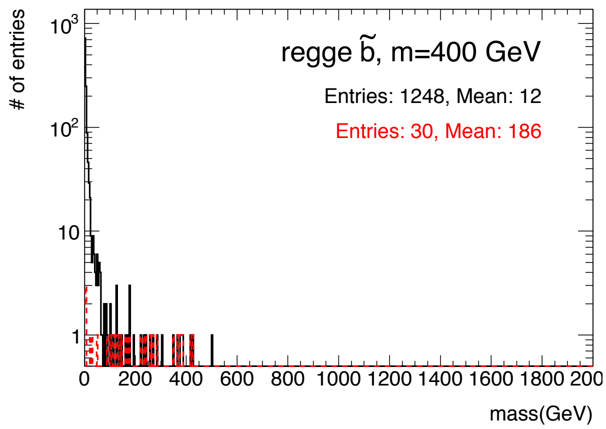

(c) jet (E_T 5 GeV) RoIs

Figure 5.55: *Perfomance of L2 SMP chain with L1TAUXE5 with J5 (single jet, E_T 5 GeV) RoIs for $\tilde{t}$ of 400 GeV with the intermediate interaction model and with candidates from truth matched RoIs shown marked red.*

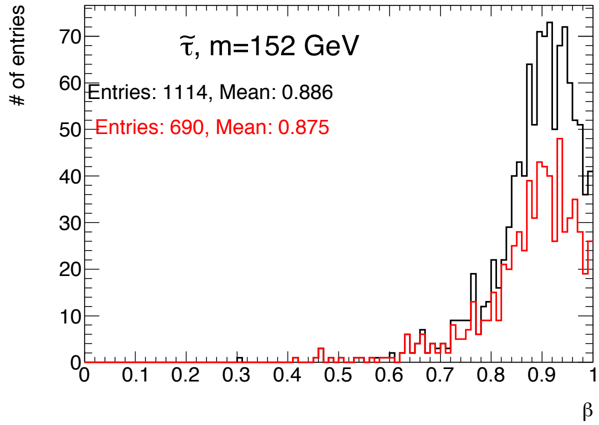

(a) jet (E_T 5 GeV) RoIs

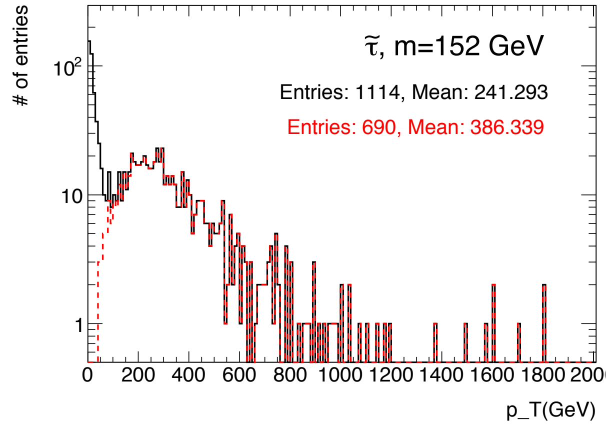

(b) jet (E_T 5 GeV) RoIs

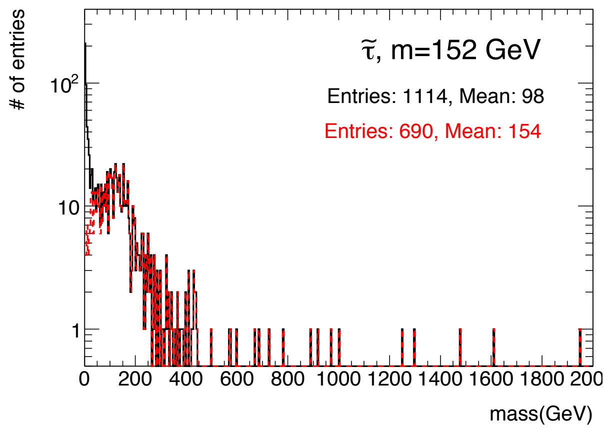

(c) jet (E_T 5 GeV) RoIs

Figure 5.56: *Perfomance of L2 SMP chain with L1TAUXE with J5 (single jet, E_T 5 GeV) RoIs for $\tilde{t}$ of 400 GeV with the intermediate interaction model and with candidates from truth matched RoIs shown marked red.*

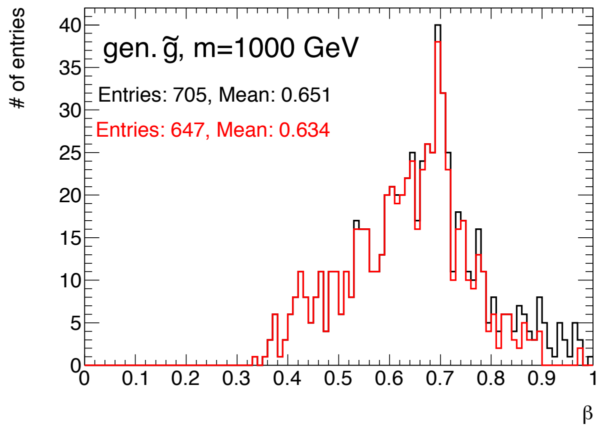

(a) jet (E_T 5 GeV) RoIs

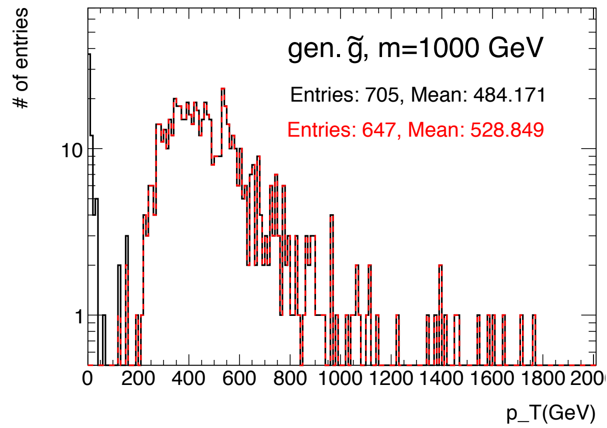

(b) jet (E_T 5 GeV) RoIs

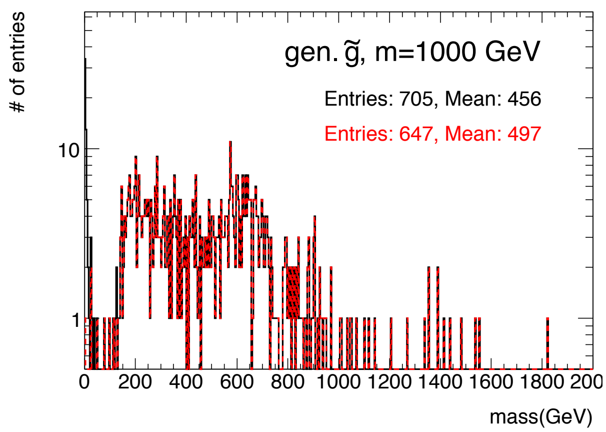

(c) jet (E_T 5 GeV) RoIs

Figure 5.57: *Perfomance of L2 SMP chain with L1MU20 with mu20 RoIs for $\tilde{g}$ of 700 GeV with the generic interaction model and with candidates from truth matched RoIs shown marked red.*

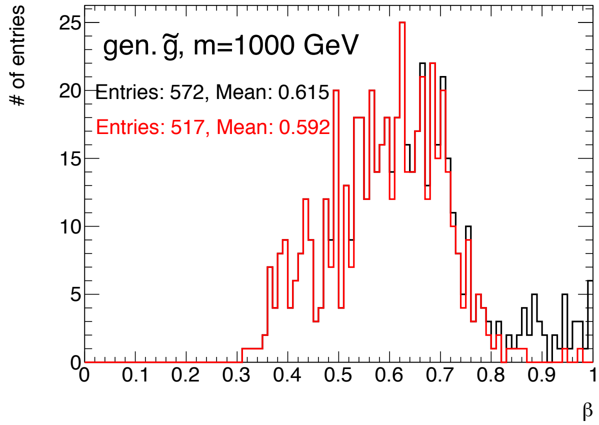

(a) jet (E_T 5 GeV) RoIs

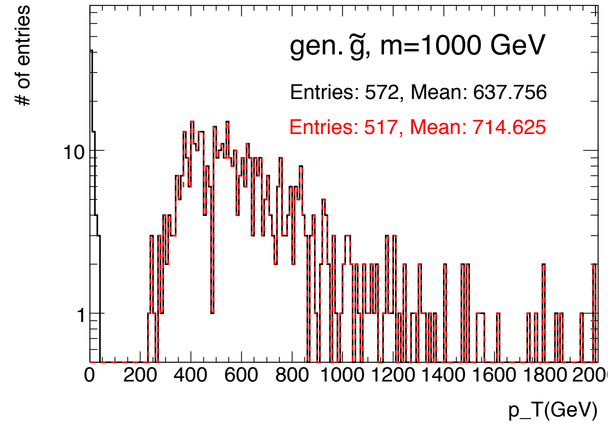

(b) jet (E_T 5 GeV) RoIs

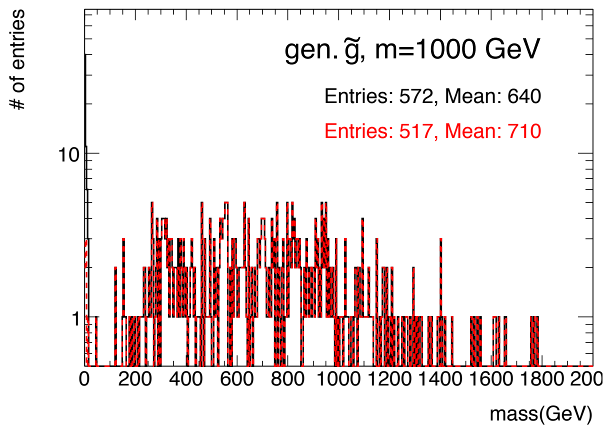

(c) jet (E_T 5 GeV) RoIs

Figure 5.58: *Perfomance of L2 SMP chain with L1MU20 with mu20 (single muon, p_T 20 GeV) RoIs for $\tilde{g}$ of 1000 GeV with the generic interaction model and with candidates from truth matched RoIs shown marked red.*

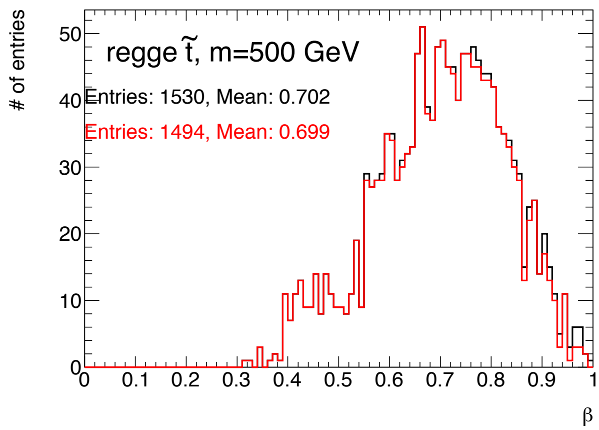

(a) jet (E_T 5 GeV) RoIs

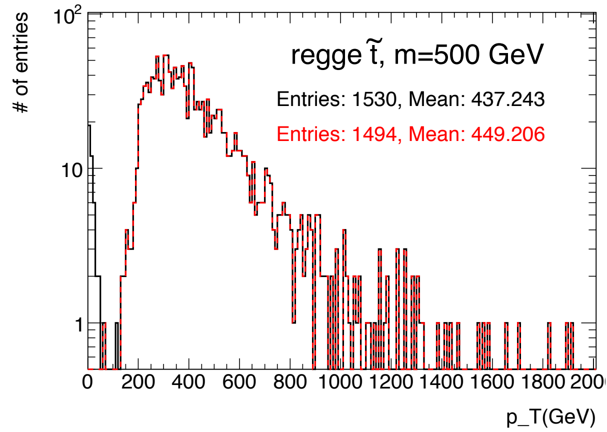

(b) jet (E_T 5 GeV) RoIs

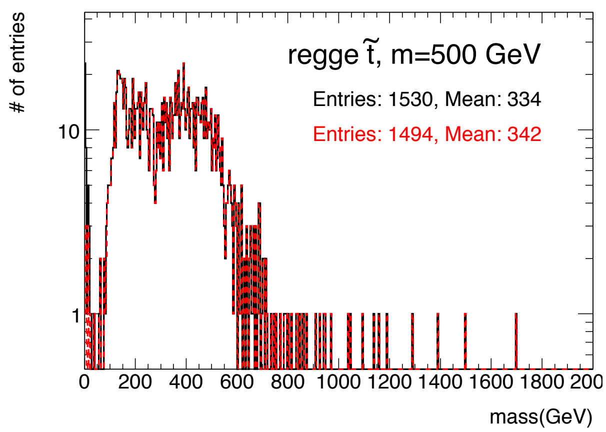

(c) jet (E_T 5 GeV) RoIs

Figure 5.59: *Perfomance of L2 SMP chain with L1MU20 with mu20 (single muon, p_T 20 GeV) RoIs for $\tilde{t}$ of 500 GeV with the intermediate interaction model and with candidates from truth matched RoIs shown marked red.*

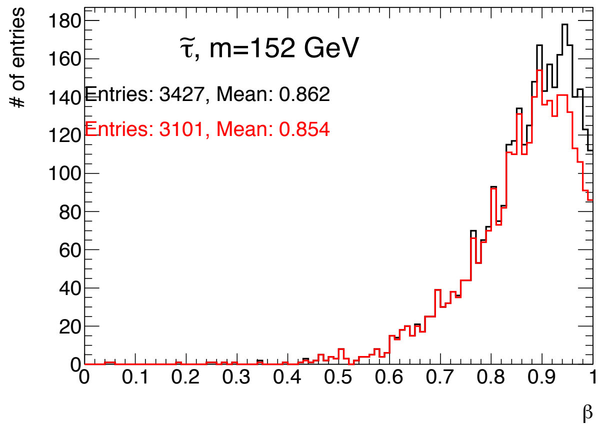

(a) jet (E_T 5 GeV) RoIs

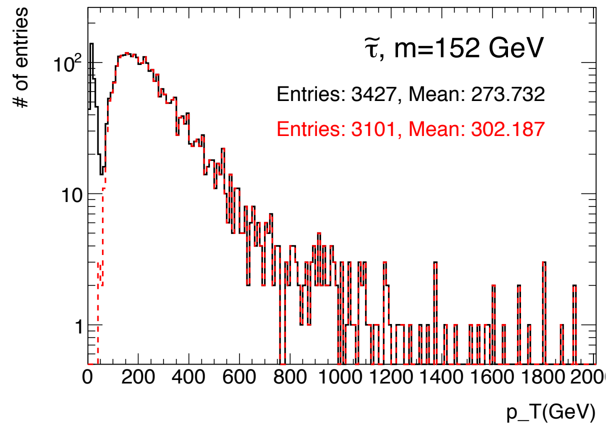

(b) jet (E_T 5 GeV) RoIs

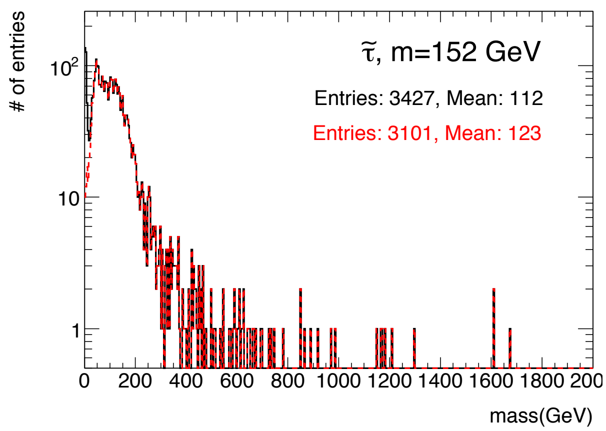

(c) jet (E_T 5 GeV) RoIs

Figure 5.60: *Perfomance of L2 SMP chain with L1MU20 with mu20 (single muon, p_T 20 GeV) RoIs for $\tilde{t}$ of 400 GeV with the intermediate interaction model and with candidates from truth matched RoIs shown marked red.*

Bibliography

[1] S.L. Glashow: *Partial-symmetries of weak interactions*,
Nuclear Physics, 1961.

[2] Donald H. Perkins: Introduction to High Energy Physics,
Cambridge University Press, 4th ed. 2000.

[3] Dieter Haidt: *The discovery of the weak neutral currents*,
Cern Courier Oct. 2004 `http://cerncourier.com/cws/article/cern/29168`

[4] G. Garnison et al.: *Experimental observation of isolated large transverse enery electrons with associated missing energy a* $\sqrt{s}$*=540 Gev*,
Physical Letters B122 1983.

[5] G. Garnison et al.: *Experimental observation of lepton pairs of invariant mass around 95 Gev at the CERN SPS collider*,
Physical Letters B126, 1983.

[6] P. Bagnaia et al.: *Evidence for* $Z_0 - > e + e-$ *at the CERN anti-p p collider*,
Physical Letters B129, 1983.

[7] M. Banner et al.:*Observation of single isolated electrons of high transverse momentum in events with missing transverse energy at the CERN anti-p p collider*,
Physical Letters B122 1983.

[8] Dan Green: *High Pt Physics at Hadron Colliders*,
Cambridge University Press, 2005.

[9] E. Peskin and D.Vs Schroeder: *An Introduction to Quantum Field Theory*,
Reading, USA, Addison-Wesley 1995.

[10] Christopher T. Hill, Elizabeth H. Simmons: *Strong Dynamics and Electroweak Symmetry Breaking*
`http://arxiv.org/abs/hep-ph/0203079`, March 2002.

[11] Harald Fritzsch: *Composite Weak Bosons*
`http://arxiv.org/abs/1010.1428`, October 2010.

[12] Mariannne Johansen: *Studies of Long-lived Supersymmetric Top Quarks and Online monitoring of the ATLAS First Level Calorimeter Trigger*,
PhD thesis, Stockholm University 2010.

[13] M. Fairbairn, A.C.Kraan, D.A. Milstead, T.Sjöstrand, P.Skands, T. Sloan: *Stable Massive Particles at Colliders*, 2006 `http://arxiv.org/hep-ph/0611040`

[14] S. Dimopoulos, D. Eichler, R. Esmailzadeh and G.D. Starkman: *Getting a charge out of dark matter*,
Phys.Rev. D 41, 1990.

[15] Ed. A.Breskin and R.Voss: *The CERN Large Hadron Collider: Accelerator and Experiments*, Vol. 1, CERN 2009

[16] Cern press release archive: *Incident in LHC sector 3-4*,
`http://press.web.cern.ch/press/PressReleases/Releases2008/PR09.08E.html`

[17] Cern press release archive: *The LHC is back*,
`http://press.web.cern.ch/press/PressReleases/Releases2009/PR16.09E.html`

[18] Alice Collaboration: *Elliptic Flow of Charged Particles in Pb Pb Collisions at 2.76 TeV*,
`http://xxx.lanl.gov/abs/1011.3914`

[19] Alice Collaboration: *Charged-Particle Multiplicity density at mid-rapidity in central Pb-Pb collisions at sqrt(sNN)02.76 TeV*,
`http://xxx.lanl.gov/abs/1011.3916`

[20] Aafke C. Kraan: *Interactions and Detections of R-hadrons*,
PhD thesis, Niels Bohr Institute, 2004.

[21] Konrad Kleinknecht: *Detectors for Particle Radiation*, Cambridge University Press, second ed. 1998.

[22] ATLAS Collaboration: *The ATLAS Experiment at the CERN Large Hadron Collider*, Journal of Instrumentation, 2008 `http://iopscience.iop.org/1748-0221/3/08/S08003`

[23] ATLAS Level-1 Trigger Group,
Level-1 Trigger Technical Design Report, 1998 ATLAS, CERN.

[24] ATLAS L1Calo Group, compiled by E. Eisenhandler: *ATLAS Level-1 Calorimeter Trigger Algorithms*,
ATL-DAQ-2004-011 ; CERN-ATL-DAQ-2004-011.

[25] *ATLAS liquid argon calorimeter: Technical design report, CERN-LHCC-96-41.*, December 1996.

[26] *ATLAS Tile Calorimeter: Technical design report, CERN-LHCC-96-42.*, December 1996.

[27] T. Sjöstrand, S. Mrenna, P. Skands, *Pythia 6.4, Physics and Manual*,
arXiv:hep-ph/0603175.

[28] R. Mackeprang and A. Rizzi: *Interactions of coloured stable particles in matter*, 2006
`http://inspirebeta.net/record/734378?ln=en`

[29] R. Mackeprang, D. Milstead: *An Updated Description of Heavy-Hadron Interactions in GEANT-4*, 2010
`http://inspirebeta.net/record/828442?ln=en`

[30] Rasmus Mackeprang: *Stable Heavy Hadrons in Atlas*, PhD thesis, Niels Bohr Institute, 2007.

[31] T. Cornelisen et al.: *Search for Stable Hadronising Squarks and Gluinos at the ATLAS Experiment at the LHC*, cern 2011 `http://inspirebeta.net/record/892044?ln=en`

[32] Aafke C. Krann: *Interactions of Heavy Stable Hadronizing Particles*, arXiv:hep-ex/0404001, april 2004.

[33] R. Mackeprang, D.Milstead, G. Farrar, J.P. Roberts: *Limit on the mass of a long-lived or stable gluino*, 2010 `http://inspirebeta.net/record/877357?ln=en`

[34] Y.R. de Boera, A.B. Kaidalova, D.A. Milstead, O.I. Piskounova:*Interactions of Heavy Hadrons using Regge Phenomenology and the Quark Gluon String Model* arXiv:0710.3930v2 [hep-ph], 22 Oct 2007

[35] Particle Data Group: *particle listings 2010* `http://pdg.lbl.gov/2010/listings/contents_listings.html`

[36] Florian Beaudette: *Top physics prospects at LHC* , presentation held at "XLth Rencontres de Moriond" 2005 `http://moriond.in2p3.fr/EW/2005/Transparencies/3_Tuesday/2_evening/7_F_Beaudette/Beaudette`

[37] S. P. Martin: *A Supersymmetry Primer*, arXiv:hep-ph/9709356v5, 2008.

[38] S. Hellman, M. Johansen, R. Mackeprang, P. Mermod, D. Milstead, C. Ohm, A. Solodkov: *Measuring time-of-flight and identifying exotic stable massive particles with the ATLAS Tile calorimeter*, 2009.

[39] ed. E. Klinkby, R. Mackeprang, D .Milstead, *Search for Stable Hadronising Squarks and Gluinos at the Atlas Experiment at the LHC*, 2011 ATL-COM-PHYS-2010-1065 `http://cdsweb.cern.ch/record/1317326`

[40] Morten Dam Joergensen, *Search for long-lived massive particles*, 2011